Correlation between Raman spectroscopy and electron microscopy on individual carbon nanotubes and peapods

Vom Fachbereich Physik
der Universität Duisburg-Essen
zur Erlangung des akademischen Grades eines
Doktors der Naturwissenschaften
genehmigte Dissertation von

Christian Spudat

geb. in Berlin

Tag der Einreichung: 1. Februar 2010
Tag der mündlichen Prüfung: 2. Juni 2010
Gutachter: Prof. Dr. C. M. Schneider (Universität Duisburg-Essen)
Zweitgutachter: Jun.-Prof. Dr. C. Stampfer (RWTH Aachen)

Abstract

In this thesis, we investigate the possibility of filling carbon nanotubes (CNTs) grown by chemical vapor deposition (CVD) with guest molecules directly on substrates. This requires the characterization of CNTs after synthesis. It is shown by high-resolution TEM and Raman spectroscopy that the diameter distribution and number of layers of as-grown CNTs depends on the growth temperature T_{CVD}.
HRTEM measurements are seen to induce defects, even when performed at electron energies as low as 80 keV. Raman spectroscopy, on the other hand, is non-destructive for individual CNTs at small laser intensities ($P < 0.5$ mW). This fact motivated us to attempt a correlation of HRTEM and Raman spectroscopy, which allowed us to prove the radial phonon-coupling for an individual multi-walled CNT and a bundle of single-walled CNTs for the first time experimentally and to confirm our results by a simple numeric model. Furthermore, it could be shown that the width of the resonance profiles of radial Raman modes allows one to determine whether the investigated CNT is an individual single-walled CNT, located within a bundle or a layer of a multi-walled CNT. This makes a determination of the inter-molecular structure of CNTs possible without damaging the CNTs by TEM imaging. Moreover, resonant Raman spectroscopy provides important information about the electronic structure of the investigated CNTs, which is essential for interpreting future quantum transport measurements and permits the determination of the atomic structure of individual CNTs.
A second part of this thesis deals with the synthesis of peapods, CNTs filled with fullerene molecules such as C_{60}. We present a detailed characterization of individual CNTs after each step of the peapod synthesis, focusing especially on the opening of the as-grown CNTs. A UHV-chamber was built up to avoid reactions between the opened CNTs and the atmosphere, allowing for the *in situ* removal of excess fullerene molecules from the CNTs. Using this novel method, we obtain clean peapods in different yields and with different numbers of layers directly on the substrate, which opens the way for future quantum transport measurements of these systems.

Zusammenfassung

In der vorliegenden Arbeit wurde untersucht ob Kohlenstoffnanoröhrchen (CNTs), die mit Hilfe der chemische Gasphasenabscheidung (CVD) auf Substraten gewachsen wurden, direkt mit Gastmolekülen gefüllt werden können. Dies setzt eine Charakterisierung der gewachsenen CNTs nach der CVD-Synthese voraus. Dabei konnte mit Hilfe von hochauflösender Transmissionselektronenmikroskopie (HRTEM) und Raman Spektroskopie gezeigt werden, dass die Durchmesserverteilung und die Anzahl der Wände von der Wachstumstemperatur T_{CVD} abhängen.
Während HRTEM-Messungen werden jedoch Defekte in den CNTs induziert, was bereits bei Elektronenenergien von 80 keV beobachtet werden konnte. Raman Spektroskopie hingegen ist für kleine Laserleistungen ($P < 0.5\,\mathrm{mW}$) zerstörungsfrei für einzelne CNTs. Diese Beobachtung motivierte zu einer Korrelation von HRTEM und Ramanspektroskopie, mit deren Hilfe erstmals die radiale Phononen-Kopplung in einem einzelnen mehrwandigem CNT und einem Bündel von einwandigen CNTs experimentell nachgewiesen und durch ein einfachen numerischen Modells bestätigt werden konnte. Weiterhin konnte gezeigt werden das Anhand der Breite des Resonanzprofils der radialen Raman-Moden festgestellt werden kann, ob das untersuchte CNT ein einzelnes einwandiges CNT ist, sich innerhalb eines Bündels von CNTs befindet oder eine Wand eines mehrwandigen CNT ist. Dies ermöglicht mit Hilfe von Raman-Messungen auf die intermolekulare Struktur von CNTs zu schließen, ohne diese zu beschädigen. Darüber hinaus liefert die resonante Raman Spektroskopie wichtige Informationen über die elektronische Struktur der untersuchten CNTs, was essentiell für die Interpretation späterer Quantentransport Messungen ist und die Bestimmung der atomaren Struktur von einzelnen CNTs erlaubt.
Der zweite Teil dieser Arbeit untersucht das Füllen der gewachsenen CNTs mit Fullerenen, wie beispielsweise C_{60}, wobei die gefüllten CNTs als „Peapods“ bezeichnet werden. Wir präsentieren eine detaillierte Charakterisierung einzelner CNTs nach jedem Schritt der Peapod-Synthese, wobei insbesondere auf das Öffnen der gewachsenen CNTs eingegangen wird. Um Reaktionen der geöffneten CNTs mit der Atmosphäre zu vermeiden, wurde eine UHV-Kammer aufgebaut, welche es ermöglichte die CNTs *in situ* von überschüssigen C_{60} Molekülen zu reinigen. Dieses neue Verfahren erlaubt die Synthese von sehr sauberen Peapods in verschiedenen Ausbeuten und mit einer unterschiedlichen Anzahl von Außenwänden direkt auf dem Substrat, was den Weg für zukünftige Quantentransport Messungen an diesen Systemen öffnet.

Danksagung

Im Folgenden möchte ich denjenigen Personen danken die zum Gelingen dieser Arbeit beigetragen haben:

Prof. Dr. Claus M. Schneider danke ich für die Möglichkeit diese Arbeit durchführen zu dürfen und seine Tipps und Ratschläge während der letzten drei Jahre.

Jun.-Prof. Dr. Christoph Stampfer danke ich für die Übernahme des Korreferats.

Dr. Carola Meyer möchte ich für die Betreuung dieser Arbeit danken. Sie stand mir während dieser Arbeit immer mit Rat und Tat zur Seite, wobei die Diskussionen mit ihr entscheidend zum Gelingen dieser Arbeit beigetragen haben. Auch für die vielen nützlichen Tipps und Anregungen während der Schreibphase möchte ich mich bei ihr bedanken.

Dr. Lothar Houben danke ich für die Betreuung während der HRTEM-Messungen am Ernst-Ruska Zentrum. Ohne seine Hilfe wären viele TEM-Bilder in dieser Arbeit nicht möglich gewesen.

Prof. Christian Thomsen möchte ich für die sehr fruchtbaren Kirchberg-Konferenzen und die Möglichkeit, RRS-Messungen an der TU Berlin durchführen zu können, danken. **Prof. Dr. Janina Maultzsch** danke ich für die Gespräche über Raman Spektroskopie an CNTs und für die Hilfestellungen bei der Interpretation der gemessenen Daten. Insbesondere danke ich **Dipl. Phys. Matthias Müller** für die Erstellung der Resonanzprofile und die gemeinsamen Messzeiten in Berlin.

Prof. Paul Kögerler danke ich für die Nutzung des FT-Raman Spektrometers und die Synthese der Polyoxometallat-Cluster.

Prof. Thomas Pichler und **Dr. Christian Kramberger** danke ich für die

Einführung in das Füllen von CNTs im Rahmen meines Besuches am IFW Dresden.

Meinen Kollegen in der Nachwuchsforschergruppe Meyer, **Dipl. Phys. Karin Goß**, **Dipl. Phys. Caitlin Morgan** und **Dipl. Phys. Robert Frielinghaus**, danke ich für die gute Zusammenarbeit und gegenseitige Hilfestellungen. Insbesondere für das Korrekturlesen dieser Arbeit möchte ich mich bei ihnen bedanken.

Dipl. Phys. Julius Mennig danke ich für die Einführung in die Benutzung des UHV-SEMs und das Schreiben der FIB-Marker in die Si_3N_4 Substrate.

Fabian Knorr danke ich für sein Mitwirken bei der Untersuchungen der Phononenkopplung in Bündeln von CNTs mit Hilfe der FT-Raman Spektroskopie im Rahmen seiner Bachelor-Arbeit.

Akashdeep Kamra danke ich für die AFM-Charakterisierung der von Polyoxometallat-Clustern gewachsenen CNTs im Rahmen seiner Studienarbeit.

Steffen Wegscheider danke ich für seine Hilfe bei der Durchführung der konfokalen Raman-Messungen an einzelnen CNTs, die er im Rahmen seiner Diplomarbeit untersuchte.

Prof. Andreas Rüdiger und **Dr. Serge Röhrig** danke ich für die Einführung in die Benutzung des konfokalen Raman Spektrometers.

Dipl. Ing. Holger John und **Dr. Christian Pithan** danke ich für die Betreuung des Raman-Labors.

Unseren Technikern **Ing. Konrad Bickmann** und **Bernd Küppers** danke ich für ihre Hilfestellung, wenn immer es etwas zu konstruieren gab. Insbesondere der Aufbau der UHV-Kammer wäre ohne ihre Hilfe nicht möglich gewesen.

Heinz Pfeiffer und **Jürgen Lauer** danke ich für die Unterstützung bei elektronischen und numerischen Problemen.

Meinen beiden Zimmerkollegen **Dr. Carsten Wiemann** und **Dr. Alexander Kaiser** danke ich für das nette Arbeitsklima und die gemeinsame Zeit im Raum 26a.

Dr. Frank Matthes danke ich für das Einrichten einer Fahrgemeinschaft von Aachen nach Jülich und das geduldige Warten wenn der Wecker mal zu leise war.

Desweiteren möchte ich allen anderen Mitarbeitern des IFF-9 für die gemeinsa-

me Zeit und ihre Unterstützung danken.

Mein besonderer Dank geht an meine Freundin **Sarah**, die mir mit ihrer Liebe und Kraft auch über die schwierigen Zeiten dieser Arbeit half.

Erklärung

Hiermit erkläre ich, dass ich die vorliegende Arbeit selbständig und ohne fremde Hilfe verfasst habe. Ferner habe ich außer den angegebenen Quellen keine anderen Quellen und Hilfsmittel benutzt. Die dem Sinn oder Wortlaut nach entnommenden Textpassagen oder Abbildungen habe ich in jedem Einzelfall kenntlich gemacht. Dieser Dissertation geht weder ein erfolgloser Promotionsversuch voraus, noch wurde sie in einem weiteren Promotionsverfahren eingereicht. Abgesehen von den angegebenen Publikationen sind die Ergebnisse dieser Dissertation unveröffentlicht. Diese Dissertation, die den Doktorgrad „Dr. rer. nat." anstrebt wurde von Prof. Dr. C. M. Schneider betreut.

(Christian Spudat)

Contents

Chapter 1

Introduction

The discovery of carbon nanotubes (CNTs) is credited to Iijima *et al.* [1] in 1991, who first noted their graphitic structure, although CNTs were previously synthesized by Radushkevich *et al.* [2] in 1952 and Oberlin *et al.* [3] in 1976. In addition to amorphous carbon, diamond, graphite and C_{60} CNTs establish a unique modification of carbon. They consist of only carbon atoms and can be described as layers of graphite wrapped into a seamless cylinder forming an inner hollow. When a CNT consists of only a single layer of graphite, it is called a single-walled carbon nanotube (SWCNT), while double-walled carbon nanotubes (DWCNTs) and multi-walled carbon nanotubes (MWCNTs) have two or more layers, respectively. These layers form cylinders and are concentrically encapsulated into each other being separated by approximately the van der Waals (vdW) distance of graphite. Recently, DWCNTs and MWCNTs were suggested for building nano-electro-mechanical systems (NEMS), such as low-wear bearings [4] or gigahertz oscillators [5].
In general, SWCNTs vary from metallic to semiconducting depending on their chirality. Due to their extremely large aspect ratio, featuring diameters in the order of nanometers, but lengths up to several centimeters [6], SWCNTs provide a structural confinement serving as a model for a one-dimensional system, which gives rise to outstanding electronic properties. Semiconducting and metallic SWCNTs show ballistic transport [7] allowing extremely large current densities in the order of $10^9\,\mathrm{A/cm^2}$ [8], which even leads to superconductivity below 20 K for SWCNTs with a diameter of only 4.2 Å [9]. For metallic SWCNTs, the Kondo effect has been observed [10], as well as evidence for Luttinger liquid behavior [11, 12].
When individual SWCNTs are contacted by metal leads, quantum dot behavior has been observed at low temperatures, where energy quantization is due to the confinement given by these contacts acting as tunneling barriers [13]. This provides an experimental realization of a one-dimensional particle in a box system, where the confined quantum dot can be selectively filled electron by electron by tuning the potential with a gate electrode in the proximity of an individual CNT [14].
The magnetic and electronic properties of CNTs can be altered by functionalization

[15]. This can be done by sticking side groups on the outside or the inside of the CNTs or by filling the inner hollow of CNTs with guest molecules. When C_{60} is used as a guest molecule, C_{60} molecules align inside the CNTs similar to peas in a peapod [16]. Therefore, these structures are called peapods and have recently generated a lot of interest as systems for future electronic applications. The C_{60} fullerenes inside the tubes modulate the local density of states due to hybridization of the molecular orbitals with the conduction band [17], and endohedral fullerenes inside a semiconducting tube can change the bandgap [18]. These effects allow one to build ambipolar CNT field effect transistors [19] and to tune the gate-dependent conductance of single electron transistors [20]. But filling CNTs with fullerenes can also change their mechanical properties, e.g., softening the vibrational modes [21, 22], which is interesting for the fabrication of nano-electro-mechanical devices.
The included C_{60} molecule itself, which also provides an inner hollow, can be functionalized by side groups or guest molecules from the inside or the outside as well. When the C_{60} molecules are filled with paramagnetic atoms, e.g. N or P, resulting in endohedral fullerenes N@C_{60} and P@C_{60} respectively, this structure provides a one-dimensional spin chain. Natural carbon consists of mainly two isotopes: ^{12}C and ^{13}C, where only ^{13}C has a nuclear spin. Since carbon consists of 98.8 % ^{12}C, nuclear fields leading to spin relaxation are negligible, which makes CNTs an ideal matrix for the alignment of individual spin centers. Due to their close one-dimensional arrangement in CNTs, the endohedral atoms couple with one another. This allows the investigation of spin chains coupled to a ballistic conductor, which makes peapods filled with endohedral fullerens a promising material for spin electronic (spintronic) devices [23].
When a peapod filled with endohedral fullerenes is contacted, a coupling between the electrons in the quantum dot and electrons of the atoms within the endohedral fullerenes is expected at low temperatures. This may be useful as a read-out for their spin state, which can be altered by an external magnetic field $\vec{B}_0$. Such a device is illustrated in figure 1.1, which is based on the concepts of Ardavan *et al.* [24]. It combines the excellent electronic properties of CNTs with a multiplicity of different electron spin systems provided by endohedral fullerenes to study spin dependent transport.
For electronic applications, CNTs are often grown by chemical vapor deposition (CVD), because this method leads to long and well-separated CNTs. This is in contrast to CNTs dispersed from solution, which are comparably short and tend to align themselves side by side due to their inter-tube vdW interactions. Thus, they form bundles, preventing one from contacting individual CNTs. Furthermore, catalyst particles, which induce the growth of CNTs during CVD, can be placed at selected sites on the substrate by using electron beam lithography, allowing for synthesis of CNTs at predefined sites of the sample [25].
To choose those CNTs for device fabrication which show the desired yield of func-

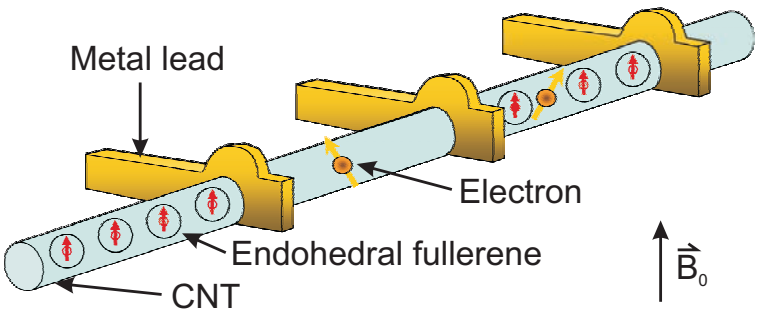

Figure 1.1: Illustration for the use of a contacted CNT filled with endohedral fullerenes as a device for quantum information applications. A coupling between the quantum dot and the atoms within the endohedral fullerenes is expected.

tionalization, doping, etc., a characterization on the single CNT level is needed. Transmission electron microscopy (TEM) is an important tool for characterizing the atomic structure of CNTs. Especially due to the increase in resolution by using aberration corrected high-resolution transmission electron microscopy (HRTEM), it is possible to investigate a CNTs diameter, purity, number of layers and inter-layer distance directly. Furthermore, HRTEM provides the investigation of the inner hollow of CNTs with different numbers of layers, and is therefore widely used to verify the filling of CNTs. This allows one to determine the diameter of the innermost tubes of MWCNTs, which is most important for providing enough space for the filling of CNTs with guest molecules like C_{60} [26]. Because of the introduction of defects during electron irradiation, which can even lead to the destruction of the investigated CNT, HRTEM can only be used as the last step and does not allow a pre-characterization of the CNTs or peapods.
In contrast, Raman spectroscopy is a non-destructive tool to determine the effects of functionalization, for example creation of defects or changes in the electronic structure [27]. Furthermore, resonant Raman spectroscopy (RRS) provides the structural characterization of individual SWCNTs by determining their chirality [28]. But since Raman spectroscopy provides only indirect information on the atomic structure of CNTs, a correlation of microscopy and spectroscopy measurements on the same CNTs is needed to interpret the observed Raman spectra.
Therefore the first aim of this thesis is to further develop Raman spectroscopy as a characterization method for individual CNTs and bulk samples. This is achieved by making a detailed correlation of HRTEM and Raman spectroscopy for both individual CNTs and bulk samples to study the influences of different atomic and molecular structures of CNTs on the obtained Raman spectra. It allows us to study the inter-layer phonon coupling in a bundle of SWCNTs and an individual MWCNT for the first time experimentally, providing a new way to pre-characterize individual

CNTs.
In order to keep the advantages of the CVD growth, the peapod synthesis has to be carried out directly on the substrates. Peapods filled with empty C_{60} molecules could be synthesized from bulk material of CNTs dispersed from solution [29]. To obtain individual peapods from CVD-grown CNTs, the procedures for the synthesis of peapods using bulk material have to be adapted for individual CNTs attached to the substrate. This has only been achieved by two research groups so far [30, 31].
Thus, the second aim of this thesis is to confirm the synthesis of peapods from CVD-grown CNTs directly on different substrates, which are suitable for later transport measurements. As a start, empty C_{60} molecules are used to fill the CNTs. In order to optimize the peapod synthesis, we present a detailed characterization of each synthesis step by a correlation of HRTEM and Raman spectroscopy, which allows us to study the atomic and the electronic structure of CNTs and to confirm their opening, filling, and cleaning.

This thesis is organized as follows:
As an introduction, we will discuss the atomic structure of SWCNTs, which is the origin of their different electronic properties in **chapter 2**. These can be determined by the so-called zone-folding approximation starting from the band structure of graphene, a single layer of graphite. In addition, the electronic structure of CNTs depends on tube-tube interactions induced for bundled SWCNTs or MWCNTs. Furthermore, peapods are expected to alter their electronic structure due to interactions between the CNT and the encapsulated C_{60} molecules, which can tune the properties of the CNTs [32]. This leads to shifts in the band structure, which will be discussed separately. Since CNTs show a strong electron-phonon coupling [33], the understanding of the electronic structure of CNTs and peapods is fundamental for the interpretation of the Raman spectra.
In **chapter 3**, the experimental methods used are introduced. There we will focus on HRTEM and Raman spectroscopy, being the prominent methods used in this thesis. Although HRTEM is operated at 80 keV, which is the smallest electron energy possible for the instrument used, it leads to the introduction of defects due to electron irradiation annealing [34]. On the other hand, non-destructive Raman spectroscopy, which only probes the phononic and electronic properties of the investigated CNTs, does not provide one with a clear determination of the atomic structure. Therefore, these two characterization methods are correlated in this thesis to obtain a better understanding of the influences of the atomic structure of CNTs and peapods on their electronic properties and characteristic phonons, which are introduced and discussed. This chapter closes with a comparison of the characterization methods used, which feature different possibilities and restrictions.
In **chapter 4**, an overview of the known synthesis methods for CNTs is given, followed by a discussion and comparison of said methods. We will focus on the growth of CNTs

by CVD, which is used to grow CNTs directly on substrates in this thesis. Because the CNTs obtained are investigated with different characterization methods, the use of different kinds of substrates is necessary, which will be introduced discussing their applications and limitations. Since CNTs are grown by a catalytic process, different kinds of catalysts and their resulting CNTs are investigated and compared, focusing on the usage of Fe:Mo alloy catalysts. Another important synthesis parameter is the growth temperature T_{CVD}, which is varied for different samples to investigate its influence on the structure of the obtained CNTs. This characterization of the starting material for the peapod synthesis is essential in order to distinguish between the effects of further processing steps.

In **chapter 5**, the effect of tube-tube interactions on the optical transition energies is studied. They are investigated by RRS for a small bundle of SWCNTs and an individual MWCNT, using several laser excitation energies in order to obtain resonance profiles for resonant Raman modes. These results are compared to HRTEM and AFM measurements to see how far individual CNTs can be characterized by Raman spectroscopy alone. This would help to pre-characterize individual CNTs and to select adequate CNTs for further processing.

In **chapter 6**, Raman spectroscopy is used to investigate an individual MWCNT and a small bundle to study the influence of the tube-tube interactions on their radial vibration modes. Since MWCNTs and individual SWCNTs in bundles are coupled by weak vdW interactions, the coupling of phonons is theoretically predicted for these CNTs, but not yet observed experimentally. A correlation of RRS and HRTEM measurements allows us to introduce a numeric model to simulate the effect of phonon coupling in MWCNTs and bundles of SWCNTs and to compare our result to the existing models. This may introduce a new method to distinguish the number of layers and their diameters by Raman spectroscopy alone.

In **chapter 7**, the peapod synthesis from individual CNTs and bulk samples directly on substrates is presented. Because as-grown CNTs have to be opened before they can be filled, two different oxidation methods are investigated. These are acid treatment with and without subsequent annealing and heating in air. The removal of exterior C_{60} molecules from the CNTs after filling is essential, not only for later transport measurements, but also to confirm the filling of CNTs with experimental methods. Therefore, a UHV-chamber has been built up, allowing for the production of clean peapods with different number of layers by using vapor filling directly on substrates. The obtained samples are characterized by HRTEM and Raman spectroscopy to specify their filling yield and their purity. These results are compared to conventionally produced peapods from other groups.

This thesis closes with **chapter 8**, which concludes the main results and gives an outlook on future experiments.

Chapter 2

Basic properties of carbon nanotubes

The outstanding electronic properties of CNTs as discussed in chapter 1 are a direct consequence of their unique atomic structure. These vary for different SWCNTs; where some SWCNTs show a metallic behavior, others are semiconducting. The axial atomic assembly of different single-walled carbon nanotubes (SWCNTs) and their electronic band structure can be derived from cut and rolled up graphene, a single layer of graphite, allowing the classification of different SWCNTs in chapter 2.1. These different atomic assemblies of SWCNTs are due to their spiral conformation called chirality, which is defined by their chiral vector. This explains their different electronic behaviors, which are ordered in different families in chapter 2.2. They are the basis for the interpretation of optical transitions investigated by Raman spectroscopy. Different environments also influence the band structure of SWCNTs leading to shifted transition energies and therefore provide additional information about their inter-molecular arrangements. These effects will be discussed in chapter 2.5, chapter 2.6 and chapter 2.7.

2.1 Atomic structure

SWCNTs can be described by a single layer of graphite rolled-up into a seamless cylinder. Their atomic assembly depends on how the layer is cut out from a graphene sheet as illustrated in figure 2.1a. The resulting SWCNT is defined by the chiral vector $\vec{C}_h$ around its circumference (figure 2.1b). The chiral vector is expressed with the graphene lattice vectors $\vec{a}_1$ and $\vec{a}_2$ by

$$\vec{C}_h = n_1\vec{a}_1 + n_2\vec{a}_2 \tag{2.1}$$

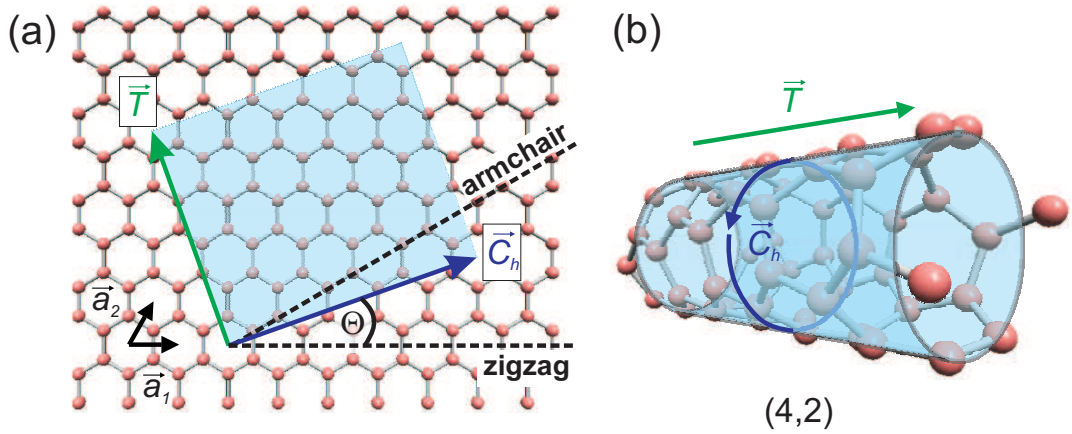

Figure 2.1: (a) Hexagonal lattice of graphene with its basis vectors $\vec{a}_1$ and $\vec{a}_2$. A rectangular sheet (blue area) is cut out of the graphene lattice, which is defined by the translation vector $\vec{T}$ (green arrow) and the chiral vector $\vec{C}_h$ (blue arrow). The atomic assignments of the resulting SWCNT vary for different chirality angles between $\Theta = 0°$ (zigzag) and $\Theta = 30°$ (armchair) as marked by the black dashed lines. (b) When the shaded area in (a) is rolled-up along $\vec{C}_h$ the unit cell of a (4,2) SWCNT is obtained.

and (n_1,n_2) is called the chiral index.
The length of the unit cell is given by the translation vector $\vec{T}$, which represents the unit cell along the nanotube axis and is given by

$$T = |\vec{T}| = a_0 \frac{\sqrt{3(n_1^2 + n_1 n_2 + n_2^2)}}{\gcd(n_1, n_2)\mathcal{R}}, \tag{2.2}$$

with the graphene lattice constant $a_0 = \sqrt{3}a_{cc} = 2.46\,\text{Å}$. In this equation $\gcd(n_1, n_2)$ is the greatest common denominator of n_1 and n_2 and

$$\mathcal{R} = \begin{cases} 3 & \text{if } (n_1 - n_2)/[3\gcd(n_1, n_2)] \in \mathbb{N} \\ 1 & \text{otherwise.} \end{cases} \tag{2.3}$$

These two vectors $\vec{C}_h$ and $\vec{T}$ define the unit cell of a SWCNT, which is shown in figure 2.1b for a SWCNT with a chiral index of (4,2). Thus, except for the length of the unit cell, which is given by $|\vec{T}|$, all other structural properties of a SWCNT can be determined by its chiral index (n_1,n_2).
The diameter of a SWCNT is given by

$$d_\text{T} = \frac{|\vec{C}_h|}{\pi} = \frac{a_0}{\pi}\sqrt{n_1^2 + n_1 n_2 + n_2^2} = \frac{\sqrt{3}a_{cc}}{\pi}\sqrt{n_1^2 + n_1 n_2 + n_2^2}, \tag{2.4}$$

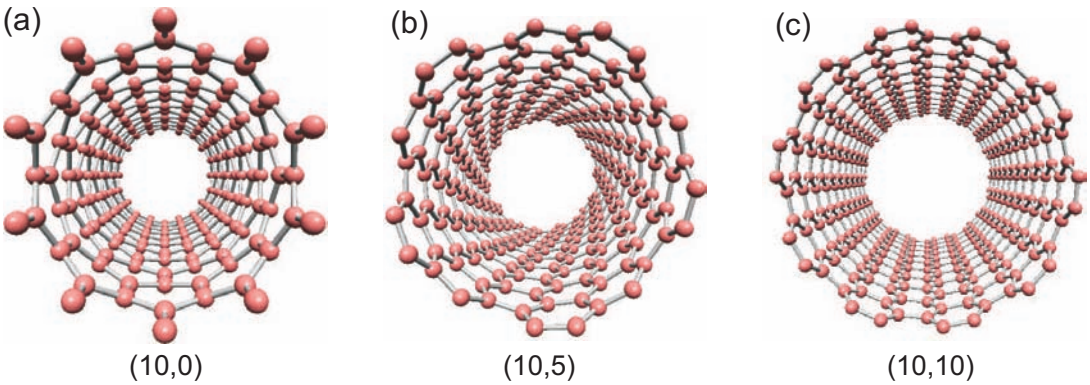

Figure 2.2: Atomic structure of (a) a (10,0) zigzag SWCNT, (b) a (10,5) chiral SWCNTs and (c) a (10,10) armchair SWCNT. The diameter is increasing for higher chiral angles from (a) 0.78 nm via (b) 1.03 nm to (c) 1.35 nm. Carbon atoms and bonds are colored red and grey respectively.

where $a_{cc} = 1.421$ Å is the nearest neighbor distance of carbon atoms in graphite.
The angle between the chiral vector $\vec{C}_h$ and the lattice vector $\vec{a}_1$ is called the chiral angle Θ and is given by

$$\Theta = \arccos\left[\frac{n_1 + n_2/2}{\sqrt{n_1^2 + n_1 n_2 + n_2^2}}\right], \tag{2.5}$$

which varies between $0° \leq \Theta \leq 30°$. All other ranges are equal to this interval due to the six-fold hexagonal symmetry of graphene. Thus, $(n_1, 0)$ SWCNTs have the smallest chiral angle of $\Theta = 0°$ and are called zigzag SWCNTs due to their zigzag alignment of carbon atoms along their circumference, while (n_1, n_1) SWCNTs with the highest chiral angle of $\Theta = 30°$ are called armchair SWCNTs. These two extreme cases are drawn in figure 2.1a by dashed lines, which show their high symmetry within the graphene lattice. They are called achiral, while SWCNTs with a intermediate chiral angle of $30° > \Theta > 0°$ featuring a lower symmetry are called chiral. The resulting different atomic arrangements are illustrated in figure 2.2.
As we will see in chapter 2.2, armchair SWCNTs are metallic, while zigzag and chiral SWCNTs can be semiconducting or semimetallic featuring a finite bandgap of 0.3-1.0 eV and 50 meV respectively [35]. In general, SWCNTs can be classified in three families, that are characterized by the family index

$$\nu = (n_1 - n_2) \bmod 3 = \begin{cases} -1 & \text{semiconducting SWCNTs type I} \\ 0 & \text{(semi)metallic SWCNTs} \\ +1 & \text{semiconducting SWCNTs type II,} \end{cases} \tag{2.6}$$

while only armchair tubes with $\nu = 0$ are metallic, whereas all other SWCNTs with $\nu = 0$ are semimetallic. Because of the small bandgap of semimetallic SWCNTs, electrons are excited at room temperature, which gives these small bandgap semiconductors a metallic behavior.

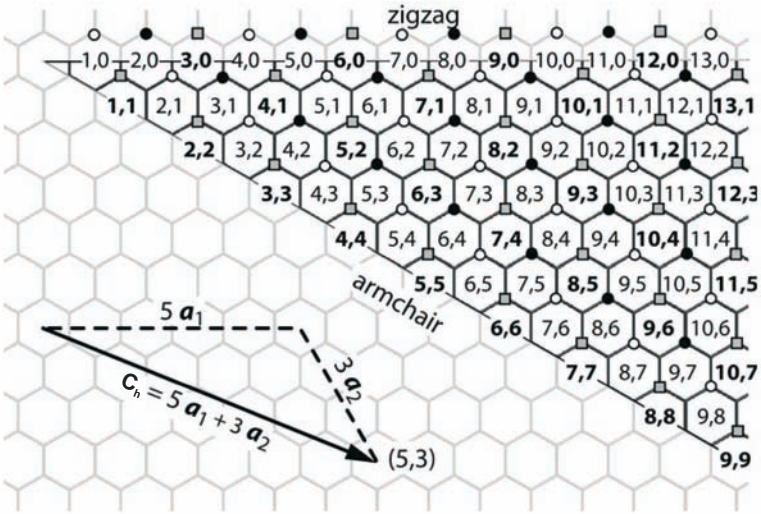

Figure 2.3: Chiral indices of SWCNTs mapped onto a graphene lattice taken from [36]. Different families are marked by small symbols in the upper corner of each hexagon, where filled circles stand for semiconducting type I ($\nu = -1$), open circles for semiconducting type II ($\nu = +1$) and filled squares for metallic SWCNTs ($\nu = 0$).

Figure 2.3 shows the chiral indices for SWCNTs with a diameter $d_{\mathrm{T}} \leq 1.2\,\mathrm{nm}$ mapped onto a graphene sheet belonging to different families defined by the family index ν, where about 1/3 of the SWCNTs with different chiral indices are metallic, while 2/3 are semiconducting. SWCNTs of the same family are connected by lines parallel to the armchair direction or its equivalent translations. The lower right corner shows the chiral vector $\vec{C}_h$ of a $(5, 3)$ SWCNT, for example, obtained by the addition of the lattice vectors $\vec{a}_1$ and $\vec{a}_2$.

2.2 Electronic structure

The electronic properties of SWCNTs can be derived from the band structure of graphene. This method is called the zone-folding approximation [37]. The electronic band structure of graphene can be calculated by an empirical tight-binding model, which includes only the π-orbitals perpendicular to the graphene surface and their

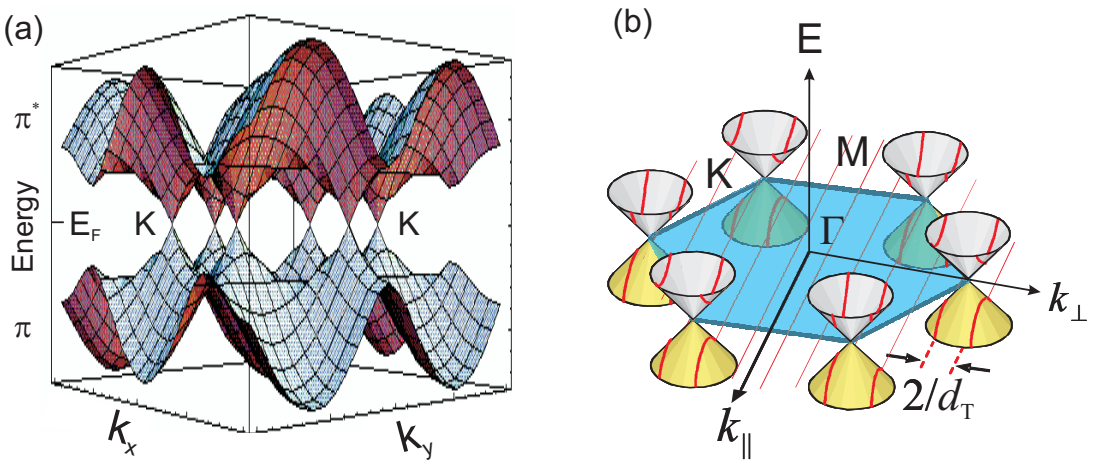

Figure 2.4: (a) Tight-binding calculation of the band structure of graphene around its hexagonal Brillouin zone (taken from [38]). The valence (conduction) band is labeled with π (π^*). (b) Scheme to depict the zone-folding approximation: Boundary conditions cause discrete reciprocal vectors $\vec{k}_\perp$ perpendicular to the tube axis (red lines), which cut the cones of graphene, while $\vec{k}_\parallel$ parallel to the tube axis is almost continuous for long SWCNTs. The Fermi surface of the Brillouin zone of graphene is shown by the blue area with its symmetry points K, M and Γ.

interactions, which gives rise to the electronic bands close to the Fermi level [39]. If only nearest neighbors are considered the energy dispersion in graphene is given by

$$E_\pm(\vec{k}) = \gamma_0 \sqrt{3 + 2\cos\vec{k}\cdot\vec{a}_1 + 2\cos\vec{k}\cdot\vec{a}_2 + 2\cos\vec{k}\cdot(\vec{a}_1 - \vec{a}_2)}, \tag{2.7}$$

where γ_0 describes the interaction between two neighboring π-electrons and $\vec{k}$ is the reciprocal wave vector in the Brillouin zone (BZ) of graphene [41]. E_+ represents the energy of the π^*-states in the conduction band, while E_- is the energy of the π-states of the valence band. Figure 2.4a shows this electronic dispersion of graphene within its hexagonal BZ depending on the cartesian reciprocal basis vectors $\vec{k}_x$ and $\vec{k}_y$.
Graphene is a semimetal, as the π- and π^*-bands touch only at the six so-called K-points in the corners of the hexagonal BZ. Around these points both bands are approximately linear with $\vec{k} = k_x\vec{k}_x + k_y\vec{k}_y$ and can be described as cones centered at the K-points of the BZ as shown in figure 2.4b.
This two-dimensional band structure of graphene is further reduced for SWCNTs and can be described with the following zone-folding approximation. Their circumference

allows only discrete reciprocal wave vectors $\vec{k}_\perp = k_\perp \vec{e}_{k_\perp}$ perpendicular to the tube axis given by

$$\vec{C}_h \cdot \vec{k}_\perp = 2\pi m; \quad \vec{T} \cdot \vec{k}_\perp = 0; \quad \vec{C}_h \cdot \vec{k}_\parallel = 0; \quad \vec{T} \cdot \vec{k}_\parallel = 2\pi \tag{2.8}$$

with the wave vector parallel to the tube axis $\vec{k}_\parallel = k_\parallel \vec{e}_{k_\parallel}$ and $m \in \mathbb{N}$, which fulfill the boundary conditions. This yields a $\vec{k}$-space consisting merely of lines parallel to the tube axis, where the length of these lines is given by $2\pi/T$ and is continuous for long SWCNTs. Each line cuts the cones around the K-points with a distance between the lines of $\Delta k = 2/d_\mathrm{T}$. Thus, the actual band structure of a SWCNT is given by the electronic dispersion of graphene along these lines of allowed states, where each line results in a different band designated by the quantum number m in equation 2.8. When a K-point of the BZ lies on such a line, the SWCNT becomes (semi)metallic otherwise it will be semiconducting. The K-point of graphene is located at $1/3(\vec{k}_1 - \vec{k}_2)$, where the reciprocal basis vectors $\vec{k}_1$ and $\vec{k}_2$ are related to the basis vectors in real space $\vec{a}_1$ and $\vec{a}_2$ by $\vec{a}_i \cdot \vec{k}_i = 2\pi\delta_{ij}$. Thus, a SWCNT is (semi)metallic if

$$\vec{k} \cdot \vec{C}_h = 2\pi m = \frac{1}{3}(\vec{k}_1 - \vec{k}_2)(n_1\vec{a}_1 + n_2\vec{a}_2) = \frac{2\pi}{3}(n_1 - n_2), \tag{2.9}$$

with the quantum number m. This is fulfilled for

$$3m = n_1 - n_2, \tag{2.10}$$

and explains the relation of equation 2.6.

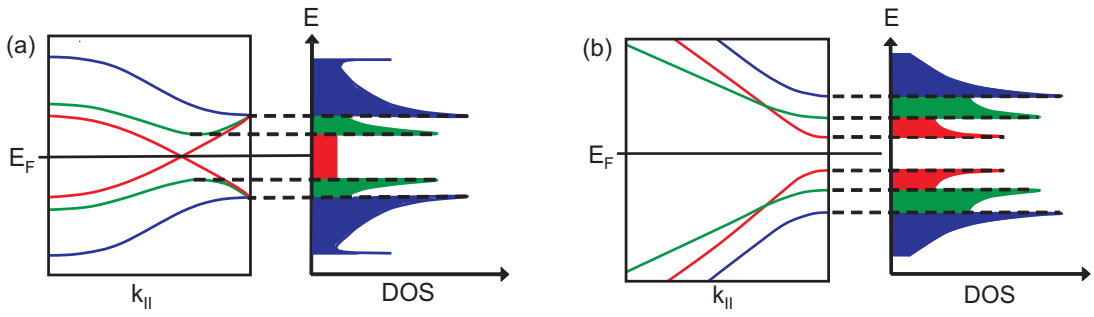

Figure 2.5: Schematic band structure obtained by the zone-folding approximation for (a) a metallic SWCNT and (b) a semiconducting SWCNT. For the metallic SWCNT the valence and conduction band cross providing a finite DOS at $\mathrm{E_F}$, while the conducting SWCNT shows a bandgap around the Fermi level. Sharp van Hove singularities can be observed for both SWCNTs in their DOS.

The band structure of SWCNTs obtained by the zone-folding approximation is illustrated schematically in figure 2.5 for (a) a metallic SWCNT and (b) a semiconducting SWCNT. Their one-dimensional density of states (DOS) is shown on the right side for each SWCNT, which features sharp van Hove singularities (vHSs) due to their one-dimensional confinement. While metallic SWCNTs show a finite DOS at the Fermi-level because of the crossing of their π- and π^*-bands, semiconducting SWCNTs have a bandgap between the first vHS of the valence and conduction band. Since the distance between the lines of allowed states that cut the BZ of graphene is $\Delta k = 2/d_\mathrm{T}$ and the dispersion decreases linearly with k around the K-points, the energy between the corresponding vHSs is proportional to $1/d_\mathrm{T}$.

2.3 Trigonal warping effect

In the zone-folding approximation the energy bands around the K-points are described to disperse approximately linearly with respect to k, leading to symmetrical cones. The trigonal warping effect describes the deviations from this linear energy dispersion around the K-points. Figure 2.6 shows contour energy plots around the K-point of graphene, calculated by equation 2.7 with $\gamma_0 = 2.9\,\mathrm{eV}$ [40]. Trigonal distortions of the

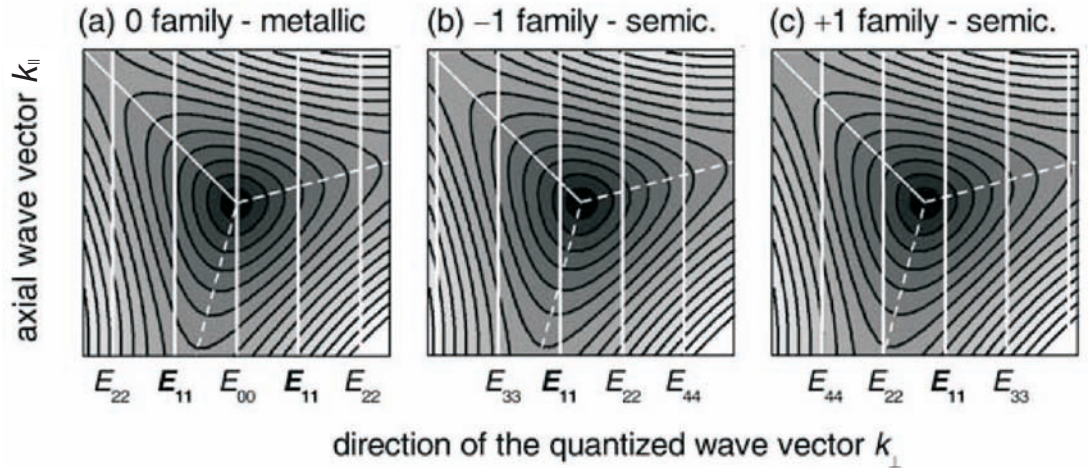

Figure 2.6: Equi-energy contour plots of the band structure of graphene close to the K-points showing the trigonal distortion in the direction of the M-points. Allowed wave vectors for (a) a metallic, (b) a semiconducting type I and (c) a semiconducting type II SWCNT are plotted by white vertical lines, which are labeled with their corresponding transition. A chiral angle of $\Theta = 15°$ and an equal tube diameter $\mathrm{d_T}$ is assumed (taken from [36]).

equi-energy contours can be seen to increase with the distance to the K-point due to the straight equi-energy lines between adjacent M-points in the BZ of graphene. The asymmetry of the energy contours around the K-point leads to a chirality dependence of the resulting energy bands in a SWCNT [41]. This is shown in figure 2.6a for a metallic SWCNT with $\nu = 0$, in figure 2.6b for a semiconducting type I SWCNT with $\nu = -1$ and in figure 2.6c for a semiconducting type II SWCNT with $\nu = +1$. The allowed wave vectors are plotted as vertical lines with their corresponding transition energy E_{ii} separated by $\Delta k = 2/d_{\mathrm{T}}$, where the index i enumerates the vHSs in the valence and conduction band on both sides of the Fermi level.
In the case of a metallic SWCNT as shown in figure 2.6a the trigonal warping effect leads to a lift of the degeneracy of the E_{11} transition into two nearby transition energies with the same distance to the K-point. The transition energy on the left of the K-point is slightly increased, while the transition energy on the right side of the K-point is slightly lowered.
For semiconducting SWCNTs as shown in figure 2.6b and figure 2.6c, the E_{11} transition is either on the left side of the K-point in the case of type I SWCNTs or on the right side for type II SWCNTs. In both cases the distance of the E_{11} transition to the K-point is equal, but due to the asymmetric warping decreased for type I SWCNTs and increased for type II SWCNTs. For the E_{22} transition the situation is reversed because this transition originates from the opposite side of the K-point, while the side alternates for higher transitions.
Because the trigonal warping effect slightly shifts the transition energies depending on the chirality of the SWCNT, it gives rise to a splitting of the transition energies for each family, allowing the assignment of the chiral indices for the investigated SWCNTs by resonant Raman spectroscopy (RRS) as will be shown in section 3.3.3. The trigonal warping effect is most prominent for zigzag SWCNTs with $\Theta = 0°$, while the trigonal distortions around the K-point become symmetrical to the allowed states for armchair SWCNTs with $\Theta = 30°$. This leads to the absence of the trigonal warping effect for these tubes, where the transition energies are proportional to $1/d_{\mathrm{T}}$.

2.4 Curvature effect

The zone-folding approximation neglects the effect of the SWCNT's curvature. This effect decreases with increasing tube diameter. On the one hand, the curvature of a CNT leads to smaller inter-atomic distances between the C atoms compared to graphene. Thus, for SWCNTs the interaction γ_0 in equation 2.7 between two neighboring π-electrons depends on the symmetry of the carbon bonds relating to the tube axis, which leads to the small bandgaps in semimetallic SWCNTs.
On the other hand, the curvature changes the bonds between the C atoms due to

rehybridization of the $\sigma\pi^2$-orbitals. To describe the degree of rehybdridization, Niyogi *et al.* introduced the pyramidization angle

$$\theta_{\mathrm{P}} = \theta_{\sigma\pi} - 90°, \tag{2.11}$$

which is defined as the difference of the angle $\theta_{\sigma\pi}$ between the in-plane σ- and the out-of-plane π-bonds in the trigonal configuration of graphene and 90° [42]. Graphene has a pure sp^2-character, where σ- and π-bonds are perpendicular to each other with the pyramidization angle of $\theta_{\mathrm{P}} = 0°$ as shown in figure 2.7a. In the tetrahedral sp^3 configuration as observed for diamond (figure 2.7b) the pyramidization angle increases to $\theta_{\mathrm{P}} = 19.47°$. Niyogi *et al.* showed that θ_{P} increases linearly with the reciprocal tube diameter $1/d_{\mathrm{T}}$ [42]. This leads to a mixture of the sp^2- and the sp^3-configuration as observed for C_{60} featuring a pyramidization angle of $\theta_{\mathrm{P}} = 11.4°$.
These structural deviations also cause deviations in the electronic structure of SWCNTs. Figure 2.7c and figure 2.7d show the band structure of a (10,0) SWCNT calculated by Reich *et al.* [43]. While figure 2.7c was obtained by a tight-binding calculation, which includes only π-orbitals, but neglects the curvature effect, figure 2.7d was calculated by an *ab initio* calculation. As a result the π^*-bands are significantly downshifted as shown in figure 2.7d for bands with $m = 0$ marked by red curves with black points. This is due to the mixing of σ^*- and π^*-bands induced

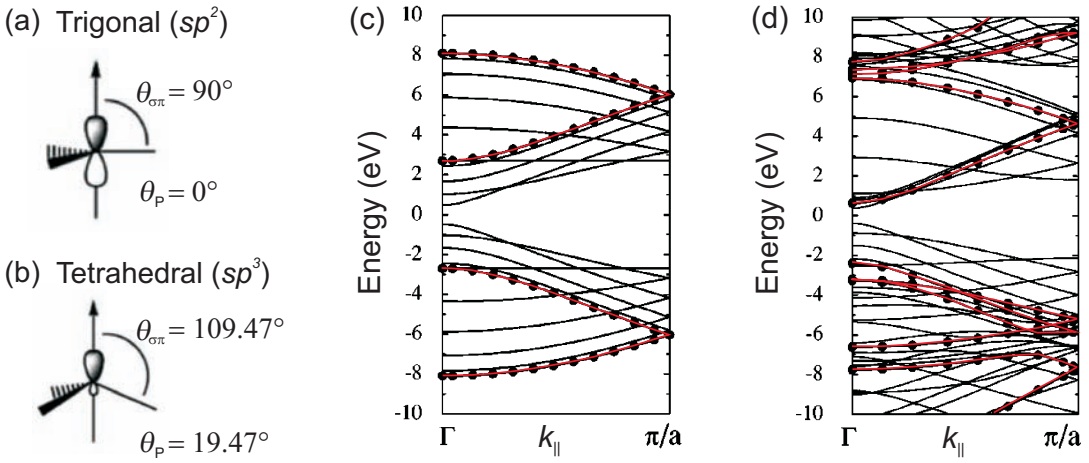

Figure 2.7: (a-b) Pyramidization angles for (a) the trigonal sp^2- and (b) the tetrahedral sp^3-configuration (taken from [42]). (c-d) Band structure of a (10,0) SWCNT calculated by (c) tight-binding approximation and (d) ab-initio calculation (taken from [43]). Red curves with black points mark the bands with $m = 0$. The downshift of the π^*-bands in the ab-initio calculation is due to the curvature effect.

by the rehybridization of the sp^2-orbitals, which was already calculated by Blase *et al.* in 1994 using *ab initio* local density functional calculations [44]. The curvature effect increases for smaller diameters of CNTs due to their increasing rehybridization. Furthermore, Kürti *et al.* showed that the curvature effect also depends on the chirality of the SWCNTs, while zizag SWCNTs are more affected than armchair SWCNTs [45], which can be explained by their different symmetries [43]. This shows that the changes in the band structure of SWCNTs induced by the curvature effect are increasing with smaller tube diameter d_T and smaller chiral vector Θ and thus vary for each (n_1, n_2) SWCNT.

2.5 Bundling effect

When several individual SWCNTs interact with each other, they show a strong tendency to align themselves axially forming bundles, which stick together by inter-tube van der Waals (vdW) interactions. A schematic example of a bundle of SWCNTs is shown in figure 2.8a, which shows the hexagonal formation of axially aligned SWCNTs. The distance between individual tubes in a bundle is approximately 0.34 nm, which equals the observed distance between individual layers in graphite [46].
As mentioned above, the curvature effect leads to the rehybridization of the sp^2-orbitals, which asymmetrically deforms the p-orbitals as seen in figure 2.7b. This increases the reactivity of SWCNTs as shown by Kürti *et al.*, which explains their strong tendency to form bundles [45]. Therefore, the electronic structure of SWCNTs is also expected to change in a bundle. Reich *et al.* calculate the band structure of an

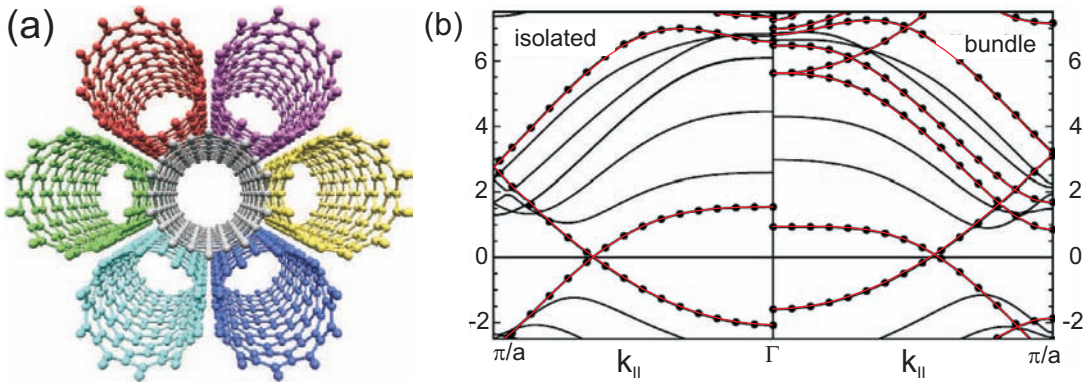

Figure 2.8: (a) Schematic alignment of a bundle of (6,6) SWCNTs. Individual SWCNTs are colored differently to gain a better overview. (b) Comparison of the electronic band structure of an isolated (left) and a bundled (right) (6,6) SWCNT (taken from [43]).

individual (6,6) armchair tube compared to a bundle of (6,6) SWCNTs as shown in figure 2.8b [43]. The calculation shows that the bundling effect leads to a further decrease of the separation between the conduction and the valence band around the Fermi level. These shifts of the band structure are most pronounced for the non-degenerate states, which are indicated by red curves with black points. These calculations are consistent with experimental results by Wang *et al.*, who observed for bundles a red-shift of tens of meV in the energy of their optical transitions, which were obtained by Rayleigh scattering [47]. Since the symmetry of individual SWCNTs in a bundle is lowered, the degeneracy of states is lifted as shown for a doubly-degenerate state in figure 2.8b.

2.6 Multi-walled carbon nanotubes

In analogy to graphite, which consists of several graphene layers, multi-walled carbon nanotubes (MWCNTs) consist of several SWCNTs encapsulated one inside the other and bound only by weak inter-layer vdW interactions. Figure 2.9a shows as an example a double-walled CNT (DWCNT), which is the simplest form of a MWCNT consisting of a (5,0) SWCNT (colored grey) inside a (10,0) SWCNT (colored red). This arrangement of SWCNTs leads to a higher stiffness allowing a higher thermal

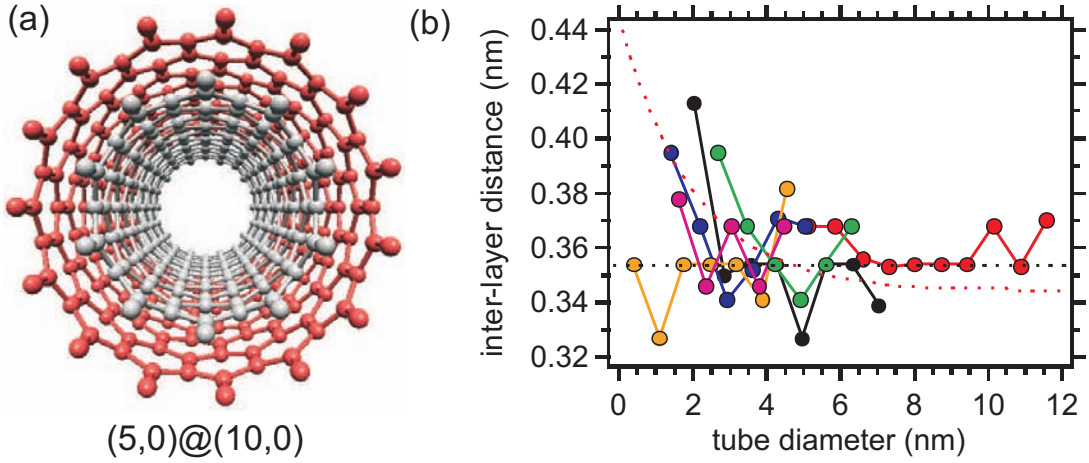

Figure 2.9: (a) Atomic structure of a DWCNT being the simplest form of MWCNTs consisting of a (5,0) SWCNT (colored grey) encapsulated by a (10,0) SWCNT (colored red), which is designed as (5,0)@(10,0). (b) Measured inter-layer distances for different MWCNTs compared to the predicted diameter dependence according to Kiang *et al.* [48] (red dashed curve). The measured inter-layer distances spread around a mean value of $d_\Delta = 0.35\,\mathrm{nm}$ (black dashed line).

stability of MWCNTs compared to SWCNTs [49].
In general SWCNTs with different chiralities can form a MWCNT as long as the diameter of the inner tube is small enough to fit inside the outer tube. As we will see in chapter 4, MWCNTs are formed during growth depending on the growth temperature and on the catalyst used.
The inter-layer distance between adjacent SWCNTs within a MWCNT is slightly larger than the inter-layer distance of $d_\Delta = 0.34\,\text{nm}$ observed for graphite due to the geometric and electronic perturbations induced by the curvature effect. Figure 2.9b shows the experimentally obtained inter-layer distance for different MWCNTs measured by high resolution transmission electron microscopy (HRTEM), where tubes belonging to the same MWCNT are connected by solid lines.
The curvature effect leads to a dependency of the inter-layer distance on the diameter of the tubes reported by Kiang *et al.* [48] resulting in rather small variations of around 0.08 nm for tube diameters between $d_\text{T} = 0.5 - 10\,\text{nm}$, which are plotted by the red dashed curve. Within the error of the measurement of $\Delta d_\text{T} = \pm 0.08\,\text{nm}$ no clear relation of the inter-layer distance to the tube diameter caused by the curvature effect could be resolved. This aspect will therefore be neglected. Instead, the measured inter-layer distance spread around a constant value of around 0.35 nm, which is consistent with the measured inter-layer distances of $d_\Delta = 0.35 - 0.37\,\text{nm}$ reported by Dresselhaus *et al.* [33].
Since MWCNTs consist of individual coaxial SWCNTs, their vibrational and electronic properties are strongly related to those of the participating SWCNTs, which are modulated by inter-layer vdW interactions regarding their dependence on the inter-layer distance. Surrounding layers act as a concentric potential that stabilizes the inner tubes. Thus, the innermost tubes can have a diameter, as small as $d_\text{T} = 3.4\,\text{Å}$, which would not be stable for an individual SWCNT due to its strong curvature [50]. On the other hand it induces a stronger σ-π-rehybridization of the inner tubes. Therefore, individual SWCNTs within a MWCNTs show a small down-shift of their π^*-bands induced by the increased curvature effect [51].

2.7 Peapods

Peapods are carbon nanotube hybrid structures consisting of fullerenes encapsulated in the inner hollow of SWCNTs or MWCNTs. This is shown in figure 2.10a for a (10,10) SWCNT, which is filled with C_{60} fullerenes forming a linear chain inside the SWCNT. The formation of a linear chain is the simplest ordering phase of C_{60} molecules within CNTs. Hodak *et al.* predicted ten different ordering phases of C_{60} in SWCNTs providing a diameter between 1.25 nm and 2.71 nm, which depend on the provided space of the inner hollow and therefore on the diameter of the encapsulating CNT [52]. For diameters between 1.25 nm and 1.45 nm a linear chain is expected, which transforms

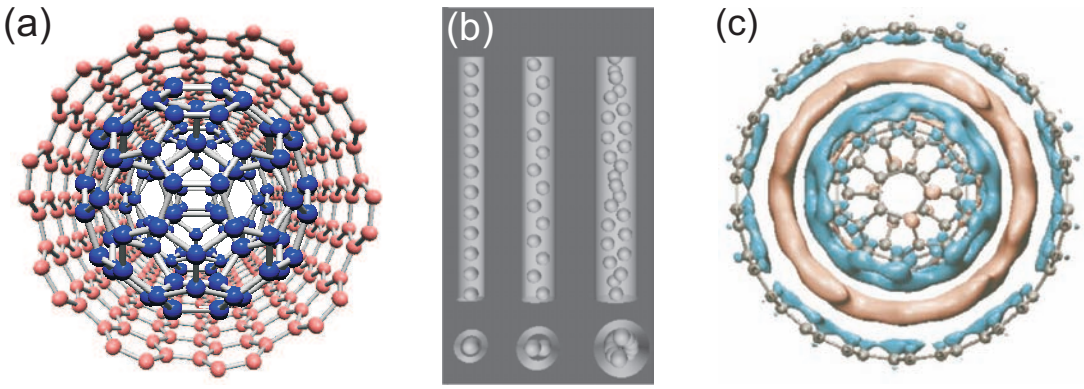

Figure 2.10: (a) Atomic structure of a peapod consisting of C_{60} molecules (blue atoms) encapsulated by a (10,10) SWCNT (red atoms) forming a linear chain. (b) Three most simple ordering phases of C_{60} molecules inside a SWCNT. With increasing diameter the linear chain phase transforms via a zigzag phase into a chiral phase (taken from [52]). (c) C_{60} molecule inside a (11,11) SWCNT. Pink and cyan surfaces denote the electron-rich or electron-poor regions (taken from [53]).

into a zigzag structure for diameters between 1.45 nm and 2.16 nm, while larger inner diameters show mostly chiral phases consisting of one or more helices as shown in figure 2.10b. Khlobystov *et al.* confirmed these predicted ordering phases experimentally for DWCNTs filled with C_{60} molecules [54].
The distance of adjacent C_{60} molecules in the linear chain phase is slightly smaller than in C_{60} crystals, but larger than for C_{60} polymers [55]. Thus, electron transfer along the chain of C_{60} molecules is expected. This also occurs between the encapsulated C_{60} molecule and the layer of the innermost CNT, as shown with density functional theory calculations by Okada [53]. They indicate that electrons are transferred from the π-orbitals of the C_{60} molecules and the SWCNTs to the space between them, leading to a local polarization of the peapod. This can be seen in figure 2.10c, which shows a C_{60} molecule inside a (11,11) SWCNT, where pink and cyan isosurfaces denote electron-rich and electron-poor regions. Thus, the electron density around the atoms in the CNTs is decreased leading to a slight decrease of the π^*-band. This effect could only be observed for CNTs slightly larger than a (10,10) SWCNT providing enough space between the interior C_{60} molecule and the inner layer of the encapsulating SWCNT, while calculations show that for $d_T < 1.25$ nm C_{60} molecules are axially deformed after the encapsulation [56].
If the diameter is smaller than $d_T = 1.25$ nm, the insertion of C_{60} becomes endothermic due to the required distortions of the encapsulating SWCNT. This minimum diameter is slightly smaller than the diameter of C_{60} ($d_{C_{60}} = 0.71$ nm) plus twice the van

der Waals distance observed for graphite ($d_\Delta = 0.34\,\mathrm{nm}$), which indicates small distortions of the C_{60} molecule and the encapsulating SWCNT. For the insertion of C_{60} inside MWCNTs, the minimum diameter is even lower, as observed for filled DWCNTs providing an inner average diameter of only $d_T = 1.13\,\mathrm{nm}$, which is due to the additional contributions of the several layers to the attractive part of the vdW interactions compensating the distortions of the inner tube [54].

2.8 Summary

SWCNTs show a variety of different atomic alignments depending on their chiral vector $\vec{C}_h$. These alignments result in different electronic properties, which can be calculated using the zone-folding approximation. SWCNTs can be divided into three different families determined by the family index ν, where SWCNTs with $\nu = 0$ are (semi)metallic, while SWCNTs with $\nu = -1$ and $\nu = +1$ named type I and type II are semiconducting.
The zone-folding approximation neglects the curvature effect, which arises from the rehybridization of the pure sp^2-orbitals in graphene due to the curvature of a SWCNT. This effect can be described by the pyramidization angle θ_P and is most prominent for SWCNTs with small diameters d_T and small chiral angles Θ. As a result the π-bands are downshifted significantly, which leads to a decreased bandgap.
The rehybridization increases the attractive vdW forces between individual tubes due to the asymmetric deformation of the π-orbitals, which leads to bundle formation and to a further decrease of the separation between the conduction and the valence band. Furthermore, a splitting of degenerate bands occurs due to the lowered symmetry in a bundle.
The electronic structure of SWCNTs within a MWCNT shows only slight changes compared to the band structure of an individual SWCNT, which are induced by the increased curvature effect due to the outer tubes forming a concentric potential for inner tubes. This effect also allows the formation of very small inner tubes, which would not be stable otherwise.
Peapods are hybrid structures consisting of SWCNTs or MWCNTs filled with fullerene molecules. Depending on the diameter of the innermost tube, different ordering structures could be observed for C_{60} molecules within CNTs. The interaction between the encapsulated C_{60} molecule and the innermost layer depends on their distance since it is dominated by vdW interactions. For larger distances a slight shift of the electron density, which is transferred from the tube and the C_{60} molecule to the space between them, has been calculated. Thus, the electron density around the atoms decreases, leading to a slight decrease of the band dispersion. For diameters below the minimum diameter of $d_T = 1.25\,\mathrm{nm}$, on the other hand, calculations show that encapsulated C_{60} molecules are axially deformed and induce distortions in the innermost layer of the

CNT.
Due to the strong electron-phonon coupling in CNTs, these fundamental electronic processes are essential for the interpretation of optical transitions as observed in Raman spectroscopy. In principle, the deviations of the observed Raman modes from the theoretical expectations allow the identification of different environments which slightly influence their electronic structure.

Chapter 3

Experimental methods

In the following chapter, the main experimental methods used in this thesis are introduced and discussed. These yield different information on the atomic and electronic structure of the investigated CNT and have specific advantages and limitations. Atomic force microcopy (chapter 3.1) and scanning electron microcopy (section 3.2.1) are used to probe the surface, transmission electron microscopy (section 3.2.2) to determine the structural assignment, and Raman spectroscopy (chapter 3.3) investigates the electrical properties of bulk material and individual CNTs.

3.1 Atomic force microscopy (AFM)

The AFM was developed by G. Binning *et al.* in 1986 [57]. A schematic assembly of

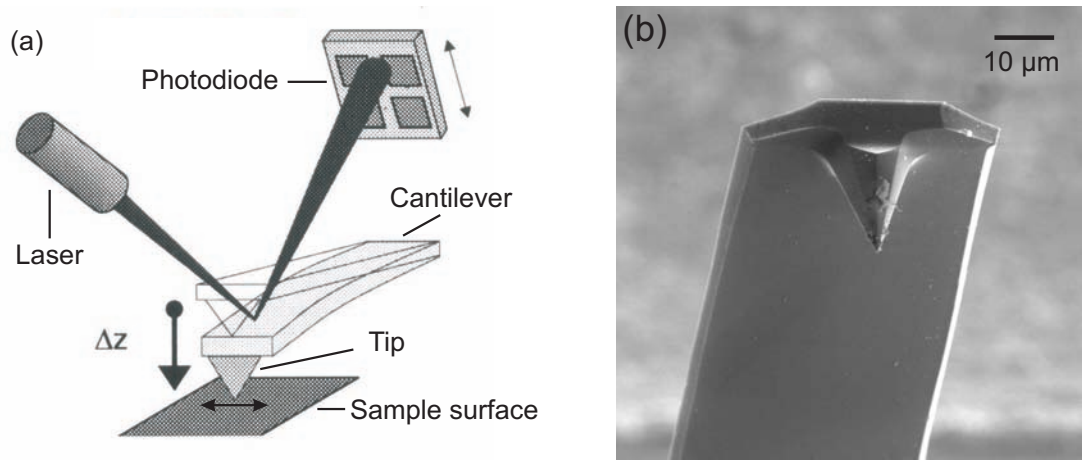

Figure 3.1: (a) Schematic assembly of an AFM (taken from [58]). (b) SEM image of the end of a cantilever showing its tip, which scans the sample surface (taken from [59]).

an AFM is shown in figure 3.1a. It consists of a cantilever with a sharp tip at its end. A closer view of a tip is shown in figure 3.1b. It points to the sharpness of the tip, featuring a diameter of about 0.5 µm at its top. When this tip is moved above the sample scanning the surface, it is deflected due to van der Waals (vdW) forces between the tip and the surface. The deflection is measured by a laser beam that is reflected from the cantilever into a segmented photodiode. Thus, the degree of deflection of the cantilever is measured by the photodiode and converted into a voltage. If this voltage is measured for each scanning point and plotted subsequently, a picture of the surface of the sample is obtained. The height of the sample can be measured with a high resolution of below 1 nm, which is more than 200 times better than the optical diffraction limit. The obtained lateral resolution depends on the density of scanned points per surface and the diameter of the tip.
Three different main operation modes exist for an AFM: the contact mode, the tapping mode and the non-contact mode. While in the non-contact mode the tip is not touching the surface, it is permanently touching the surface in the contact mode. The non-contact mode only works on hydrophobic samples or when the AFM is operating in vacuum environment. This is due to the adsorbed fluid layer that is covering the sample surface consisting mainly of adsorbed water molecules. When this adsorbate layer is too thick, the tip becomes trapped in it causing unstable feedback and scraping of the sample. In the contact mode, on the other hand, a force is applied on the tip, which directly interacts with the surface to overcome the interaction with the adsorbate layer. The disadvantage of this method is the scraping of the tip on the surface, which may induce damages. To avoid this, all measurements in this thesis are done in tapping mode. In this mode the cantilever is resonantly excited up and down by a small piezoelectric element mounted in the AFM tip holder. When the tip comes close to the surface, the amplitude of this oscillation is decreasing due to vdW forces, while the height of the cantilever above the sample is controlled by the piezoelectric actuator. During the scanning of the surface the height is adjusted to maintain a constant cantilever oscillation amplitude. In contrast to the contact mode, where the tip is permanently touching the surface, the tip only taps on the surface during scanning. Thus, the interactions with the surface are minimized, providing a non-destructive method to investigate the surface topology of a sample.
The microscope used (Digital Instruments) is placed on a vibration isolation system (MOD-1 M, Halcyonics GmbH) to avoid distortions of the scanning tip due to external vibrations. Flat surfaces like Si are needed to study the topology of individual CNTs and CNT bundles. The outer diameter of a CNT or a bundle can be determined by its measured height. This is in general a better sign for its diameter than its measured width, which is increased due to the moving tip during the scanning process providing a lateral resolution below 10 nm, while the height can be measured with an accuracy below 1 nm. Since AFM probes the topography of the sample, inner tubes of a MWCNT and individual SWCNTs within a bundle cannot be investigated.

3.2 Electron microscopy

The electron microscope is an optical analogue to the conventional light microscope. The first electron microscope was build by E. Ruska and M. Knoll in 1931 [60] which was further developed by E. Ruska in 1933, exceeding the resolution possible with an optical microscope [61]. An electron microscope uses a particle beam of electrons to probe a sample, which allows a greater resolution and magnification than for light microscopes, due to the smaller de Broglie wavelength. The de Broglie wavelength λ_e for relativistic electrons with the kinetic energy E is given by

$$\lambda_e \approx \frac{h}{\sqrt{2m_0E(1+\frac{E}{2m_0c^2})}} \tag{3.1}$$

with the Planck constant h and the rest mass m_0. The theoretical resolution of electrons with a kinetic energy of $E_{\text{kin}} = 100\,\text{keV}$ is about 4 pm, compared to the theoretical resolution of visible light of about 200 nm. This allows one to investigate individual molecules with diameters around 1 nm, e.g. carbon nanotubes. Instead of glass lenses like in the optical microscope, electromagnetic lenses are used which deflect the electron beam.
The first electron microscopes probe the sample in transmission and are therefore called transmission electron microscopes (TEM), which earned E. Ruska the Nobel price in 1986. In 1937 M. v. Ardenne was the first who tried to investigate a sample not in transmission but by scanning the sample surface and detecting the scattered secondary electrons created by the electron beam [62]. This different type of electron microscope is known today as a scanning electron microscope (SEM).
Both electron microscopy methods SEM and TEM are used in this thesis and will be discussed in section 3.2.1 and section 3.2.2.

3.2.1 Scanning electron microscopy (SEM)

A schematic assembly of a scanning electron microscope is shown in figure 3.2. The electrons are emitted by an electron gun with a kinetic energy of $E_{\text{kin}} = 8 - 30\,\text{keV}$, which are collimated by a condenser lens and afterwards focused by an objective lens, forming an electron spot of a few nm in diameter (blue lines). The beam is deflected in the x- and y-direction by a pair of scanning coils moving the electron beam from one side to the other over the samples surface just like the raster scanning performed with atomic force microscopy. In consequence, the lateral resolution of the SEM can never be better than the diameter of the beam scanning the surface.
If the electrons are capable of transferring enough kinetic energy to the sample, secondary electrons are emitted (red lines). Due to their low kinetic energy ($E_{\text{SE}} < 50\,\text{eV}$) secondary electrons only move a short mean free path before they get absorbed in the

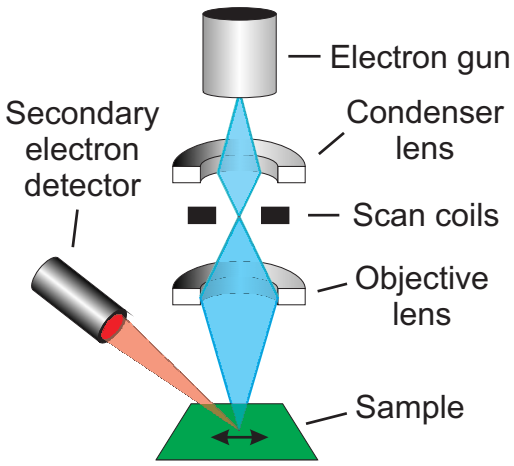

Figure 3.2: Schematic assembly of an SEM, which scans the surface with a focused electron beam. Primary electrons are colored blue, while secondary electrons are drawn in red.

sample, therefore the only secondary electron signals detected from the sample are those arising from the surface. This makes the secondary electron radiation extremely surface sensitive and therefore especially suited for surface visualization. The excited secondary electrons are measured in a secondary electron detector for each point of the scanned area, which is adjusted in a fixed angle to the surface.
The SEM technique provides a wide depth of focus, which enables a large vertical proportion of the sample to be in focus at the same time. Furthermore, the amount of electron scattering depends on the angle of the sample surface relative to the incident electron beam, which gives SEM images a three-dimensional appearance.
Figure 3.3a shows an SEM image of a hole in a perforated Si_3N_4 membrane which is overgrown by a network of CNTs. The light spots in the picture are caused by catalyst particles consisting of metal compounds having a larger atomic number. This increases the amount of secondary electrons due to the larger amount of weakly bonded valence electrons. On the other hand Si_3N_4 is a non-conductive material that leads to charging effects of the catalyst particles during electron irradiation, which further increases the amount of secondary electrons.
Since electrons are strongly scattered by their collisions with air molecules, the electron microscopes have to be run under high-vacuum conditions. When the residual pressure in the electron microscope is too high, hydrocarbon molecules decompose when interacting with the accelerated electrons. This leads to the creation of amorphous carbon, which is deposited on the CNTs. This is shown by the white arrow in figure 3.3b for a small region of an individual CNT that was imaged by SEM at a pressure of about

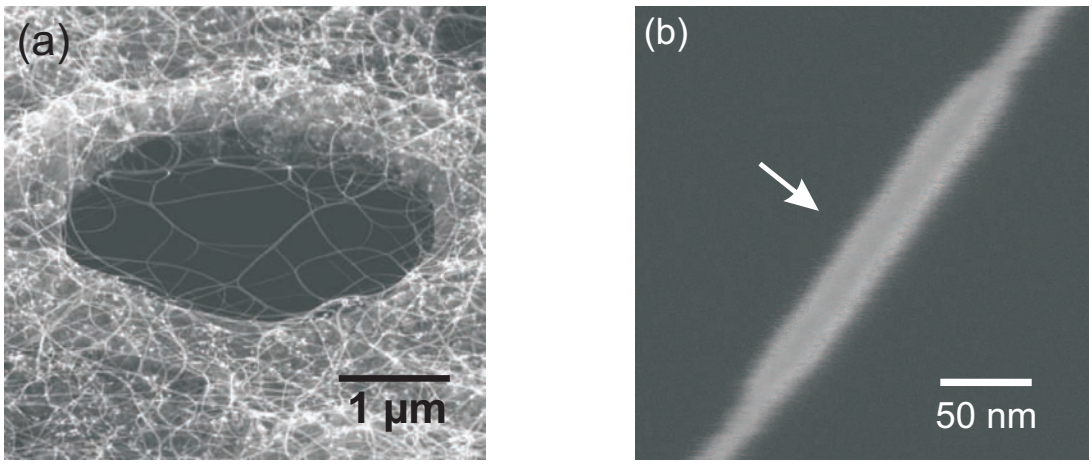

Figure 3.3: (a) SEM image of a hole in a perforated Si_3N_4 membrane which were measured with an angle of 60° between the surface and the detector. (b) SEM image of an individual CNT crossing the hole, which shows deposition of amorphous carbon after SEM measurement at $p = 10^{-6}$ mbar (white arrow). The kinetic energy of the incident electrons for both images was $E_{\mathrm{kin}} = 20\,\mathrm{keV}$.

$p = 10^{-6}$ mbar for several seconds. The blurring of this CNT is because of vibrations induced by electrical charging. To avoid the deposition of amorphous carbon on the surface of the CNTs, UHV-SEM measurements are carried out in a UHV-chamber with a base pressure of about $p = 10^{-10}$ mbar.

3.2.2 Transmission electron microscopy (TEM)

In TEM, the sample is measured in transmission directly behind the condenser lens as shown in figure 3.4, which requires thin or perforated samples. In contrast to SEM, which uses a convergent beam, a phase wave illumination is used, which is determined by the condenser lens (blue lines). Electrons with a kinetic energy of typically $E_{\mathrm{kin}} = 80 - 300\,\mathrm{keV}$ are used for materials science applications with a resolution below 1 Å. Due to the interaction of the electrons with the electrostatic potential of the atoms, electrons are scattered. The scattered electrons carry the information about the structure of the investigated sample (red lines). In TEM, the scattered beams are brought to interference in the image plane in order to form an image of the sample. The objective lens provides a fixed magnification, while the projector lens has variable magnification. Charge coupled device (CCD) cameras equipped with thin film scintillators are used for recording the interference images.
Primary electrons are detected, which are scattered by the sample, requiring larger ac-

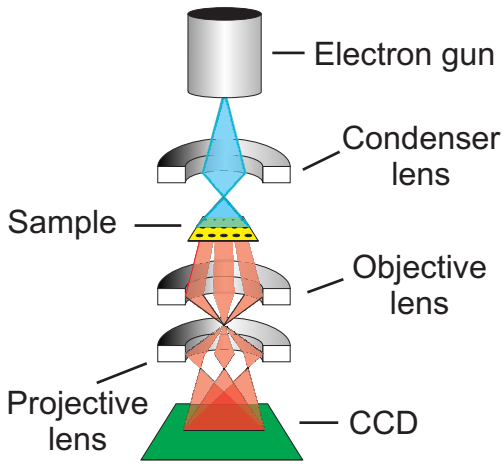

Figure 3.4: Schematic assembly of an TEM. Electrons are scattered by the sample, where primary electrons are colored blue and diffracted electrons are drawn in red.

celeration energies compared to SEM. The theoretical resolution depends on the energy of the electrons, allowing higher resolution for higher acceleration energies. Due to the larger acceleration voltage TEMs require with a base pressure below $p = 10^{-8}$ mbar a better vacuum than conventional SEMs, which also prevents electron induced deposition of amorphous carbon.
Because the sample is not scanned as for AFM or SEM, the resolution is theoretically only restricted by the de Broglie wavelength λ_e (equation 3.1). In reality it is reduced by aberration effects which can be distinguished into geometrical and chromatic aberrations. Chromatic aberrations are caused by the dependency of electron refraction on its kinetic energy in a magnetic field. This effect can be reduced by using energy filters to decrease the energy distribution of the electrons within the beam. Geometric aberration like the spherical aberration can be corrected by additional lenses. As illustrated in figure 3.5a, the refraction of the electrons depends on their angle to the optical axis. Thus, electrons that are scattered in the sample at high angles come to a focus in front of the Gaussian image plane. Therefore, a single point P of the investigated sample is broadened into a point-spread disc with radius R [63]. Spherical aberration is compensated by adding a suitable diverging lens right after the converging lens as shown in figure 3.5b, which corrects the larger deflection for larger scattering angles. This is achieved in high resolution (HR)TEM by a double hexapole system [65] resulting in a nearly ideal converging lens, that projects each point P of the sample to a single point of the image. For thin samples, a full compensation of wave aberrations is undesired: thin samples are phase objects and no contrast would

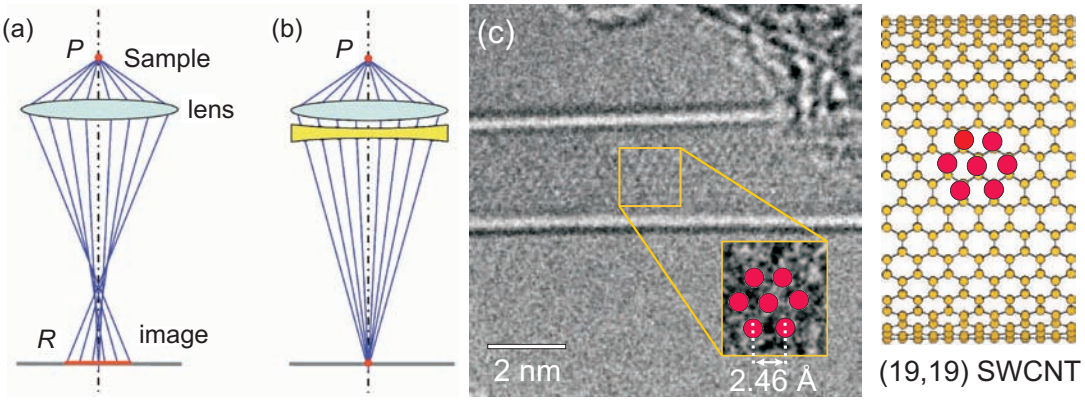

Figure 3.5: (a) Schematic illustration of the spherical aberration of a converging lens, which transforms a point P of the sample to a point-spread disc of radius R on the detector. (b) Compensation of the spherical aberration by adding a converging lens, which corrects the larger deflection for larger scattering angles (taken from [63]). Converging lenses can be realized in electron optics by a combination of multi-pole lenses. (c) Direct determination of the chirality of a SWCNT by HRTEM at 80 keV showing its high resolution allowing the investigation of single C-C bonds. This tube could be assigned as a (19,19) SWCNT, while its atomic structure is illustrated on the right side [64].

be seen if there were no aberrations. Therefore, in order to approximate a Zernike phase plate for phase contrast imaging, a small spherical aberration is balanced by an appropriately chosen defocus [66].
TEM measurements were carried out in cooperation with the AG Urban at the Ernst Ruska Centre (ER-C) in Jülich, where conventional TEM measurements were done in a Philips CM20 FEG instrument operated at 120 keV, while the HRTEM characterization was carried out in an FEI Titan 80-300 microscope equipped with a double-hexapole aberration corrector at an acceleration voltage of 80 keV. The corrector elements were adjusted to provide a negative value of the spherical aberration constant C_{40}. The particular choice of

$$C_{40} = -\frac{64}{27}\lambda_e^{-3} g_{\max}^{-4} = -52\ \mu\text{m} \tag{3.2}$$

balanced by a slight overfocus

$$Z = +\frac{8}{3}\lambda_e g_{\max}^{-2} = +12\ \mu\text{m} \tag{3.3}$$

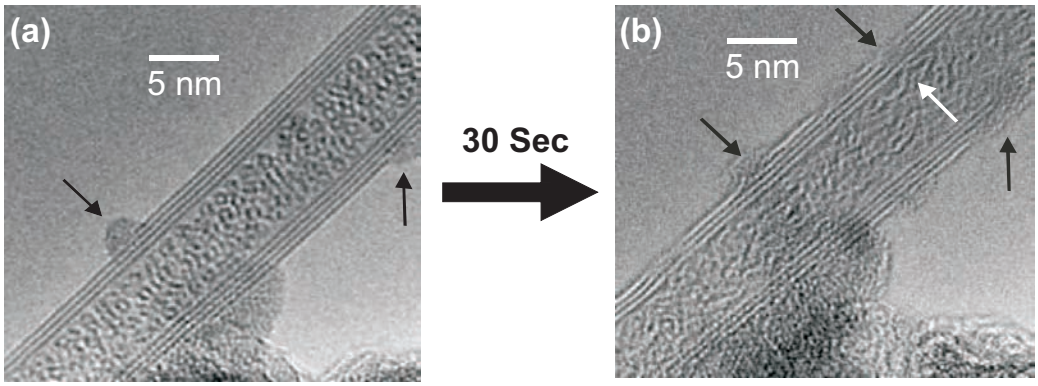

Figure 3.6: (a) First and (b) last image of a focus series measured with HRTEM at 80 keV. The time elapsed between image (a) and (b) is 30 seconds. Atoms appear black in under-focus (a), while they are white in over-focus (b). TEM induced defects (black arrows in (b)) preferably occur at pre-existing defects or deposited amorphous carbon (black arrows in (a)). The white arrow in (b) points at C_{60} molecules that coalesce forming a new inner layer.

extends the point resolution of the instrument up to its information limit

$$g_{\max} \approx 5 \text{ nm}^{-1}, \tag{3.4}$$

where λ_e is the electron wavelength at 80 keV [67]. These negative spherical aberration imaging conditions (NCSI) provide optimized phase contrast and directly interpretable bright atom contrast for the ease of structure interpretation [68]. Since the CNT structures investigated here are weakly scattering phase objects, NCSI imaging is particulary applicable and valuable for their direct study. This is shown in figure 3.5c, where the chirality of a SWCNT could be determined directly by its HRTEM image. This individual CNT was identified as a (19,19) armchair SWCNT [64]. Due to the strong electric potential of the C-C bonds that interacts with the accelerated electrons, not individual atoms but their bonds are highlighted with a distance of 2.46 Å. Because of the two-dimensional projection during HRTEM imaging the layers of the SWCNT appear as parallel lines, while their distance equals the diameter of the SWCNT.
It is well known that exposure to an electron beam can damage CNTs. It has been shown theoretically and confirmed experimentally that knock-on damage of unstrained C-C-bonds by the electron beam does not occur for energies below 86 keV [69]. If damage is seen at smaller electron energies, intrinsic or induced defects were present before the imaging. Figure 3.6 shows an individual MWCNT, that was filled with C_{60} molecules and has been investigated by a focus series at 80 keV. The total

irradiation time between the first image (figure 3.6a) and the last image (figure 3.6b) was 30 seconds. The black arrows in figure 3.6a point at pre-existing defects like amorphous carbon sticking on the outer layer and defects within individual layers. After 30 seconds, a destruction of the outer layer is clearly visible, marked by black arrows in figure 3.6b, and the damage occurs preferably at pre-existent defects sides. This finding is consistent to electron irradiation effects for isolated SWCNTs observed by Smith *et al.* [69], who could not observe defects induced by the electron beam for acceleration energies below 100 keV. Thus, at 80 keV no knock-on damage should be induced, while pre-existing defects grow during electron irradiation due to local heating of the sample [34].
Especially C_{60} molecules are affected by electron irradiation due to their stronger curvature compared to CNTs, and coalesce forming higher fullerenes [70]. This may even lead to the formation of new inner layers, which arrange in the vdW distance to the innermost layer as shown by the white arrow in figure 3.6b compared to figure 3.6a. This effect is comparable with the transformation of C_{60} molecules inside SWNTs into DWCNTs after annealing in vacuum above 900 °C [71].
To minimize these effects all HRTEM measurements in this thesis were done at 80 keV, while the intensity and the exposure time of the electron beam was minimized. However, the growth of pre-existent defects and the coalescence of individual C_{60} molecules cannot be avoided completely. Therefore, Raman spectroscopy is used as an additional characterization method, which allows a non-destructive characterization of individual CNTs.

3.3 Raman spectroscopy

Scattering of photons in molecules can be distinguished into elastic and inelastic scattering, which was first observed by C. V. Raman in 1928 [72], who received the Nobel prize for his discovery in 1930. Since vibrational information is specific to the chemical bonds and the symmetry of the molecule, Raman spectroscopy permits one to identify molecules by their characteristic set of phonon modes.
As illustrated in figure 3.7, Rayleigh scattering is the elastic scattering of a photon with the energy $h\nu$, which is absorbed exciting the molecule into a virtual state (blue arrows). The molecule relaxes to its initial vibrational state (red arrow), while a photon with the energy $h\nu$ is emitted, which equals the energy of the previously absorbed photon. Inelastic scattering occurs when the final state is different from the initial state. In the case of Stokes Raman scattering the molecule does not relax to its initial state, but to an excited vibrational state (green arrow) creating a phonon with the energy $h\nu'$. Thus, the emitted photon has a smaller energy of $h(\nu - \nu')$ compared to the absorbed photon. In contrast to that, the initial state of the Anti-Stokes Raman

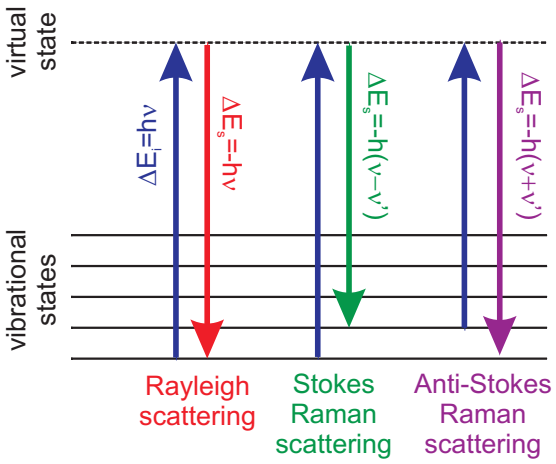

Figure 3.7: Illustration of elastic and inelastic scattering processes of phonons in molecules. Light induced transitions are shown by blue arrows, while Rayleigh transitions are red, Stokes transitions green and Anti-Stokes transitions purple.

scattering process is already an excited state. Therefore the molecule relaxes to a vibrational state with a smaller energy of $h\nu' < h\nu$ (purple arrow) and a photon with a higher energy of $h(\nu + \nu')$ is emitted. When monochromatic light is used for excitation e.g. by using a laser, these processes lead to frequency up- and downshifts, which can be observed in the Raman spectrum as Stokes and Anti-Stokes lines, respectively, providing information of phonon modes in the molecule. According to the Boltzmann distribution, ground states are primarily populated compared to excited states, which leads to a higher intensity of the Stokes Raman lines than the Anti-Stokes lines at room temperature. Therefore, all Raman spectra presented in this thesis which are measured at room temperature are investigated by Stokes Raman scattering.
Due to the small cross-section of Raman scattering of $10^{-28}\,\mathrm{cm}^2$ to $10^{-31}\,\mathrm{cm}^2$ [73], the intensity of the Raman peaks is much smaller than the elastic Rayleigh peak at the initial laser frequency, which can be suppressed by a notch filter.
Only those vibrations that are associated with a change of polarizability are Raman-active, while vibrations that are associated with a change of the dipole moment are IR-active. When the electric field of the incident light $E = E_0 \cos(2\pi\nu t)$ is interacting with a bond within the molecule, a dipole moment μ is induced depending on the polarizability α_0 of the sample given by

$$\mu = \alpha_0 E_0 \cos 2\pi\nu t. \tag{3.5}$$

If the molecule is vibrating with the frequency ν' associated with a change of the geometry and of the polarization, the resulting polarizability is

$$\alpha = \alpha_0 + \alpha' \cos 2\pi\nu' t + h.c. \tag{3.6}$$

leading to the dipole moment

$$\mu = \underbrace{\alpha_0 E_0 \cos 2\pi\nu t}_{\text{Rayleigh}} + \underbrace{\frac{1}{2}\alpha' E_0 \cos 2\pi(\nu - \nu')t}_{\text{Stokes}} + \underbrace{\frac{1}{2}\alpha' E_0 \cos 2\pi(\nu + \nu')t}_{\text{Anti-Stokes}}, \tag{3.7}$$

which includes the frequencies of the elastic Rayleigh and the inelastic Stokes and Anti-Stokes scattering as shown in figure 3.7. It can be clearly seen in equation 3.7 that Raman scattering only occurs in the case of vibrations that change their polarizability ($\alpha' \neq 0$).

3.3.1 Confocal Raman spectroscopy

The confocal Raman setup allows one to selectively investigate specific small areas on the substrate. It was invented by M. Minsky in 1955, when he built a confocal scanning microscope to investigate human neurons [74]. The assembly of a confocal setup is shown schematically in figure 3.8. The beam of a laser (blue lines) is reduced in diameter by a pinhole and redirected by a dichromatic mirror into the microscope.

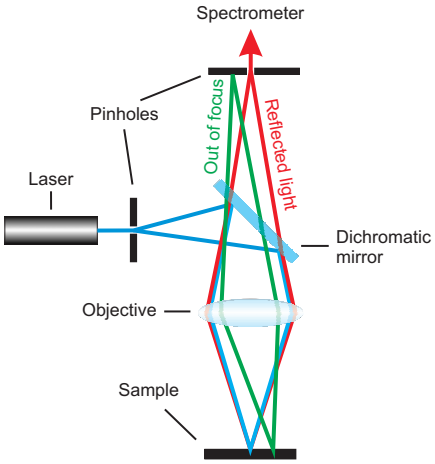

Figure 3.8: Schematic assembly of the confocal Raman spectroscopy. The spatial resolution is increased by placing a second pinhole before the spectrometer, which blocks points, that are out of focus (green lines), while points, that are in focus (red lines) can pass.

The objective focuses the laser beam onto the sample resulting in a spot diameter of approximately 1 µm, which allows one to measure single molecules. The reflected light (red lines) passing the dichromatic mirror enters a second pinhole, which blocks light scattered from points of the sample, that are out of focus (green lines). This increases the spatial resolution and avoids background blurring, leading to an optimized signal-to-noise ratio in the observed Raman spectrum. Afterwards the reflected light is analyzed with a spectrometer, which consists of a triple monochromator. The first and second monochromator provide the reduction of diffuse light acting as a band pass filter, while the third monochromator diffracts the light and projects the range of interest onto a nitrogen cooled CCD. All spectra are calibrated using a neon lamp. Frequency dependent Raman measurements were done in cooperation with the AG Thomsen at the TU Berlin using a Dilor XY 800 triple monochromator providing a spectral resolution of $0.1\,\mathrm{cm}^{-1}$ with an Ar-Kr laser, a dye laser or a Ti-Sa laser. The spectra are recorded depending on the wavelength by either using a Si or Ge based CCD. Confocal Raman measurements at a laser wavelength of 488 nm were done using a Jobin Yvon T64000 spectrometer providing a spectral resolution of $0.72\,\mathrm{cm}^{-1}$ excited by an Ar laser. Due to the small illuminated area of the sample, the photon flux interacting with the molecule is increased. Therefore, the laser power was limited to $P = 0.5\,\mathrm{mW}$ in all measurements to avoid thermal heating of the CNTs [75].

3.3.2 Fourier transform Raman spectroscopy

The first Fourier transform (FT) Raman spectrum was measured by Weber *et al.* in 1984 [76]. The core of an FT-Raman spectrometer is not a monochromator as in confocal Raman spectroscopy, but a Michelson interferometer as shown schematically in figure 3.9a. The laser beam reflected from the sample is split in two components labeled as I and II by a plate (P_1), which is coated with a semitransparent layer on its backside (S). Beam I is reflected by a fixed mirror (S_1) passing a second plate with equal diameter (P_2) twice to compensate the optical path difference between both beam components. Beam II is reflected by the semitransparent layer (S) and redirected onto a mirror (S_2), which is moving the range of a whole wavelength along the beam axis with a constant velocity v. By passing the semitransparent layer a second time, both beam components interfere and are redirected to the detector, where an interference pattern can be observed, as shown in figure 3.9b. After Raman scattering the monochromatic laser beam consists of waves with different frequencies as shown in the inset above, resulting in an intensity dependence on the position x of the moving mirror (S_2). Because of its finite number of points N with a distance Δx the discrete spectrum $S(k\Delta\nu)$ is calculated by discrete Fourier transformation (DFT) according to

$$S(k\Delta\nu) = \sum_{n=1}^{N-1} I(n\Delta x) \exp \frac{i2\pi k\Delta\nu n\Delta x}{N} \Delta x. \tag{3.8}$$

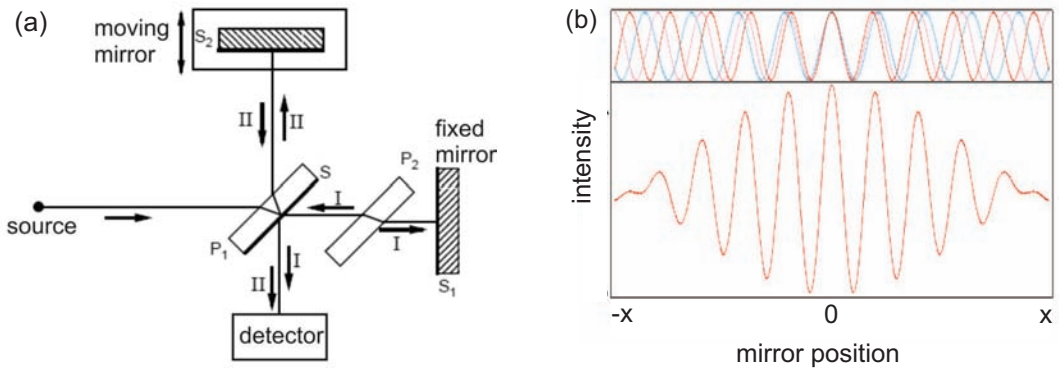

Figure 3.9: (a) Schematic assembly of a Michelson interferometer. (b) Measured interference pattern consisting of different frequencies due to Raman scattering of the monochromatic laser frequency at the sample.

The distance between two adjacent points in the spectrum

$$\Delta\nu = \frac{1}{N\Delta x} \tag{3.9}$$

determines the spectral resolution, which depends on the number N of measured points and on the length Δx of the path of the moving mirror.
The number of points can be increased by adding zeros to the beginning and the end of the interference pattern before the DFT (zero filling). This interpolation results in a smoothing of the obtained spectrum, but adds no additional frequency information. Due to its finite length, the interference pattern can be described as an infinite pattern which is multiplied by a rectangular function being 1 all along the measured interference pattern and rapidly decreasing to 0 at its borders. The Fourier transform of a rectangular function is the Sinc function, which shows additional side peaks creating artefacts in the resulting spectrum. This can be avoided by masking the interference pattern with an apodization function, which smoothes the pattern at its borders. This results in a decrease of the additional side peaks, but also increases the line width in the obtained spectrum, decreasing the spectral resolution. For all FT-Raman measurements presented in this thesis, the Blackman-Harris apodization function is used, which is optimized with respect to small line broadening and strong suppression of additional sidepeaks.
FT-Raman spectroscopy is done using a Bruker RAM II spectrometer providing a spectral resolution of $1\,\mathrm{cm}^{-1}$. It is equipped with a Nd:YAG laser with a wavelength of $\lambda = 1064\,\mathrm{nm}$ operating at a laser power of $P = 200\,\mathrm{mW}$. In contrast to the confocal setup the laser beam is not focused on the sample, resulting in a large illuminated area on the sample.

3.3.3 Raman spectroscopy of CNTs

CNTs can be identified by their characteristic phonon modes, which arise from their different atomic vibrations. Figure 3.10 shows an FT-Raman spectrum of a pristine

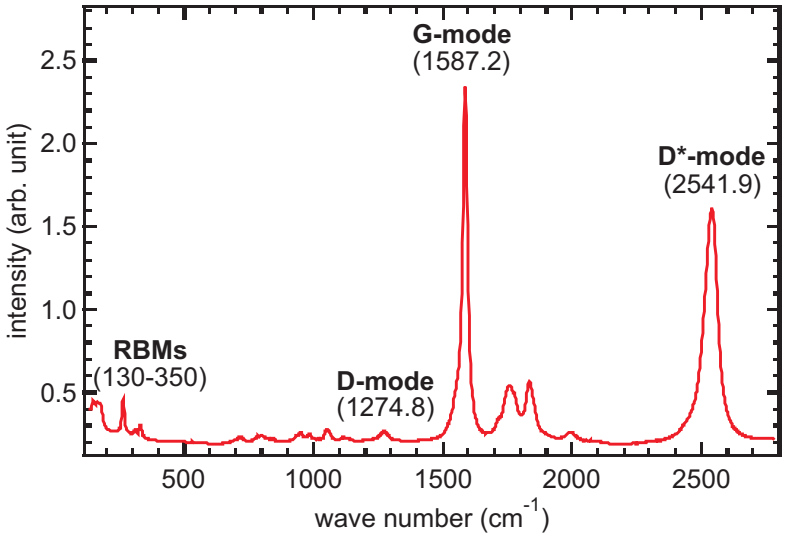

Figure 3.10: FT-Raman spectrum of a pristine bulk sample of CNTs measured at a laser wavelength of $\lambda = 1064\,\mathrm{nm}$ with its characteristic phonon modes.

bulk sample of CNTs, where the characteristic phonon modes are labeled with their name and their observed frequency. The radial breathing modes (RBMs), which are located between $130\,\mathrm{cm}^{-1}$ and $350\,\mathrm{cm}^{-1}$ and the most prominent G-Mode located around $1590\,\mathrm{cm}^{-1}$ are first order Raman transitions, while the D-Mode around $1275\,\mathrm{cm}^{-1}$ and its overtone the D*-Mode at around $2540\,\mathrm{cm}^{-1}$ are second order Raman transitions. In contrast to the first order modes, the latter show a strong energy dispersion [77]. Their exact position and intensity depends on the atomic structure of the investigated CNTs and will be discussed in the following in more detail. Intermediate modes that are not labeled are mixed phonon modes and are not of interest within the frame of this thesis. Due to the strong coupling of electronic states and phonon modes in CNTs, Raman spectroscopy probes both the phonon spectrum and the electronic structure of CNTs [33].

Resonant Raman scattering

Raman scattering is called resonant if the virtual state is replaced by a real electronic state. The excitation energy has to match the optical transition energy given by the separation of two corresponding vHSs in the DOS (see chapter 2.2). Due to the

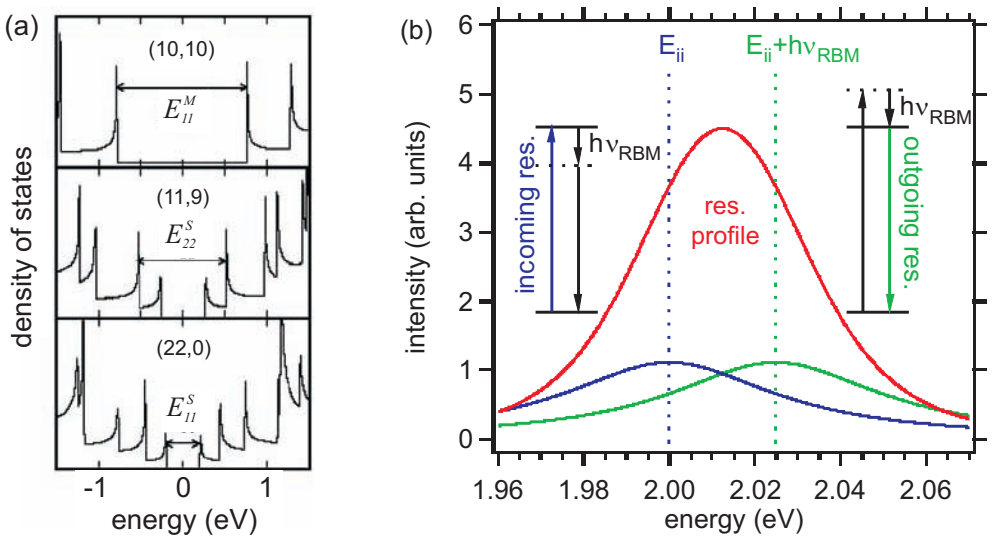

Figure 3.11: (a) Optical transitions occur between the i-th vHS above and below the Fermi-level, where M and S denote metallic and semiconducting CNTs respectively as shown for the calculated DOS of a metallic (10,10), chiral (11,9) and zigzag (22,0) SWCNT (taken from [78]). (b) Calculated resonance profile for an RBM (red) resulting from the incoming (blue) and the outgoing (green) resonance. Resonance transitions are illustrated for both resonances beside each peak, where virtual states and real states are drawn as dashed and solid lines respectively.

selection rules for optical transitions parallel to the tube axis, this is only allowed for vHSs with the same index i, as shown in figure 3.11a. It has to be noted that i is not equal to the quantum number m, which usually differs for different chiralities, changing the order of the bands in the DOS.
The singularities in the DOS lead to a strong resonance behavior, which is most pronounced for the RBMs. The intensity is increased in resonance by approximately a factor of 10^3 in comparison to the intensity for a non-resonance Raman process [77]. This allows one to measure the RBM of an individual SWCNT, where its resonance profile is a superposition of an incoming and an outgoing resonance described by

$$I(E_L) \propto \left| \underbrace{\frac{1}{E_L - E_{ii} - i\gamma/2}}_{\text{incoming resonance}} - \underbrace{\frac{1}{E_L - h\nu_{\text{RBM}} - E_{ii} - i\gamma/2}}_{\text{outgoing resonance}} \right|^2 \tag{3.10}$$

with the laser energy E_L, the optical transition energy E_{ii}, the observed RBM frequency ν_{RBM} and an equal width (FWHM) of both resonance curves γ [79]. The optical matrix elements are thereby assumed to be constant. As seen in equation 3.10, the incoming resonance occurs when $E_L = E_{ii}$, while the outgoing resonance occurs when $E_L = E_{ii} + h\nu_{\mathrm{RBM}}$, resulting in two nearby Lorentzian peaks. When the incoming and the outgoing resonance are not resolved in the measured spectrum a single peak is observed, which can be fitted according to equation 3.10 by

$$I(E_L) = \frac{A}{((E_L - E_{ii})^2 + \gamma^2/4)\,((E_L - 10^2 hc\omega_{\mathrm{RBM}} - E_{ii})^2 + \gamma^2/4)} \tag{3.11}$$

with a constant A, the Planck constant h, the speed of light c and the measured wave number of the RBM ω_{RBM} [80]. The resulting resonance profile is shown in figure 3.11b (red curve) arising from an incoming (blue curve) and an outgoing (green curve) resonance assuming a RBM wave number of $\omega_{\mathrm{RBM}} = 200\,\mathrm{cm}^{-1}$, a line width of $\gamma = 60\,\mathrm{meV}$ and a transition energy of $E_{ii} = 2.0\,\mathrm{eV}$. The corresponding resonance transitions are illustrated for both resonances in the insets beside each peak. The RBM features a relatively small resonance window of 8 meV for individual SWCNTs [81], 60 meV for individual SWCNT coated with SDS in an aqueous solution [79] and 120 meV for SWCNT bundles [75].
Since the chiral index completely characterizes the atomic and electronic structure of an individual SWCNT, its determination is of major importance for subsequent experiments on the same SWCNT. At optimal conditions the chiral index can be determined by HRTEM as shown in chapter 3.2.2. But due to the two-dimensional projection of the obtained images, this is difficult for MWCNTs, bundles or peapods. As will be shown in chapter 5, resonant Raman scattering (RRS) provides access to the diameter and the chiral index of individual SWCNTs within a bundle or MWCNTs. The RBM frequency alone will never be sufficient for an unambiguous chirality assignment, because it depends on the environment of the investigated SWCNTs. Therefore, the resonant excitation energy E_{ii} is needed as a second parameter, which can be determined with high accuracy according to equation 3.11 by resonance profiles of the investigated RBM. Furthermore, Raman spectroscopy is - in contrast to HRTEM - a non-destructive characterization method, which allows the investigation of individual SWCNTs prior to further experiments.

The radial breathing mode

The radial breathing mode (RBM) is located in the low-frequency region of the Raman spectrum with a linewidth of about $4\,\mathrm{cm}^{-1}$ for an individual SWCNT [82]. As explained above, it shows a strong resonance effect and can only be measured in resonance. It originates from a vibration with radial symmetry relating to the tube axis, where all carbon atoms within a SWCNT move outwards or inwards simultaneously.

This vibration is illustrated in figure 3.12 and is a characteristic phonon mode of CNTs

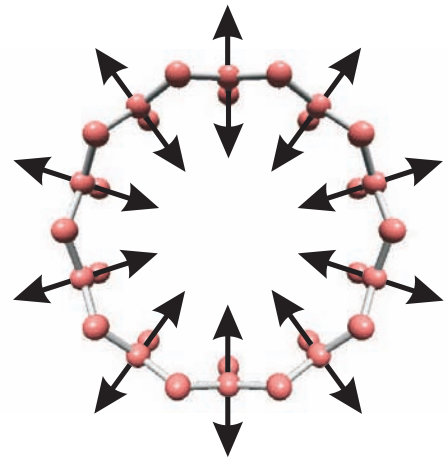

Figure 3.12: Illustration of the symmetric vibration causing the RBM. All carbon atoms vibrate simultaneously outwards or inwards in radial direction.

arising from the cylindrical structure of CNTs. As discussed in chapter 2.2 the optical transition energies E_{ii} are diameter dependent leading to a diameter dependency of the RBM as well. It disappears for graphite, which can be seen as a CNT with an infinite diameter with $d_T \to \infty$. Being a first order Raman effect, the frequency of the RBM ω_{RBM} is not dispersive and can therefore be used to estimate the diameter of investigated SWCNTs by

$$\omega_{RBM} = A/d_T, \tag{3.12}$$

where A is a constant sample-dependent parameter, which varies for different substrates. Thus, at a fixed wavelength, only tubes with a certain diameter are resonant. This is shown in the Kataura plot in figure 3.13a, which depicts the dependency of the transitions energies on the tube diameter for semiconducting (S) and metallic (M) SWCNTs for each chiral vector (n_1, n_2) [83] using equation 2.7 with $\gamma_0 = 2.9\,\text{eV}$ [77]. The energy transitions are separated by their families, where filled circles denote semiconducting type I ($\nu = -1$), open circles semiconducting type II ($\nu = +1$) and stars (semi)metallic SWCNTs ($\nu = 0$).
Due to their mirror symmetry perpendicular to the tube axis, only armchair CNTs show a purely radial vibration which is described by the $1/d_T$-dependency of the RBM frequency. All other chiralities $n_1 \neq n_2$ have a small axial component, which is largest for zigzag SWCNTs [36]. In this case the frequency of the RBM also depends on the chirality of the observed SWCNT, which leads to small deviations from its $1/d_T$-dependency due to the trigonal warping effect as discussed in chapter 2.3. This induces a spreading of the different families for higher energies and larger diameters, which split into different v-shaped branches as illustrated in figure 3.13b. Within a branch the branch index

$$\beta = 2n_1 + n_2 \tag{3.13}$$

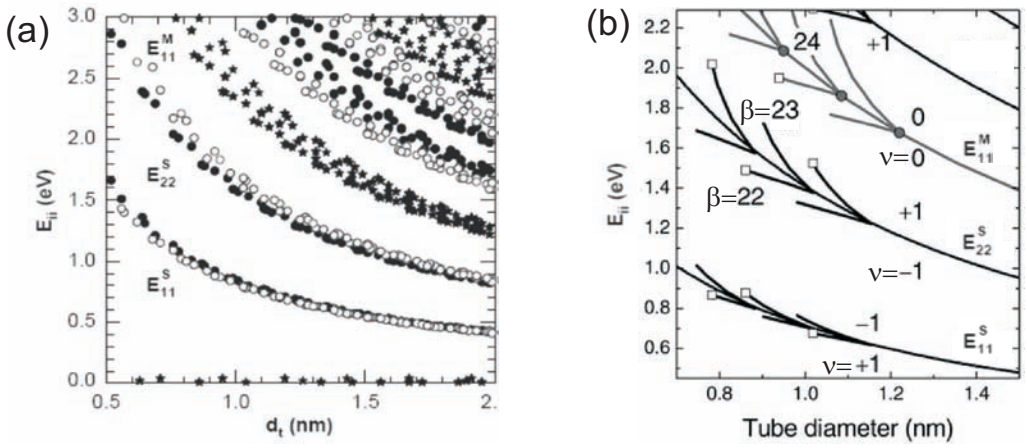

Figure 3.13: (a) Kataura plot showing the resonant transition energies depending on the diameter for semiconducting type I (filled circles), semiconducting type II (open circles) and metallic SWCNTs (stars) (taken from [77]). (b) Family branches of the Kataura plot for semiconducting (black) and metallic (grey) SWCNTs. Armchair SWCNTs are denoted by filled circles and zigzag SWCNTs by open squares. Different branches are labeled with their branch index β and their family index ν (taken from [36]).

is constant and the chiral index of a neighboring SWCNT with larger diameters is given by

$$n_1' = n_1 - 1 \quad \text{and} \quad n_2' = n_2 + 2, \quad n_1 \geq n_2 \tag{3.14}$$

for a SWCNT with the chiral index (n_1, n_2) [36]. Thus, armchair tubes which strictly follow the $1/d_{\mathrm{T}}$-dependence showing no splitting due to the trigonal warping effect, are located at the centers of the metallic v-shaped branches and are represented by filled circles in figure 3.13b. Zigzag tubes are represented by open squares and are located at the end of the branches. For the E_{11}^{S} transition semiconducting type I SWCNTs with $\nu = -1$ are up-shifted with increasing chiral angle, while semiconducting type II SWCNTs with $\nu = +1$ are down-shifted. This situation is vice versa for E_{22}^{S} transitions due to the trigonal distortions of the graphene band structure around the K-points and alternates for higher transition energies [36].
The splitting of the transition energies induced by the trigonal warping effect allows one to obtain the chiral index of individual SWCNTs by their RBM frequency and their optical transition energy. Especially for CNTs with large diameters and low transition energies the splitting of the family branches is rather small and requires a high precision in the measurement of the optical transition energy. This can be obtained by resonant profiles of individual RBMs using a tunable laser system as will be shown

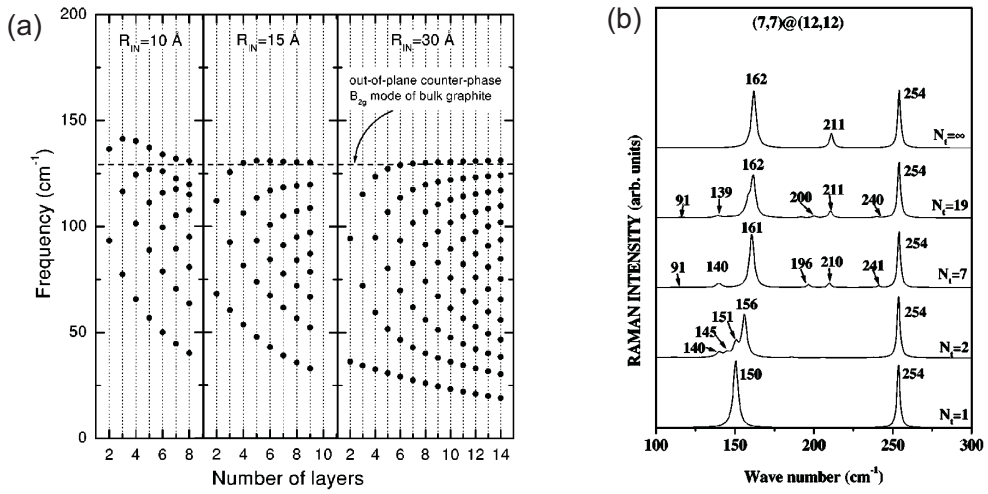

Figure 3.14: (a) Calculated BLM frequencies for MWCNTs with inner tube radii R_{IN} of 10 Å, 15 Å and 30 Å for increasing number of layers (taken from [84]). (b) Calculated spectra of (7,7)@(12,12) DWCNT bundles for increasing number of tubes N_t in the bundle (taken from [85]).

in chapter 5.

The RBM frequency of individual tubes within a MWCNT deviates from the $1/d_T$-dependence due to the coupling of individual RBMs caused by inter-layer vdW interactions. Thus, instead of individual RBM frequencies arising from the radial vibration of a specific SWCNT with a characteristic diameter according to equation 3.12, coupled breathing-like modes (BLMs) arise for MWCNTs [84]. Rahmani *et al.* calculated the BLMs for DWCNTs with different chiralities and could show that a low-frequency BLM and and a high-frequency BLM arise [85]. These can be assigned to in-phase and counter-phase motions of both tubes respectively, while the frequencies of the BLMs do not significantly depend on the chirality of the individual SWCNTs. Popov *et al.* calculated the BLMs for MWCNTs with more layers and observed intermediate modes of mixed character beside the in-phase and counter-phase mode [84]. The frequency of the BLMs is upshifted compared to the frequencies of the RBMs of individual SWCNTs, while the number of existing BLMs equals to the number of involved SWCNTs within a MWCNT. This is shown in figure 3.14a depending on the number of layers for different inner diameters R_{IN}. For larger numbers of layers and larger inner diameters the frequency of the counter-phase mode tends to the frequency of the acoustic out-of-plane B_{2g}-mode of graphite at $127\,\mathrm{cm}^{-1}$ (marked by a dashed horizontal line), while the in-phase mode is decreasing to zero for an increasing number of layers. For smaller inner diameters, the counter-phase mode of MWCNTs is sig-

nificantly higher than the B_{2g}-mode in graphite and decreases monotonically to this value for increasing number of layers.
The phonon coupling induces non-linear shifts of the BLMs, which depend on the eigenfrequencies of each contributing SWCNT. Thus, the frequency of the BLMs can only be obtained by numeric models as will be shown in chapter 6.
Coupling of phonon modes also occurs for bundles as mentioned in chapter 2.5, which leads to new phonon modes induced by the inter-tube coupling in bundles called bundle breathing like mode (BBLM) [85]. This is shown in the calculated Raman spectra in figure 3.14b for a bundle of (7,7)@(12,12) DWCNTs, while the number of DWCNTs in the bundle increases from $N_t = 1$ to $N_t = \infty$. The most prominent peaks are the BLMs originating from the (7,7) and the (12,12) SWCNTs, while the BLM of the outer tube is up-shifted due to the bundling effect. Between the two BLMs several weak peaks appear for $N_t = 2 - 19$, while the BBLM around $211\,\mathrm{cm}^{-1}$ is the most prominent one, which appears even in the spectrum of CNT crystals with $N_t = \infty$. According to Rahmani *et al.* this peak can be calculated by

$$\omega_{\mathrm{BBLM}} = \frac{A_{\mathrm{BBLM}}}{d_{\mathrm{outer}}} - C_{\mathrm{BBLM}} \tag{3.15}$$

with $A_{\mathrm{BBLM}} = 378\,\mathrm{cm}^{-1}\mathrm{nm}$ and $C_{\mathrm{BBLM}} = 16.5\,\mathrm{cm}^{-1}$ for given outer tube diameters d_{outer}. The experimental evidence for this mode will be discussed in chapter 6.2.
In general, the RBM allows one to completely characterize the atomic structure of investigated SWCNTs depending on the optical transition energy. This is even possible for MWCNTs and bundles when their special environment is taken into account. However, its rather small resonance window makes it difficult to observe the RBM for an individual CNT, and its intensity is rather small in bulk samples compared to the other phonon modes as shown in figure 3.10.

The G-mode

The G-mode, which is located around $1590\,\mathrm{cm}^{-1}$, is the most prominent peak in the Raman spectrum (figure 3.10) and arises from tangential vibrations of the C atoms against each other. In contrast to the Raman spectrum observed for graphite, where the G-Mode appears as a single Lorentzian peak at $1582\,\mathrm{cm}^{-1}$ [86], the G-mode splits into two components for CNTs. These two modes are labeled with G^- (red) and G^+ (blue) in figure 3.15a. They have their origin in vibrations perpendicular to (red arrows) and along (blue arrows) the tube axis respectively as shown in the inset. Due to the curvature effect, the bond length perpendicular to the tube axis depends on the diameter of the CNTs. Thus, the G^--mode shows a diameter dependency, while the G^+-mode is diameter independent as shown in figure 3.15b. The splitting between G^- and G^+ decreases for larger tube diameters and disappears for an infinite diameter,

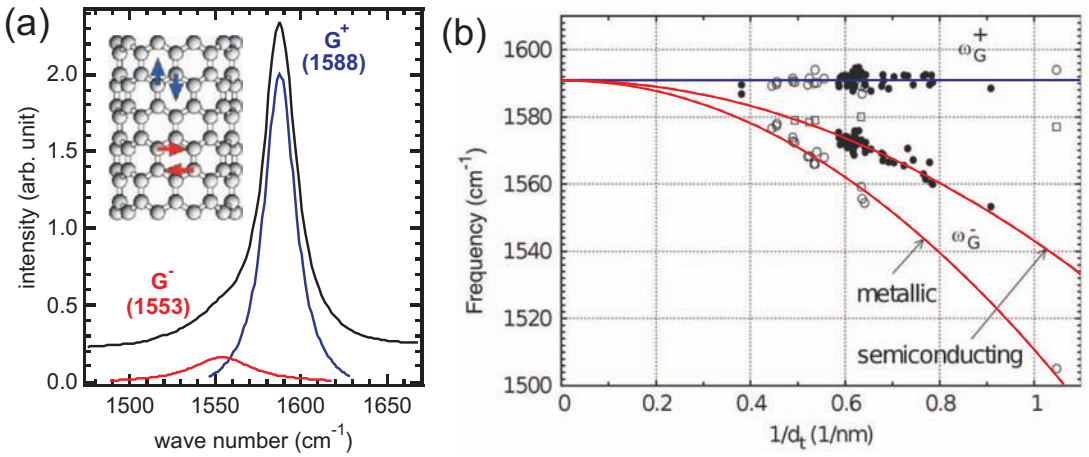

Figure 3.15: (a) G-mode of a bulk sample measured at a laser wavelength of $\lambda = 1064\,\mathrm{nm}$. The inset illustrates the vibrations of the G^-- and G^+-mode, which are fitted as red and blue curves respectively. The measured frequencies of both components are given in braces. (b) Diameter dependence of the frequency of the G^--mode ω_{G^-} and the G^+-mode ω_{G^+} for metallic (open circles) and semiconducting (solid circles) SWCNTs (taken from [77]).

which can be seen as an graphene sheet. According to Dresselhaus *et al.* the frequency of the G^--mode ω_{G^-} depending on the tube diameter d_T is given by

$$\omega_{G^-} = \omega_0^G + \beta/d_T^2 \tag{3.16}$$

with the position of the G-mode in graphite $\omega_0^G = 1591\,\mathrm{cm}^{-1}$ and $\beta = -45.7\,\mathrm{cm}^{-1}\mathrm{nm}^2$ for semiconducting and $\beta = -79.5\,\mathrm{cm}^{-1}\mathrm{nm}^2$ for metallic CNTs [77]. This equation makes a determination of the diameter of an individual CNT with small diameter possible, which show a resolvable splitting between G^- and G^+. For bulk samples the G^--mode is broadened, providing a nearly Gaussian line shape due to averaging over different diameters and types of CNTs. It appears as a small side peak of the G^+-mode as shown in figure 3.15a.
The difference in the atomic structure of CNTs leads to a different position of the G^--mode for metallic and semiconducting CNTs, as shown in figure 3.15b, but also changes the line shape of the G^--mode. While semiconducting CNTs show a Lorentzian line shape of the G^--mode, the line shape of the G^--mode is asymmetrically broadened and increased in intensity for metallic CNTs as described by the Breit-Wigner-Fano line shape [87]. Thus, also the electronic properties of individual CNTs can be determined by the G^--mode.

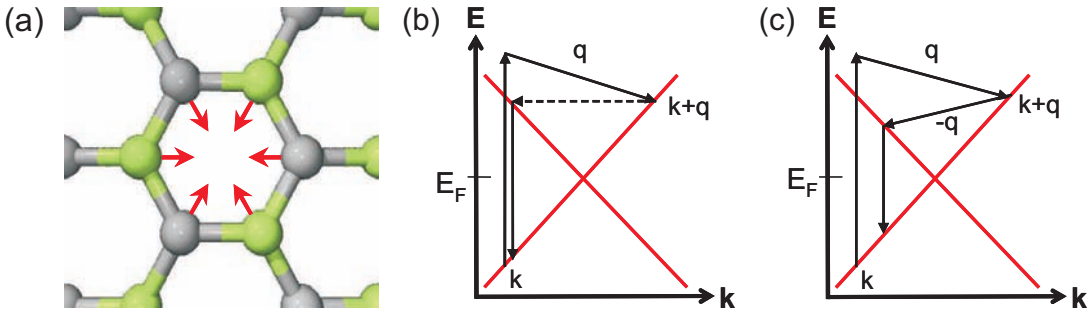

Figure 3.16: (a) Illustration of the vibration causing the phonon contributing to the D- and D*-mode. (b-c) Scheme of the double resonant scattering processes for (b) the D-mode arising from an inelastic (solid arrows) and an elastic (dashed arrow) phonon scattering process and (c) the D*-mode arising from two inelastic phonon processes around the K-point.

The D-mode and the D*-mode

The D and D*-modes are second order Raman transitions and arise from two scattering processes. They appear in the Raman spectrum around 1375 cm^{-1} and 2540 cm^{-1} respectively. The D- and the D*-mode arise from the phonon mode associated with the radial vibration of the C atoms against each other within a graphene hexagon as shown in figure 3.16a. In second order Raman processes, an electron is excited by absorbing a photon at a k-state, which is scattered to a $k+q$-state and afterwards back to a k-state before it recombines with a hole emitting a photon as shown in figure 3.16b and 3.16c. The scattering process of the D-mode (figure 3.16b) consists of an inelastic scattering event with scattering wave vector $\vec{q}$ (solid arrow) and an elastic scattering event (dashed arrow), while the D*-mode arises from two inelastic scattering events with scattering wave vectors $\vec{q}$ and $-\vec{q}$ (figure 3.16c). Thus, both modes arise from the same inelastic scattering event with scattering wave vector $\vec{q}$, which contributes twice to the D*-mode. Therefore, the D*-mode is called the overtone of the D-mode and appears approximately at the doubled frequency. It has to be noted that the D- and the D*-mode arise from inter-valley transitions around two neighboring K-points K and K' [88].
Elastic scattering is induced by defects of the graphene structure. Thus, the D-mode disappears for defect free structures like highly ordered pyrolytic graphite (HOPG) as shown in figure 3.17a. The D-mode is also called "defect-mode" and its intensity in the Raman spectrum increases linearly with the number of defects [33]. To obtain comparable values for the quality of a sample, the number of defects has to be related to the amount of carbon within the sample. This is done by the D/G-ratio, which is calculated by the intensity of the D-mode divided by the intensity of the G-mode being

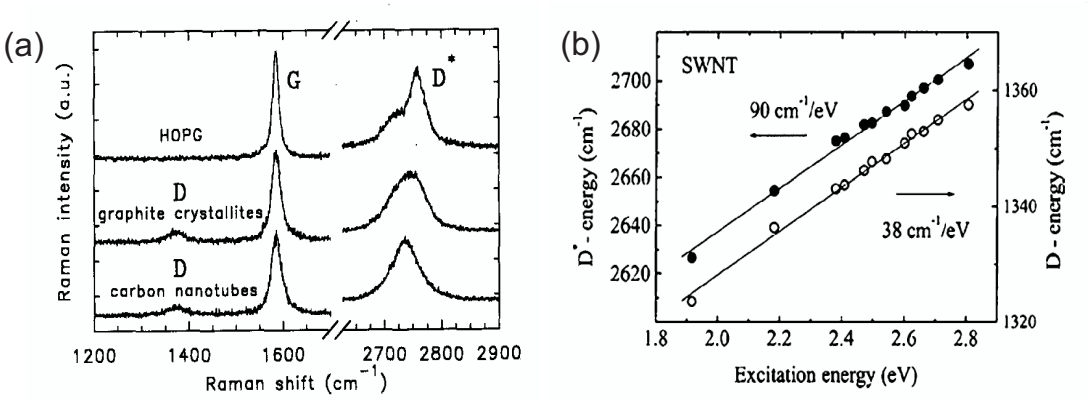

Figure 3.17: (a) Raman spectra showing the region of the D-, G- and D*-mode of highly ordered pyrolytic graphite (HOPG), graphite crystallites and carbon nanotubes (taken from [89]). (b) Energy dispersion of the frequency of the D- (open circles) and D*-mode (filled circles) being second order Raman processes (taken from [36]).

present for all carbon materials. Disordered carbon structures like amorphous carbon also show a strong D-mode, which makes the D/G-ratio an indicator for the purity of the CNTs [90]. The D/G-ratio is therefore used as a sign for the structural integrity of the CNTs and of the amount of amorphous carbon within a sample. However, these two origins cannot be discriminated by Raman spectroscopy alone.
The D*-mode on the other hand is independent of the quality of the graphite sample, but differs in shape and frequency for different amounts of graphite layers, as investigated by Ferrari *et al.* [91] and shown in figure 3.17a for HOPG compared to CNTs. Since the D*-mode arises from two inelastic electron scattering processes, it is strongly related to the electronic structure of the sample. Corio *et al.* showed that the D*-mode is up-shifted while applying a negative electronic potential to the sample, which induces a controlled up-shift of the Fermi-level [92].
This strong dependence of the frequency of the D*-mode on the electronic structure makes the D*-mode also sensitive to the bond length of the C atoms within the CNTs. This was shown by Cooper *et al.* for SWCNTs and MWCNTs after applying a surface strain, which slightly increases the bond lengths within the CNTs leading to a down-shift of the D*-mode. In contrast, he observed an up-shift of the D*-mode for SWNTs measured under external pressure due to slightly decreased bond lengths [93].
Due to the radial components of the phonon vibration shown in figure 3.16a, the D-mode and the D*-mode have a slight dependency on the tube diameter d_T. Both the D-mode and the D*-mode, being second order Raman processes, have additionally a strong energy dispersion as shown in figure 3.17b for individual SWCNTs [36]. Thus,

their observed frequency in the Raman spectrum depends additionally on the excitation energy used. According to Dresselhaus *et al.* the diameter dependency of the D-mode and the D*-mode at a laser wavelength of $\lambda = 514\,\mathrm{nm}$ is given by

$$\omega_\mathrm{D} = \omega_0^\mathrm{D} + A_\mathrm{D}/d_\mathrm{T} \quad \text{and} \tag{3.17}$$

$$\omega_{\mathrm{D}^*} = \omega_0^{\mathrm{D}^*} + A_{\mathrm{D}^*}/d_\mathrm{T} \tag{3.18}$$

with $A_\mathrm{D} = -16.5\,\mathrm{cm}^{-1}\mathrm{nm}$ and $A_{\mathrm{D}^*} = -35.4\,\mathrm{cm}^{-1}\mathrm{nm}$ for the D-mode and D*-mode respectively, where $\omega_0^\mathrm{D} = 1356\,\mathrm{cm}^{-1}$ and $\omega_0^{\mathrm{D}^*} = 2704\,\mathrm{cm}^{-1}$ are the values for graphene with $d_\mathrm{T} \to \infty$ [77].
Both second order Raman modes depend on various structural and electronic properties, which makes the interpretation of their observed frequencies difficult. But in correlation to the first order modes and to microscopic data, they provide additional information about the electronic and atomic structure of the investigated CNTs and their environment at a selected excitation energy.

3.4 Comparison of the methods used

In this chapter, the most important methods for the characterization of CNTs are discussed. They have different properties and feature different capabilities.
AFM provides the characterization of the diameter of CNTs, which are grown on flat substrates, but cannot characterize the inner structure of individual MWCNTs or CNTs in a bundle. SEM is also a surface sensitive microscopy method, but makes the investigation of CNTs grown over holes of perforated membranes possible, which are not accessible by AFM. To avoid the contamination of the samples with amorphous carbon created by the electron induced decomposition of hydrocarbon molecules, UHV-conditions are necessary. UHV-SEM as well as AFM using the tapping mode are non-destructive, which allows one to pre-characterize the morphology of substrates prior to further measurements.
For TEM, the samples are measured in transmission, which allows one to probe the inner structure of CNTs revealing their number of layers and their filling. Due to aberration correction, HRTEM features a spatial resolution that makes a investigation of individual bonds in CNTs possible, providing a tool for the direct determination of the chiral vector of a SWCNT. Perforated membranes are needed for HRTEM measurements because of the small contrast of C atoms arising from their small cross-section. Due to the high acceleration energy used by HRTEM compared to SEM, CNTs are damaged during electron irradiation, starting from pre-existent defects, even at acceleration energies below the knock-on damage. Therefore HRTEM is used to characterize individual CNTs grown over holes after prior Raman measurements providing a direct correlation of the microscopically determined molecular arrangements of CNTs and their resulting electronic structures.

Raman spectroscopy allows one to investigate individual CNTs on substrates by using a confocal setup focussing the laser beam to a small sample area or bulk samples by FT-Raman, where a large sample area is illuminated. This is not possible with the other mentioned characterization methods including confocal Raman spectroscopy, which only provide a small field of view, raising the possibility that the region analyzed may not be characteristic for the whole sample. It is difficult to interpret changes in the phonon spectrum, which are caused by a change of the electronic structure of the observed CNTs and may be induced by different effects. Nevertheless, Raman spectroscopy allows one to determine the family and the diameter of an investigated CNT and to selectively observe individual CNTs in bundles by using a resonant laser excitation. In the case of confocal Raman spectroscopy, the power of the laser must be limited to avoid damage to the CNTs caused by local heating.
Because of the complimentary information provided by each characterization method a correlation of these methods helps to get a better overview of the structure of investigated CNTs. Especially HRTEM is used to understand the influence of the structure on the phonon spectrum which may provide the usage of Raman spectroscopy as a additional pre-characterization method to probe the electronic structure of an individual CNT or peapod.

Chapter 4

Growth of carbon nanotubes

There are three main techniques used to synthesize carbon nanotubes: arc discharge, laser vaporization and chemical vapor deposition, which feature different possibilities and limitations that are discussed in the following.
The arc discharge method is the one by which CNTs were first investigated by Iijima *et al.* in 1991 [1]. It was developed by Krätschmer *et al.* in 1990 as a method for the mass production of fullerenes, which are produced by the evaporation of graphite rods in contact using an ac voltage in an inert gas (typically He) [94]. Fullerenes are generated from the evaporated anode in the form of soot in the chamber. Using TEM Iijima *et al.* found MWCNTs formed in the soot deposited on the cathode [1], while SWCNTs can be synthesized by doping of the anode with transition metal catalysts like Fe or Co [95, 96].
The laser vaporization method was developed by Smalley *et al.* to investigate the formation of carbon clusters, which led to the discovery of the C_{60} molecule in 1985 [97]. A graphite target is vaporized by a laser beam inside of a quartz tube, which is flushed with Ar at a constant flow rate and placed in a furnace (laser furnace method). Doping the target with catalyst particles allows for control of the diameter distribution of the produced CNTs [98].
Chemical vapor deposition (CVD) was used since 1959 for the production of carbon filaments and fibers. In contrast to the arc discharge and laser furnace method, no graphite is vaporized. Instead the carbon required for the CNT growth is provided by the thermal decomposition of hydrocarbon vapor, like methane. The growth of the CNTs occurs in the presence of a metal catalyst, which is suspended directly on a substrate. The diameter distribution of the synthesized CNTs can be influenced by the size of the catalyst particles and the reaction temperature [99]. This allows one to synthesize the CNTs directly on a substrate offering some control over the position of the CNTs.
For electronic applications the CNTs synthesized by arc discharge or laser vaporization are suspended in a solvent, purified and dispersed on a substrate from solution before contacts are fabricated on the individual CNTs for measurements [20, 100, 101]. This

processing suffers from several disadvantages: It does not allow the controlled positioning of the nanotubes, the CNTs often cluster together in ropes, and the CNTs are rather short ($< 1\,\mu m$) due to the sonication involved. Especially the latter inhibits the fabrication of more complicated device structures as needed for, e.g., double quantum dots [102] or high-frequency irradiation [103]. On the other hand, CNTs synthesized by chemical vapour deposition (CVD) directly on substrates can be grown individually on predefined sites with lengths of several micrometers, which allows one to manufacture electronic devices [25]. Since the characterization of the CNTs should be correlated with later transport measurements on real devices, the CNTs investigated in this thesis are synthesized by CVD.

4.1 Synthesis of carbon nanotubes using CVD

Carbon nanotubes are grown directly on substrates using CVD, after [25]. The catalyst is suspended in methanol, dropped onto the substrate with a pipette and dried afterwards in a nitrogen flow. The substrate is then heated at 120 °C for 15 minutes to remove solvent residue.
The yield of CNTs after CVD growth can be controlled by the amount of catalyst particles on the substrate. Therefore only a few drops of the suspended catalyst particles were used for the investigation of individual CNTs, while bulk samples were completely covered with the suspended catalyst particles, skipping the blow-drying process. Instead, the suspension is dried using a heating plate at 100 °C. For samples with a high yield of synthesized CNTs, they form bundles due to the van der Waals interactions between their outer shells, stabilizing themselves in networks.
For CVD growth the substrate is placed inside a quartz glass tube, which is located in a furnace as shown schematically in figure 4.1a. The substrate is heated up to temperatures between 860 °C and 1030 °C in a constant Argon flow of 1.52 l/min to

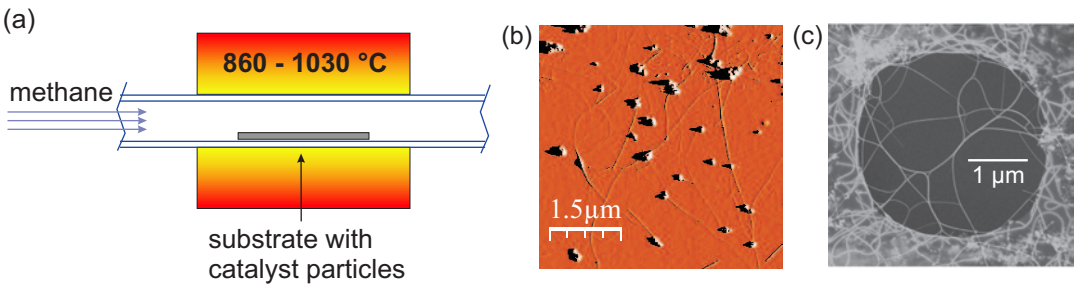

Figure 4.1: (a) Schematic assembly of the CVD system using methane as source gas. (b) AFM picture of CNTs grown on a Si substrate after CVD growth. (c) UHV-SEM picture of CNTs crossing a hole of a perforated Si_3N_4 substrate during CVD growth.

prevent the oxidation of catalyst particles prior to the CNT growth. After reaching the desired reaction temperature T_{CVD}, hydrogen is added at a flow rate of 0.7 l/min. The argon flow is stopped and methane at a flow rate of 0.52 l/min is inserted for 10 minutes, acting as the carbon-source. During this time methane inside the furnace is decomposed according to the reaction

$$\mathrm{CH_4} \longleftrightarrow \mathrm{C} + 2\mathrm{H_2} \tag{4.1}$$

providing carbon atoms for the growth of CNTs [104]. Afterwards, the methane and hydrogen flow is stopped and argon added at the same flow rate as mentioned above to provide a cool-down of the substrate to room temperature in an inert gas atmosphere. After the CVD process CNTs with length up to several micrometers can be observed, as shown for a Si substrate by AFM in figure 4.1b. The CNTs grow away from the catalyst particles being spread upon the substrate. On perforated Si_3N_4 membranes some CNTs bridge the holes, so that they are accessible for TEM as shown by UHV-SEM in figure 4.1c.

4.2 Substrates

Four different kinds of substrates are used for the CVD growth in order to investigate the synthesized CNTs with different characterization methods:

1. Substrates cut from Si/SiO_2 wafers were used for the AFM measurements due to their flatness (see figure 4.1b). The same substrates were used for patterning with electron beam lithography, which allows one to place the catalyst particles at predefined sites to investigate an individual CNT with different characterization methods and to contact the CNTs after CVD growth.

2. Quartz glass substrates are chemically inert when in contact with most acids and were therefore used for the acid treated samples. For comparison also oxidation by heating in air was done with these substrates and studied by using FT-Raman spectroscopy.

3. Due to their conductivity, Mo substrates can be investigated using UHV-SEM and correlated with FT-Raman measurements providing a high reflectivity, but their roughness prohibits AFM measurements.

4. In order to correlate HRTEM with other typical methods to characterize the structure of CNTs like UHV-SEM and confocal Raman spectroscopy, the CNTs are grown on perforated Si_3N_4 membranes with a hole diameter of $2-3\,\mu\mathrm{m}$ and a hole pitch of about $3-4\,\mu\mathrm{m}$. The thickness of the membrane is 200 nm, and they are mounted on a Si frame with a thickness of 300 µm with a window area of

0.5 mm (DuraSiN™, Protochips Inc.). During the CVD process, the CNTs cross these holes either individually or in ropes forming networks (see figure 4.1c). Thus, depending on their yield, freely suspended individual or bundled CNTs can be observed without tube-substrate interactions. The membrane itself can be marked by focused ion beam (FIB) allowing the investigation of selected individual CNTs. These substrates may also be used in a lithography process.

4.3 Growth mechanism

Due to very strong C-H bonds in the methane molecule (440 kJ/mole), its thermal decomposition occurs at very high temperatures (>1200 ℃) [105]. Various transition metal catalysts like Ni, Fe or Co have been used to reduce the temperature of methane thermal decomposition [106]. Thus, methane dehydrogenates locally at the catalyst particle sites. The carbon is absorbed by the liquid metal particles until a super-saturation point is reached and carbon precipitates out from the particle surface. Figure 4.2 illustrates the growth mechanism suggested by Gavillet *et al.*, who based their concepts on the vapor liquid solid (VLS) model [107]. Further absorbed carbon continues to assemble on the surface of the supersaturated metal particle (figure 4.2a). It either nucleates to CNT caps (figure 4.2c) forming long SWCNTs (figure 4.2d) when the carbon supply at the root continues, or grows layer-by-layer around the metal particle leading to an over-coating and therefore to the deactivation of the metal particle (4.2b). Due to an oversupply of carbon, this can also occur after SWCNTs have formed, stopping the growth after a short time (figure 4.2e and 4.2f). This results in rather short tubes as shown in the HRTEM picture in figure 4.2g. In this case the growth of a CNT was interrupted due to the over-coating of a catalyst particle with

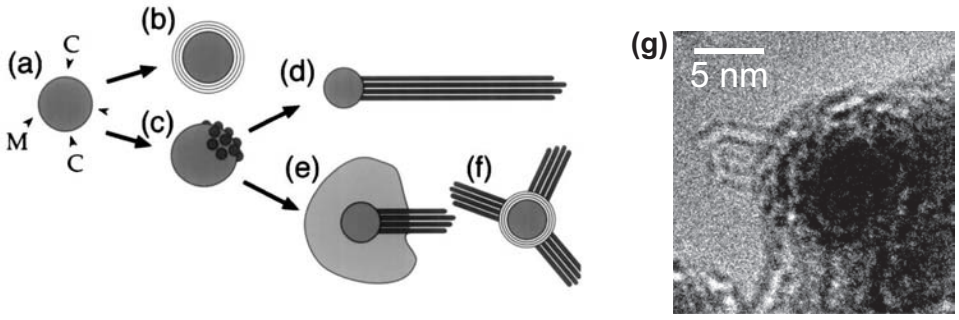

Figure 4.2: (a-f) Different phases of the VLS growth process (taken from [107]).
(g) HRTEM picture of a cap of a CNT, that is grown away from a deactivated catalyst particle.

amorphous carbon.
When a cap is formed that is large enough, more caps can grow underneath the first forming graphitic shells spaced by roughly the inter-layer distance of graphite, which leads to the formation of MWCNTs [108].

4.4 Fe:Mo alloy catalysts

Metal alloy catalysts like Fe:Mo prevent catalyst particle aggregation and improve the growth of CNTs due to intermetallic interactions between Fe and Mo enhancing the activity of the catalyst [109]. A variety of known Fe:Mo alloy catalysts were created as listed in table 4.1, which were suspended in methanol by sonication for four hours and kept for 24 hours to let the sediment settle down.
Alumina and magnesia are reported to be better catalyst supports than silica due to their strong metal-support interaction allowing high metal dispersion and therefore high density of catalytic sites [110, 111]. This additionally prevents aggregation of the metal particles during CVD synthesis, forming large clusters, which leads to greater diameters of synthesized CNTs [112]. Both magnesia (Cat 1 and Cat 5) and alumina nanoparticles (Cat 2, Cat 3 and Cat 4) were used as catalyst supports for the metal alloy catalysts, where Mo is provided by Molybdenum(IV)dioxide(acac)$_2$ and Fe by Iron(III)nitrate (Cat 1 and Cat 2) and Iron(II)acetylacetonate (Cat 4 and Cat 5). In Cat 3 Fe and Mo are provided by a spherical molecule, a so-called Polyoxometallate (POM), with a diameter of ∼2.5 nm, forming a Keplerate-type structure of icosahedral symmetry, as shown in figure 4.3a. Each FeO_6 coordination polyhedron is connected

Name	Fe:Mo alloy catalyst	support material
Cat 1	19.7 mg $Fe(NO_3)_3{\cdot}9H_2O$ 2.5 mg $MoO_2(C_5H_5O_2)_2$	15.2 mg MgO
Cat 2	20.2 mg $Fe(NO_3)_3{\cdot}9H_2O$ 2.6 mg $MoO_2(C_5H_5O_2)_2$	15.5 mg Al_2O_3
Cat 3	32.3 mg $[Mo_{72}Fe_{30}O_{25}(CH_3COO)_{12}(Mo_2O_7\ (H_2O)_2)$ $(H_2Mo_2O_8\ (H_2O))\ (H_2O)_{91}] \cdot 140H_2O$	15.5 mg Al_2O_3
Cat 4	20.5 mg $C_{10}H_{14}FeO_4$ 2.4 mg $MoO_2(C_5H_5O_2)_2$	15.2 mg Al_2O_3
Cat 5	20.2 mg $C_{10}H_{14}FeO_4$ 2.4 mg $MoO_2(C_5H_5O_2)_2$	15.3 mg MgO

Table 4.1: Chemical composition of the used catalysts dissolved in 15 ml methanol.

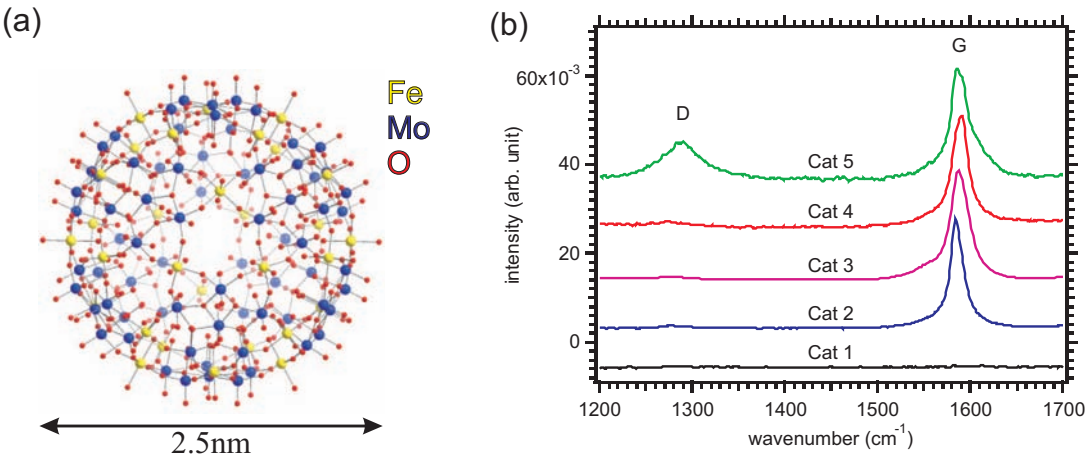

Figure 4.3: (a) Atomic structure of the used molecular nanoclusters. For a better clarity included water molecules are not shown. (b) Comparison of the intensity of the D-mode for different catalysts normalized to the G-mode.

to two MoO_6 octahedra of two neighboring Mo_6O_{21} pentagons, which were synthesized after Müller *et al.* [113] by P. Kögerler and coworkers. Water molecules are also included inside the molecule, which are not shown in figure 4.3a, but help to stabilize its structure at room temperature. It decomposes during the CVD process, giving access to both Fe and Mo, respectively and may, due to its selective size, allow a diameter selective growth of CNTs [114]. This would help to increase the homogeneity of bulk samples and to investigate specific ordering phases of C_{60} inside individual CNTs after filling.

Directly before the CVD growth, the catalyst suspension is sonicated for 10 minutes followed by 10 minutes of settle-down time, where big catalyst particles descend and settle down, while small particles stay in suspension.

In the following the CVD growth of CNTs from these different catalysts is investigated. Bulk samples are grown on Mo substrates at a growth temperature of $T_{\mathrm{CVD}} = 950\,^{\circ}\mathrm{C}$ and measured by using FT-Raman spectroscopy as shown in figure 4.3b, where for all catalysts beside Cat 1, the characteristic Raman spectrum of CNTs could be observed. The smallest D/G-ratios could be investigated for CNTs grown using Cat 2, Cat 3 and Cat 4, which use alumina as catalyst support, where the usage of Cat 4 results in a smaller yield compared to the two other catalysts. For Cat 3, no diameter selective growth compared to Cat 2 could be investigated, which was indicated by the observation of multiple RBMs in the FT-Raman spectrum and additional AFM measurements given in [115].

No CNTs could be synthesized using Cat 1, which includes magnesia as catalyst support. Furthermore, Cat 5, which also uses magnesia as catalyst support, shows the

highest intensity of the D-mode for all investigated samples, while all alumina supported catalysts show only a small D-mode. Thus, alumina is the preferred support material allowing growth of CNTs with a high crystalline order and without the formation of amorphous carbon.
To further study the influence of the support material, CNTs are grown on Si and Mo substrates using Cat 3 with and without the alumina support material and are investigated by AFM and UHV-SEM. Figure 4.4a shows CNTs grown from catalyst particles intercalated by the support material. It prevents the aggregation of the catalyst particles into larger clusters due to the high temperatures during the CVD process. But since no diameter selective growth was found for this catalyst, it can be expected that aggregation of individual metal clusters occurs even in the presence of a support material like alumina.
When no support material is used, a small yield of synthesized CNTs could be observed on Si substrates (figure 4.4b), whereas no CNTs were synthesized on Mo substrates (figure 4.4c). Thus, the absence of the support material leads to a significant decrease of the obtained yield due to the missing anchor points provided by it. Therefore, both samples have a very small amount of catalyst particles, which are rather large due to their aggregation during the CVD process. This is shown in figure 4.5, which compares the outer diameter of grown CNTs with the size of their corresponding catalyst particles. The size of the catalyst particles and the outer diameter of the CNTs are obtained by their measured height using AFM in the tapping mode. Figure 4.5 shows a rather large distribution of the size of catalyst particles ranging from 20 nm to 140 nm, while no CNTs can be investigated for catalyst sizes below 30 nm. The resulting diameters of the observed CNTs show no diameter selective growth. Fur-

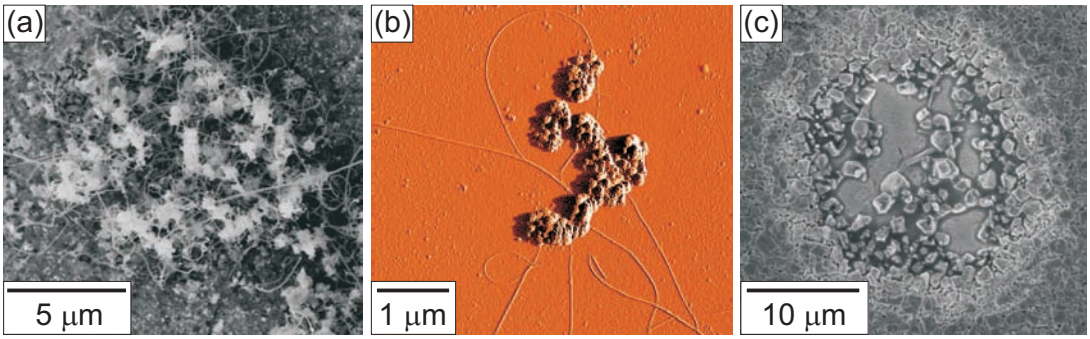

Figure 4.4: (a) UHV-SEM image of CNTs grown away from catalyst particles intercalated by alumina clusters. (b) AFM image of CNTs grown from aggregated nanoclusters without any support material. (c) In this case no CNTs are synthesized on Mo substrates, while large aggregated catalyst particles could be observed by UHV-SEM.

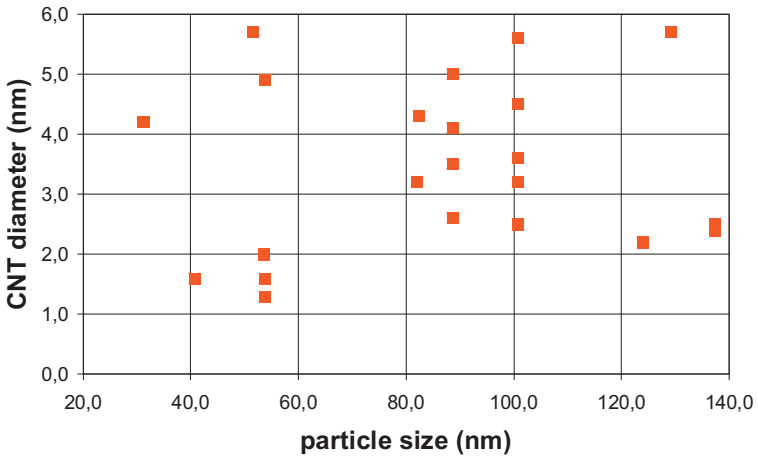

Figure 4.5: Comparison of the outer diameters with the size of catalyst particles for CNTs grown on a Si substrate using Cat 3 without a support material. The outer tube diameters and the particle size are obtained by AFM using the tapping mode.

thermore, the observed large catalyst particles on Mo substrates seem to react with the substrate as shown in figure 4.4b, which may explain the absence of synthesized CNTs. This assumption could be confirmed by the observed reactions between the molecular nanocluster and different substrates after its thermal decomposition, where Si substrates show induced calderas, perforated Si_3N_4 are melted and deposited Pt markers on Si substrates are corroded. Thus, the strong dependence of the reactions of these molecular nanoclusters to the support material used observed by Edgar *et al.* could be confirmed [116].
CNTs investigated in the following chapters are synthesized with a catalyst similar to Cat 2, which is more commonly used for CVD synthesis compared to Cat 3 and Cat 4, allowing better comparison to the results of other researchers [25, 117, 118].

4.5 Influence of the growth temperature

In order to further characterize the pristine material, bulk samples of CNTs were synthesized at different growth temperatures T_{CVD} on quartz glass and investigated with FT-Raman spectroscopy. The laser used for the FT-Raman measurements is fixed to a wavelength of $\lambda = 1064\,\mathrm{nm}$ with no tuning option. This only provides the investigation of CNTs with certain diameters being in resonance. Therefore, bulk samples with a good statistical distribution of CNTs with different diameters were

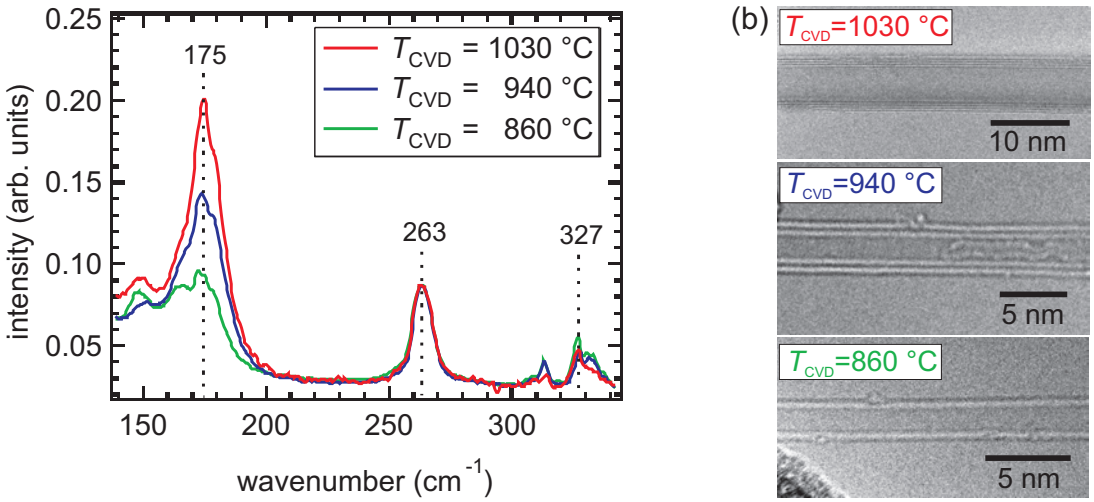

Figure 4.6: (a) RBMs measured by FT-Raman for CNTs synthesized at different growth temperatures. The intensities are normalized to the G-mode. (b) Comparison of the structure of synthesized CNTs at different growth temperatures measured by HRTEM.

investigated, providing statistical information of the CNTs being resonant at the fixed laser excitation. A comparison of the measured Raman spectrum in the range between 140 cm^{-1} and 350 cm^{-1} directly after CVD growth for different growth temperatures T_{CVD} is shown in figure 4.6a. For a direct comparison, the intensities of all spectra are scaled to the intensity of the G-mode. Since the relative intensities of these bulk samples are compared, inter-tube interactions are neglected in the following, which show only little influence on the electronic structure of individual CNTs and therefore on their resonance conditions. The peak located at 263 cm^{-1} is a BBLM, which will be discussed in chapter 6.2.

For higher growth temperatures, a strong increase of the intensity for RBMs around 175 cm^{-1} could be observed compared to the intensity of RBMs around 327 cm^{-1}. According to equation 3.12 these RBMs arise from CNTs with different diameters, while the RBMs around 175 cm^{-1} correspond to smaller diameters compared to the RBMs around 327 cm^{-1}. This may indicate a change of the diameter distribution depending on the growth temperature T_{CVD}.

In order to further support this assumption, individual CNTs were grown on perforated Si_3N_4 membranes to compare the atomic structure of CNTs synthesized at different growth temperatures by using HRTEM. Figure 4.6b shows that at $T_{\mathrm{CVD}} = 1030\,^{\circ}\mathrm{C}$ mostly multi-walled CNTs with more than three layers and a large outer diameter ($d_{\mathrm{T}} > 7$ nm) are forming, while at $T_{\mathrm{CVD}} = 940\,^{\circ}\mathrm{C}$ and $T_{\mathrm{CVD}} = 860\,^{\circ}\mathrm{C}$ nearly all CNTs

are double- or single-walled providing a smaller outer diameter ($d_T < 5$ nm). Thus, we can assume that the relative increase in intensity observed in the FT-Raman spectrum (figure 4.6a) is due to the increasing outer diameters of CNTs, while also the number of layers increases with the growth temperature T_{CVD} [119].
The amorphous material within the DWCNT grown at $T_{CVD} = 940\,℃$ is due to discontinued growth of an inner layer, which could only rarely be investigated. In general, the synthesized CNTs are very clean at their outside showing a small amount of defects and are unfilled. This is in agreement to the small D/G-ratio observed for CNTs grown with this catalyst in figure 4.3b, which slightly increases at higher growth temperatures. On the one hand this can be explained by the formation of amorphous carbon due to an over-supply of carbon atoms caused by the increased decomposition of methane. On the other hand the D/G-ratio may be increased by more defects in the layers within the pristine material synthesized at higher temperatures as investigated by Xiong *et al.*[120].
It should be mentioned here that the structure of the synthesized CNTs is also dependent on their yield. A higher probability for growing MWCNTs with the same recipe was found if a larger amount of catalyst is used, e.g. by skipping the blow-drying step. Also the inner diameter increases with an increase of the yield of CNTs. This may be due to the coalescence of bundled CNTs during the growth process forming larger MWCNTs consisting of more layers, which was investigated by Nikolaev *et al.* [121] and Méténier *et al.* [122] for bundled SWCNTs after high temperature annealing.

4.6 Summary

Different Fe:Mo alloy catalysts were investigated using magnesia and alumina nanoparticles as metal support material, where alumina provides the growth of high quality CNTs. This was confirmed by the low intensity of the D-mode compared to the intensity of the G-mode for Cat 2, Cat 3 and Cat 4. Although the molecular nanoclusters have a defined size, no diameter selective growth could be observed due to the aggregation of catalyst particles even when a metal support material is present. This may be avoided by the usage of smaller support particles, leading to a better separation of the decomposed nanoclusters. The yield of synthesized CNTs depends strongly on the support material used to provide anchor points for the catalyst particles, which aggregate to large clusters or are removed from the substrate without any support material. This shows the importance of the metal support material allowing the growth of CNTs in a high yield on different kinds of substrates, which makes a correlation of different characterization methods possible.
The growth temperature influences the outer diameters of synthesized CNTs and their number of layers, which both increase for higher temperatures. This could also be observed for bulk samples with a high yield of CNTs due to the coalescence of CNTs

during CVD growth. The yield of the CVD growth can be affected by the amount of deposited catalyst particles on the substrate, which can be altered by using different deposition methods. Thus, CNTs can be synthesized by CVD directly on different substrates, where their number of layers, their inner diameter distribution and their yield can be influenced allowing the investigation of individual or bundled CNTs with different numbers of layers.

Chapter 5

Frequency-dependent Raman spectroscopy

The diameter of CNTs is an important parameter for the preparation of peapods, leading to different ordering phases of the encapsulated C_{60} molecules and different interactions between the innermost tube and the C_{60} molecules. No encapsulation of C_{60} is possible when the inner hollow determined by the diameter of the innermost CNT is too small. For transport measurements, on the other hand, the electronic properties of the investigated CNTs are important. As discussed in chapter 2.2 the electronic properties of CNTs depend strongly on their atomic structure, which is defined by the chiral index (n_1, n_2). The determination of their chiral indices is therefore of major importance for the development of CNT-based devices. These parameters can be extracted from HRTEM measurements on individual CNTs, but due to its destructive behavior this has to be done as a final step. The non-destructive determination of these parameters before further experiments would open a way to choose the adequate individual CNT. Therefore, resonant Raman spectroscopy (RRS) being a non-destructive method is employed to assign the diameters of individual tubes within a small bundle and the chiral indices of individual layers within a MWCNT. As discussed in section 3.3.3 the RBM shows a strong resonance behavior. This provides the separation of individual SWCNTs within a bundle or individual layers of a MWCNT by using RRS as discussed in chapter 5.1 and chapter 5.2.

5.1 Diameter Assignment of a separated bundle of CNTs

RRS experiments were performed on CNTs synthesized on a Si substrate at a growth temperature of $T_{\mathrm{CVD}} = 900\,^{\circ}\mathrm{C}$, resulting in mostly SWCNTs with diameters ranging from 1 nm to 5 nm and a length of several micrometers as described in chapter 4. As shown in figure 5.1, the catalyst particles (white arrow) were deposited at selected positions on a Si substrate, allowing the selective observation of individual CNTs or small

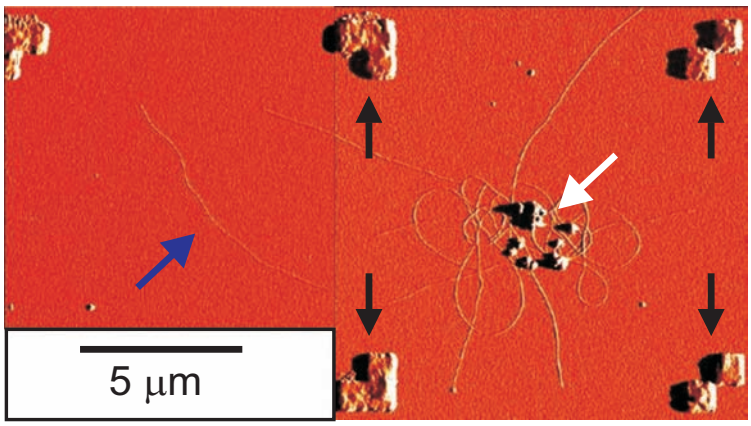

Figure 5.1: AFM image showing the surface of the investigated sample. The catalyst particles appearing as white particles (white arrow) are placed between four markers defining an individual cell on the sample (black arrows). Several SWCNTs are grown away from the catalyst particles, and the position marked by the blue arrow is further investigated by RRS.

bundles. The selective deposition of the catalyst and the pattering of the substrate was done using electron beam lithography. It is seen in figure 5.1 that the catalyst particles are placed in the middle between four markers (black arrows) defining an individual cell. The markers are made from Pt to prevent their melting during CVD growth and have a diameter of 1 µm, being visible with an optical microscope. Thus, each cell can be identified by a unique set of four markers.
The laser power was held below $P = 0.5\,\mathrm{mW}$ to prevent local heating [75] while the laser spot was focused on the tube or bundle marked by the blue arrow in figure 5.1. Its diameter is $2.5 \pm 0.2\,\mathrm{nm}$ as determined by AFM measurements. Thus, it is either an individual CNT or a small bundle of CNTs, which cannot be distinguished using AFM.
Therefore, RRS is used to further investigate this selected area. The Raman spectra of the RBM region obtained at different laser wavelengths are shown in figure 5.2a. The peak observed at a laser wavelength of $\lambda = 496\,\mathrm{nm}$ (red) marked by an asterisk is an artefact due to cosmic particles detected by the CCD leading to spikes in the measured Raman spectra. They can be identified by their very narrow line width below $4\,\mathrm{cm}^{-1}$ and their random position. The frequency of the spectra is calibrated by the observed broad Raman peak of Si at $303\,\mathrm{cm}^{-1}$ originating from the substrate. Two RBMs could be found at the laser wavelengths of $\lambda = 488\,\mathrm{nm}$ (blue line) and $\lambda = 496\,\mathrm{nm}$ (red line) at the position $179\,\mathrm{cm}^{-1}$ and $211\,\mathrm{cm}^{-1}$, respectively.
Figure 5.2b shows the Kataura plot calculated for SWCNTs by nearest neighbor tight-

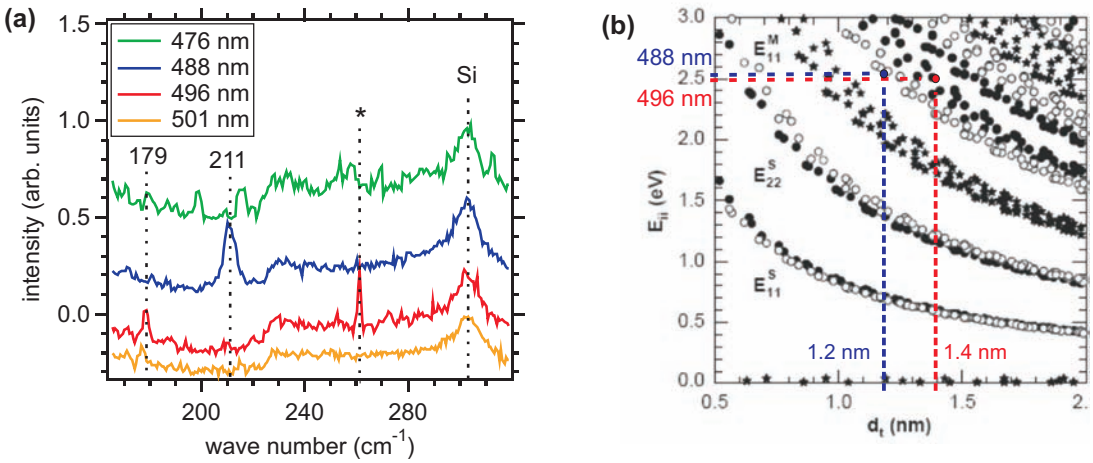

Figure 5.2: (a) Raman spectra of the RBM region measured at different laser wavelengths, which are calibrated by the observed Si peak at 303 cm^{-1}. The sharp peak designed by a asterisk is a spike due to cosmic particles. (b) Kataura plot showing the calculated resonant optical transition energies for semiconducting type I (filled circles), type II (open circles) and metallic SWCNTs (stars). The observed RBMs can be assigned to a type I (blue circle) and a type II SWCNT (red circle) using the Kataura plot taken from [77].

binding simulations according to equation 2.7 with $\gamma_0 = 2.9\,\mathrm{eV}$. A comparison of the calculated diameters according to equation 3.12, using $A = 248\,\mathrm{cm}^{-1}\mathrm{nm}$ for individual CNTs on Si substrates [28] and the laser excitation energy reveals that both SWCNTs are semiconducting, while the RBM at $179\,\mathrm{cm}^{-1}$ arises from a semiconducting type I (filled circles) and the RBM at $211\,\mathrm{cm}^{-1}$ from a semiconducting type II SWCNT (open circles).
This interpretation is consistent with the observed G^+- and G^--mode, which shows no Breit-Wigner-Fano line shape as would be expected for metallic SWCNTs. The measured region of the G-mode is shown in figure 5.3a, where two G^--modes at $1556\,\mathrm{cm}^{-1}$ and $1573\,\mathrm{cm}^{-1}$ and a G^+-mode at $1592\,\mathrm{cm}^{-1}$ can be observed. These frequencies are compared with the experimentally obtained results of Jorio *et al.* for semiconducting (filled circles) and metallic (open circles) individual SWCNTs [123] in figure 5.3b. The observed frequencies plotted as blue and green dashed lines are in good agreement to the results of Jorio *et al.*, where the G^+-mode shows no diameter dependency (black solid line), while the G^--mode shifts in frequency for smaller tube diameters d_T following the dashed black lines calculated by equation 3.16 for semiconducting and metallic tubes respectively. This confirms, in agreement with the two observed RBM

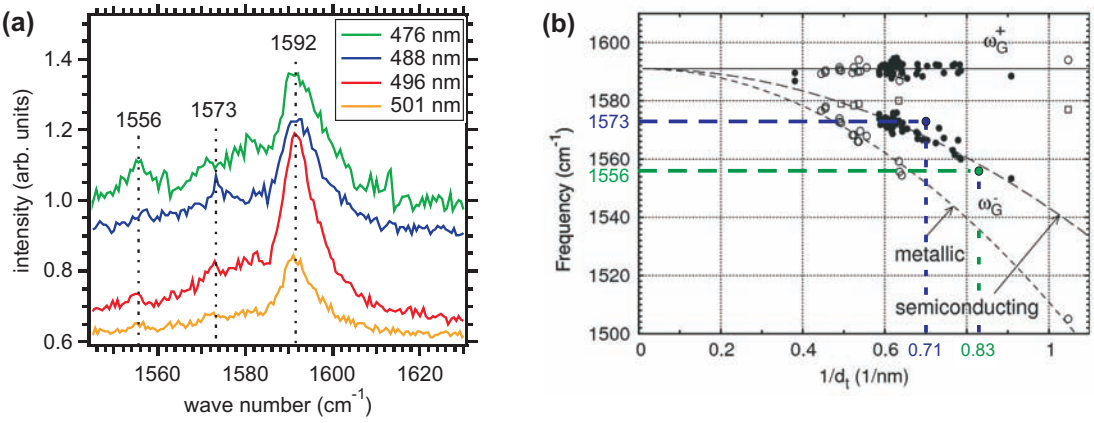

Figure 5.3: (a) Raman spectra of the G-mode at different laser wavelengths showing the splitting of the G-mode due to the diameter dependent curvature effect, where two G^--modes can be found at 1556 cm^{-1} and 1573 cm^{-1}.
(b) Comparison of the measured frequencies of the G^--mode with experimental results obtained by Jorio *et al.* for individual semiconducting (filled circles) and metallic (open circles) SWCNTs [123].

frequencies, the semiconducting nature of both SWCNTs.
Thus, it can be expected that the investigated tube is a small bundle consisting of at least two semiconducting SWCNTs with diameters of about 1.2 nm and 1.4 nm. This is in good agreement to the total diameter of 2.5 nm to 2.9 nm determined by AFM measurements. Small deviations from the expected theoretical values may be due to the bundling effect of both SWCNTs and interactions with the substrate, leading to shifts of the investigated RBM frequency.
The Ar-Kr-laser used in the previous measurements only provides characteristic laser lines having a quite large separation compared to the width of an RBM resonance profile shown below, which prevents a measurement of this sharp resonance for the investigated RBMs. Thus, the accuracy in the value of the resonant transition energies is determined by the width of the resonance window of the measured RBMs, which can be additionally broadened in bundles as will be shown below, which may lead to a deviation of the laser energy used and the real optical transition energy E_{ii} in the order of $\Delta E = 120$ meV. This prevents the assignment of the chiral indices in the Kataura plot for the individual SWCNTs within the bundle, but provides the determination of their electronic properties given by their family index ν, which can be obtained by the frequency of the RBM and the laser energy used or the frequency and shape of the G^--mode.

5.2 Chirality Assignment

CNTs are synthesized directly on a perforated Si_3Ni_4 membrane at a growth temperature of $T_{CVD} = 1030\,℃$, providing mostly MWCNTs as described in chapter 4.5. Because only small amounts of catalyst were deposited on the sample, the yield of CNTs is rather small, which permits individual CNTs to bridge the holes without forming bundles. After CVD the sample was annealed at 900 ℃ in a UHV-chamber for 1.5 hours to clean the outer layers of amorphous carbon and remove small defects, stabilizing the MWCNTs during HRTEM measurements.
To be able to correlate Raman spectroscopy and HRTEM measurements on the same MWCNT, a marker is written with a focused ion beam (FIB) prior to the CVD synthesis. These markers define a coordinate system needed to locate each hole as shown in figure 5.4. UHV-SEM was used to characterize each region before the Raman measurements determining the number of MWCNTs crossing the holes. The position E1 features an individual MWCNT that bridges the hole, as shown in the inset of figure 5.4. This geometry allows a selective investigation of a single MWCNT without any disturbance by adjacent tubes or the substrate. Thus, we can exclude bundling and tube-substrate interactions.
Since Raman spectroscopy only provides indirect information about the atomic structure of CNTs, a correlation with microscopic methods is needed to interpret the observed low-frequency Raman spectra. Figure 5.5a shows a HRTEM image of the

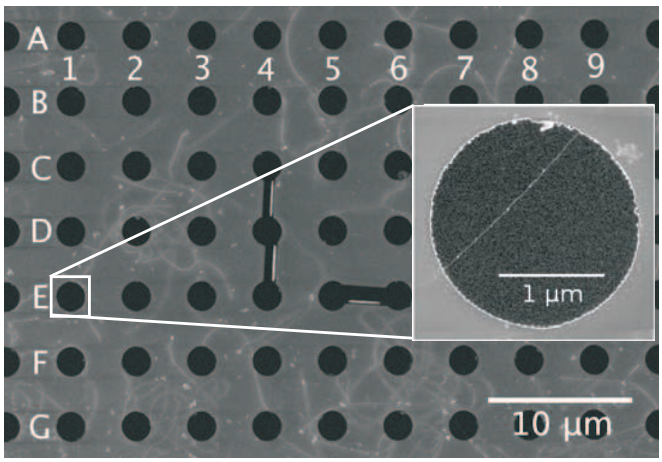

Figure 5.4: SEM picture of the used Si_3N_4 grid customized by a marker written with FIB in the middle of the picture. A coordinate system was defined around and the position E1, further investigated, providing a single MWCNT crossing the hole as shown in the inset.

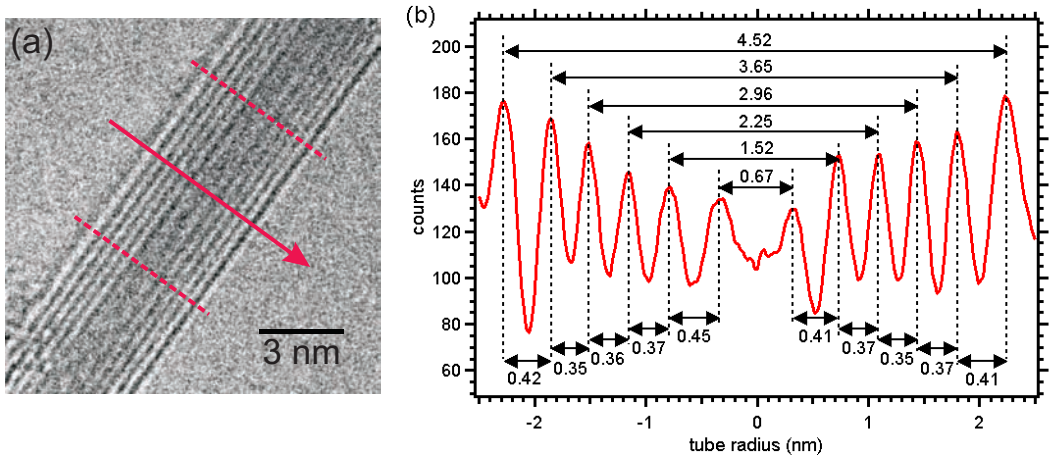

Figure 5.5: (a) HRTEM at 80 keV of the MWCNT crossing the hole at the position E1. (b) Linescan between the red dashed lines and along the red arrow in (a) showing the diameters of the individual tubes above and the wall to wall distances below. All values are given in nm.

MWCNT at position E1 taken after the Raman measurements, which exhibits clean outer layers and a high degree of graphitization of the CNT. For the estimation of the diameters, a line scan between the dashed red lines along the red arrow in figure 5.5a was averaged over 200 px, which is shown in figure 5.5b. The atoms in the HRTEM image appear white, because we measured in slight over-focus to achieve a better contrast. Therefore, the distances between the corresponding maxima on both sides of the symmetric line scan correspond to the individual tube diameters, while the distances between adjacent maxima are the inter-layer separations.
It is clearly seen that this MWCNT consists of six tubes ranging in diameter from 0.67 nm to 4.52 nm. Table 5.1 lists the measured inter-layer separation d_Δ, which is obtained by the average of the two corresponding inter-layer distances, and the full width at half maximum (FWHM) for each diameter d_T in figure 5.5b. The inter-layer distances are between 0.35 nm and 0.37 nm, which agrees within the error of the measurement, featuring a spatial resolution of 0.08 nm as given in section 3.3.1. According to Dresselhaus *et al.* the inter-layer distance is almost equal within MWCNTs ranging from 0.34 nm to 0.39 nm [33], which is consistent with the values observed here. Only the innermost and the outermost tubes have a slightly larger inter-layer separation of $0.41 - 0.45$ nm and the FWHM of their peaks listed in table 5.1 is broadened compared to the FWHM of the other peaks. This difference could be explained by defects induced due to electron irradiation, which induce an off-peeling of those tubes which are only partly stabilized within the layer structure [124]. Due to its larger curvature especially the inner layer is decomposing during HRTEM measurements, indicated by

d_T [nm]	d_Δ [nm]	FWHM [nm]
0.67 ± 0.08 (0.82)	0.43 ± 0.08	0.27
1.52 ± 0.08	0.37 ± 0.08	0.14
2.25 ± 0.08	0.36 ± 0.08	0.16
2.96 ± 0.08	0.36 ± 0.08	0.17
3.65 ± 0.08	0.42 ± 0.08	0.16
4.52 ± 0.08 (4.35)		0.32

Table 5.1: Comparison of the measured inter-layer separation d_Δ and the FWHM for each measured diameter d_T. The corrected diameters of the innermost and outermost layers being damaged during electron irradiation are given in brackets.

its buckling in figure 5.5a, resulting in the broadened FWHM in table 5.1. Since the resonant confocal Raman measurements were done before the HRTEM measurements, an inter-layer separation of 0.35 nm is assumed for the innermost and outermost layer leading to corrected diameters of 4.35 nm and 0.82 nm for the outermost and the innermost tube respectively, given in brackets in table 5.1.
In this chapter, RRS is used to directly assign the chiral indices of individual layers within the investigated MWCNT at the position E1. Especially for larger tube diameters and higher excitation energies, the separation of individual family branches decreases, which requires the resonant transition energy to be determined with a high accuracy. As discussed in chapter 2.6, the electronic structure of individual layers within a MWCNT remains nearly unchanged compared to individual SWCNTs. Only a slight decrease of the resonant transition energy is expected due to the increased curvature effect of the encapsulated layers. Thus, the resonant transition energy can be obtained by resonance profiles of individual BLMs, which are expected for MWCNTs and will be further discussed in chapter 6. Since the RBMs of individual SWCNTs show a very sharp resonance window of only 8 meV [81], a dye laser was used, allowing one to tune the excitation wavelength in small steps of $1 - 2$ nm.
The obtained spectra are shown in figure 5.6a for different laser wavelengths λ, where the measured two BLMs at $131\,\mathrm{cm}^{-1}$ (red) and $161\,\mathrm{cm}^{-1}$ (blue) show a strong resonance effect and were not observed at smaller or larger laser wavelengths. The spectra were calibrated with a neon lamp and normalized in intensity by the non-resonant signal of a CaF_2 crystal. Their measured intensities are shown in figure 5.6b. The obtained resonance profiles are approximated with equation 3.11, which provides the determination of their widths and their resonant transition energies E_{ii}.
For comparison, the resonance profile of a BLM at $210\,\mathrm{cm}^{-1}$ obtained from a small bundle on the same sample, is shown (green squares). This bundle, located at the position G7 in figure 5.4, is shown in figure 5.7a and consists of approximately 4-5

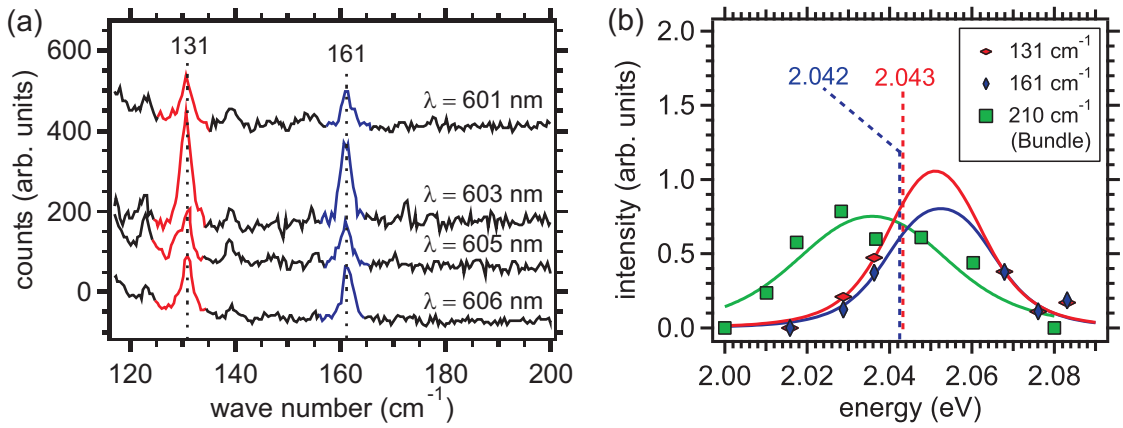

Figure 5.6: (a) Raman spectra of the observed two BLMs at 131 cm^{-1} (red) and 161 cm^{-1} (blue) of an individual MWCNT excited by different laser wavelengths λ. (b) Resonance profiles of these BLMs, which are normalized in intensity by a non-resonant CaF_2 crystal. Obtained resonance profiles are plotted by red and blue markers respectively and compared with the resonance profile of a BLM at 210 cm^{-1} originating from a small bundle (green squares), while the corresponding curve fits are shown as solid lines of the same color.

MWCNTs, which cannot be separated due to their two-dimensional projection prohibiting the determination of their diameters and their number of layers. Figure 5.7b shows the frequency dependent RRS measurements of the BLM located at 210 cm^{-1} originating from the bundle at the position G7 for different laser wavelengths.
The resonance widths of the individual MWCNTs are with 32 meV and 30 meV for the BLMs at 131 cm^{-1} and 161 cm^{-1}, respectively, larger than the resonance width of 8 meV for individual SWCNTs. In contrast, the resonance profile of the BLM at 210 cm^{-1} obtained from the small bundle has a width of 60 meV, which is almost twice the width measured for individual BLMs, but smaller than the resonance width of 120 meV for bundled SWCNTs observed by Fantini *et al.* [75]. Since its BLM is located at 210 cm^{-1}, it can be expected that it arises from an inner layer with a small diameter $d_T \leq 1$ nm, which should not be affected by the tube-tube interactions in bundles. Instead it is more reasonable that the observed broadening of the resonance profile is due to a superposition of two BLMs originating from two different inner tubes in the bundle with similar diameters and transition energies. This explains the deviation of the measured width of the resonance profile compared to the results of Fantini *et al.*, which show that the width of the resonance profile indicates whether the measured mode originates from a SWCNT, a MWCNT or an outermost layer in a bundle.

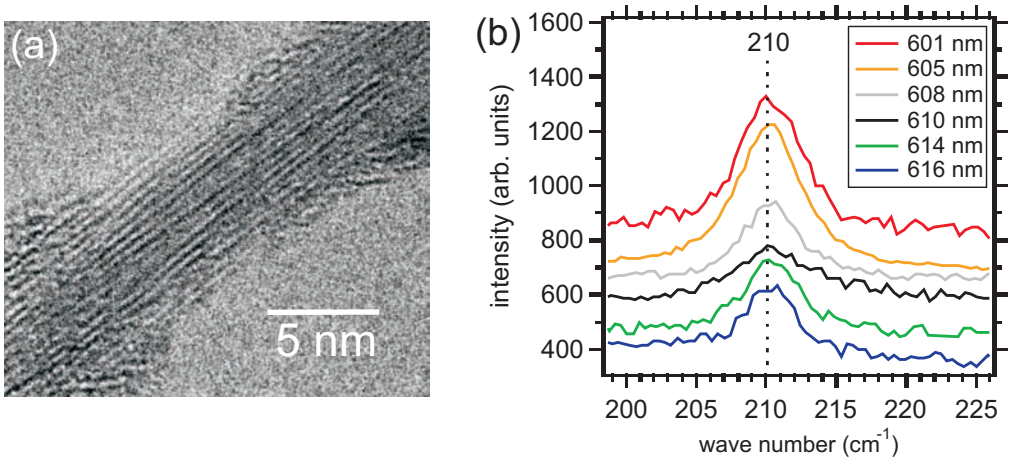

Figure 5.7: (a) HRTEM image of an individual bundle located at the position G7 in figure 5.5. (b) RRS of a BLM located at 210 cm^{-1} obtained from the position G7 using different laser wavelengths.

The second important parameter which can be derived from the approximation of equation 3.11 to the measured intensities is the resonant transition energy E_{ii}. It is located near the maximum of the measured resonance profiles at 2.043 eV and 2.042 eV for the measured BLMs at 131 cm^{-1} and 161 cm^{-1}, respectively, as shown by the dashed vertical lines in figure 5.6b. These resonant transition energies and the corresponding tube diameters obtained by HRTEM, as shown in figure 5.5, are compared with the Kataura plot in figure 5.8, calculated by Maruyama *et al.* using the nearest neighbor tight-binding approximation according to equation 2.7 with $\gamma_0 = 2.9\,eV$ [125]. Calculated transition energies are plotted by green dots, while the experimentally obtained transition energies are colored in red and blue for the measured BLM at 131 cm^{-1} and 161 cm^{-1}, respectively. It shows that the resonant energy of the BLM at 131 cm^{-1} can be assigned to the branch with $\beta = 57$ of the E_{22}^M transition featuring a family index of $\nu = 0$, while the resonant energy of the BLM at 161 cm^{-1} originates from the E_{33}^S transition with $\nu = +1$ and $\beta = 38$. The chiral indices of the most likely assignments within the assumed error of the tube diameter obtained by HRTEM of 80 pm are colored corresponding to the two investigated BLMs.
As mentioned before, we expect a small decrease of the optical transition energies of the observed layers being encapsulated within the MWCNT. Thus, it is most likely that the BLM at 131 cm^{-1} originates from either a (19,0) or a (18,2) SWCNT, while the BLM at 162 cm^{-1} originates either from a (28,1) or a (27,3) SWCNT. These SWCNT are located at the end of each branch showing a transition energy that is for the (18,2) and the (27,3) approximately 9 meV and for the (19,0) and (28,1) SWCNT 13 meV higher than the measured transition energies of both BLMs. Since the inter-

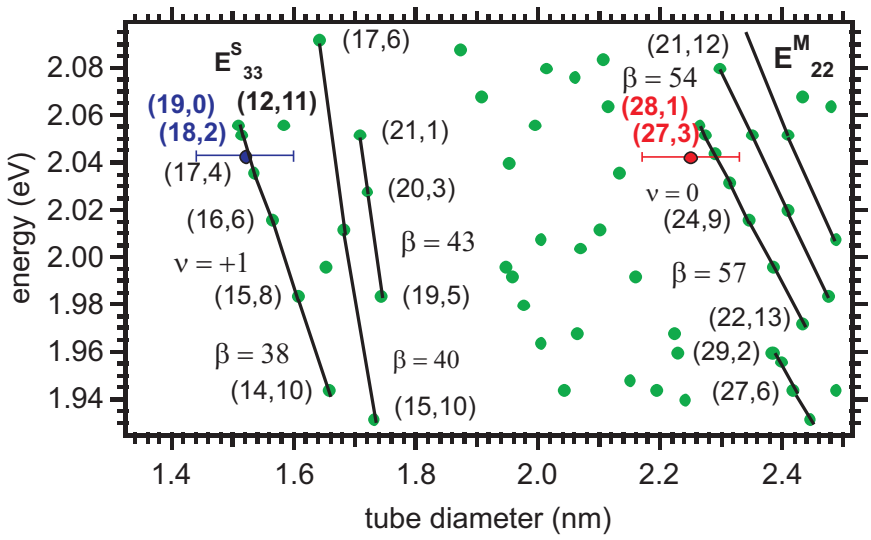

Figure 5.8: Comparison of the measured diameters obtained by HRTEM and resonant transition energies obtained by RSS for the investigated BLMs at 131 cm^{-1} (red point) and 161 cm^{-1} (blue point) with the resonant transition energies calculated by Maruyama *et al.* [125] (green points). The chirality indices are given in brackets, while family branches with the same branch index β are connected by black lines.

layer interactions strongly depend on the chirality index of the interacting layers, these values can be compared to the inter-layer interaction energy of around 10 meV for a (7,0)@(16,0) DWCNT calculated by Denis *et al.* with density functional calculations [126], which would nicely fit to the transition energies of the (18,2) and (27,3) SWCNT in figure 5.8. Furthermore, Okada *et al.* predicted an overlap between the conduction band of the inner layer and the valence band of the outer layer leading to a metallization of the (7,0)@(16,0) DWCNT [32].
This shows that besides the determination of the family index ν, which defines the electronic properties of individual tubes, RRS provides the determination of the branch index β of the investigated layers when the transition energy is obtained by resonance profiles of individual BLMs. This makes it possible to distinguish between metallic and semiconducting SWCNTs but also between metallic and semimetallic SWCNTs, which is important for electronic devices.

5.3 Summary

In this chapter we demonstrated that RRS allows one to selectively investigate individual SWCNTs even within a MWCNT or a rope. It allows one not only to determine the diameter by the $1/d_{\mathrm{T}}$-dependence in the case of SWCNTs, but also to assign the investigated SWCNTs to its family, allowing the determination of its electrical behavior. A correlation of HRTEM and RRS allow the determination of the diameters of each tube with high accuracy, as shown for an individual MWCNT. Furthermore, the resonant transition energy can be determined with high accuracy by the resonance profiles of the measured SWCNTs. This allows for the determination of the branch of the investigated SWCNT by a direct assignment of the chirality index using the theoretical Kataura plot, while the width of the resonance profile indicates whether the SWCNT is individual, within a MWCNT or a bundle.
Since Raman spectroscopy is, in contrast to TEM, a non-destructive characterization method, it offers the possibility to characterize individual SWCNTs with different environments prior to further experiments, allowing one to determine their atomic and electronic structure. This is essential for the filling of the CNTs with C_{60} or quantum transport measurements on individual CNTs.

Chapter 6

Phonon coupling in carbon nanotubes

As discussed in section 3.3.3, an interaction is expected between individual layers within a MWCNT, inducing coupled phonon states of the RBMs called BLMs. This was predicted by Popov *et al.* [84] and Rahmani *et al.* [85] by numerical simulations. To study the effect of the phonon coupling for MWCNTs, a correlation between HRTEM and confocal Raman spectroscopy for an individual MWCNT is presented in chapter 6.1.
According to calculations by Rahmani *et al.*, a coupled phonon mode is also expected for large bundles of CNTs named BBLM, which arises from the outermost layers of CNTs in a bundle. This will be investigated for a bulk sample providing large bundles of CNTs in chapter 6.2.

6.1 Phonon modes of an individual MWCNT

In the previous chapter, an individual MWCNT was introduced in figure 5.4 and characterized in figure 5.5, which will be used to study the BLMs of MWCNTs. Because it is grown separately over a hole, substrate interactions and bundling effects, which additionally influence the frequency of the radial modes, can be neglected. Using confocal resonant Raman spectroscopy, sharp peaks with a line width of $3 - 4\,\mathrm{cm}^{-1}$ are measured at the laser wavelength of $\lambda = 603\,\mathrm{nm}$ (blue) and $\lambda = 647\,\mathrm{nm}$ (red) as shown in figure 6.1. These peaks, which are located at $131\,\mathrm{cm}^{-1}$, $161\,\mathrm{cm}^{-1}$ and $270\,\mathrm{cm}^{-1}$ have a strong resonance effect, as shown before. Due to this strong resonance behavior which is characteristic for the RBM, and their comparable line widths, we can assume that these peaks are BLMs of the investigated individual MWCNT. Other BLMs of smaller frequency could not be discerned due to the relatively broad Rayleigh peak which prohibits the investigation of weak modes near the Rayleigh frequency.

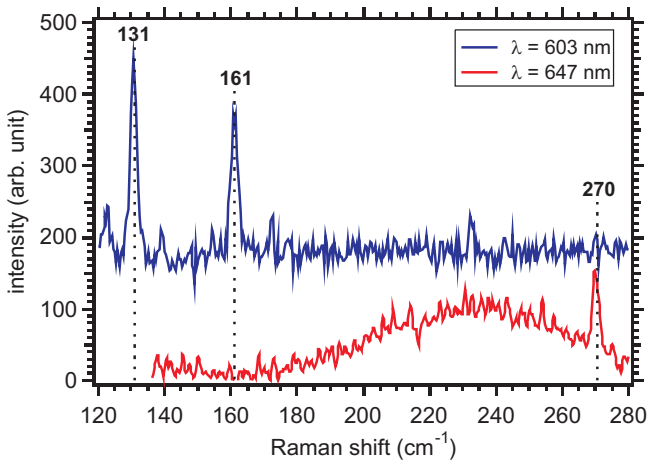

Figure 6.1: Resonant Raman spectrum of the individual MWCNT crossing the hole at position E1 for laser wavelengths of $\lambda = 603\,\mathrm{nm}$ (blue) and $\lambda = 647\,\mathrm{nm}$ (red).

6.1.1 Numeric model of phonon coupling in MWCNTs

When the curvature effect and the inter-layer coupling are neglected, each tube within the MWCNT should behave like an individual SWCNT, where each RBM frequency can be calculated by equation 3.12 with $A = 223.75\,\mathrm{cm}^{-1}\mathrm{nm}$ for SWCNTs [16] due to the absence of tube-substrate interactions using the measured diameters d_T. The inter-layer coupling between different layers in a MWCNT leads to non-linear up-shifts of the BLM frequencies compared to the RBM frequencies of the uncoupled SWCNTs, as will be shown in the following.

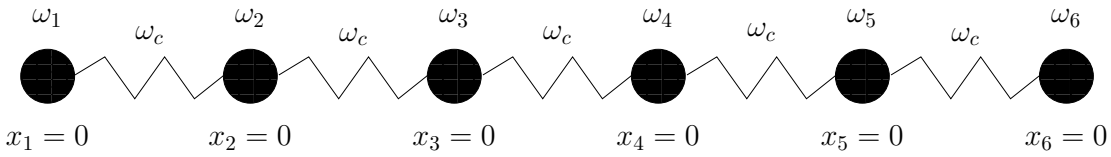

Figure 6.2: One-dimensional model of the inter-layer vdW interactions in the radial direction based on a chain of six harmonic oscillators with eigenfrequencies ω_n being coupled by an equal coupling frequency ω_c. All amplitudes x_n are set to 1.

To further study the effect of inter-layer coupling a simple numeric model is constructed to describe the inter-layer coupling in the radial direction by a one-dimensional chain

of coupled harmonic oscillators, as shown in figure 6.2. The mass m_n and the spring constant k_n of each oscillator is expressed by its eigenfrequency

$$\omega_n = \sqrt{\frac{k_n}{m_n}}, \tag{6.1}$$

which is given by the RBM frequency ω_{RBM} for the individual layers. This eigenfrequency ω_n is coupled to the eigenfrequencies of the adjacent layers ω_{n+1} and ω_{n-1} by the coupling frequency ω_c. Assuming an equal coupling frequency of ω_c for different layers neglecting the curvature and the surface of individual CNTs, the equations of motion for N coupled harmonic oscillators are given by

$$\ddot{x}_n = -\omega_n^2 x_n - \omega_c^2(x_n - x_{n+1}) - \omega_c^2(x_n - x_{n-1}), \tag{6.2}$$

with $n = 1, \ldots, N$ and the boundary conditions

$$x_0 = x_{N+1} = 0. \tag{6.3}$$

The investigated MWCNT at the position E1 has six layers (see figure 5.5) leading to $N = 6$, which results in six coupled equations of motion. These are integrated in time and Fourier transformed to obtain the resulting frequencies for each harmonic oscillator with their amplitudes set to $x_n = 1$.
The coupling frequency ω_c is linearly increased in the calculation as shown in figure 6.3a, leading to an increase of all BLM frequencies compared to their RBM frequencies with $\omega_c = 0$ calculated from their diameters observed by HRTEM. The dashed white lines in figure 6.3a mark the frequencies of the measured BLMs in the low-frequency Raman spectrum as shown in figure 6.1. This allows for the assignment of the three observed BLMs to the three innermost layers within the MWCNTs.
Compared to the BLM frequencies measured by Raman spectroscopy, the calculated frequencies of the two innermost layers are up-shifted, while the calculated frequency of the third layer is down-shifted.
According to calculations for MWCNTs by Popov *et al.* the lowest BLM frequency is an in-phase mode, the highest BLM frequency a counter-phase mode and the intermediate modes are of mixed character [84]. The effect of the inter-layer coupling is strongest for the intermediate modes compared to the in-phase and counter-phase mode, which is in agreement to the results of Benoit *et al.* [127].
The dashed black line in figure 6.3a marks the coupling frequency $\omega_c = 1.52\,\mathrm{THz}$, which results in the best agreement between calculation and experiment.
This calculation already fits quite well to the measured BLM frequencies, but it does not include the surface effect, which describes the increasing number of interacting atoms for increasing diameters. After equation 6.1, the assumed coupling frequency ω_c depends not only on the coupling constant k_c, but also on the difference of the

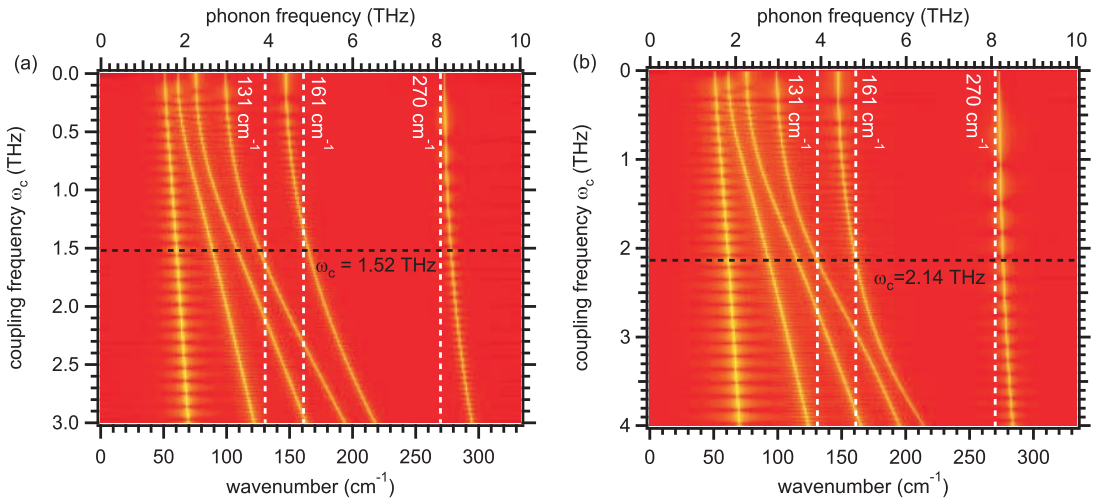

Figure 6.3: BLM frequencies (yellow lines) for increasing coupling frequency ω_c assuming (a) an equal coupling frequency for all layers (Sim1) and (b) a coupling frequency scaled with the diameter respecting the surface effect (Sim2). The dashed white lines show the positions of the measured Raman modes with its frequencies, which allow for the assignment of the measured BLM frequencies to the three innermost tubes. The best agreement is found for a coupling frequency of (a) 1.52 THz and (b) 2.14 THz marked by the black dashed lines.

masses between two adjacent layers $m_{n+1} - m_n$. The mass of individual layers in our one-dimensional model is given by the number of C atoms on the layer surface. When an equal distance is assumed for the C atoms, this is proportional to the diameter of each layer, while the mass difference for two adjacent layers decreases for larger diameters. Thus, the inter-layer coupling is expected to increase for larger diameters, which can be described by a scaled coupling frequency

$$\omega_s = \sqrt{1 - \frac{d_{n+1}[\mathrm{nm}] - d_n[\mathrm{nm}]}{d_{n+1}[\mathrm{nm}]}}\omega_c \tag{6.4}$$

between the n-th and $(n+1)$-th layer with their diameters d_n and d_{n+1} tending to $\omega_s = \omega_c$ for graphite with infinite diameters. Figure 6.3b shows the resulting calculation of the BLM frequencies when assuming a scaled coupling frequency according to equation 6.4, which show far better agreement to the experimental values than the prior model neglecting the surface effect. In this case, the best agreement between simulated and measured frequencies is found at a coupling frequency of $\omega_c = 2.14\,\mathrm{THz}$ as marked by the black dashed line in figure 6.3b. To be able to distinguish between

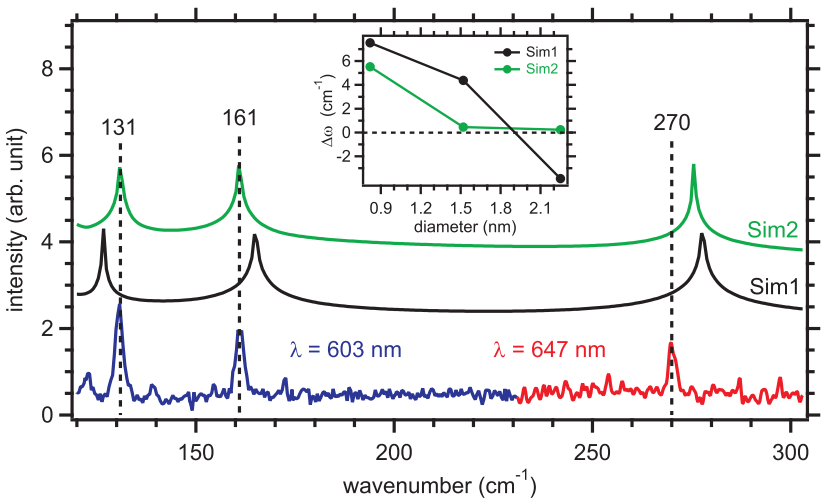

Figure 6.4: Comparison of the measured (blue and red) and calculated Raman spectra assuming an equal coupling frequency for all layers denoted as Sim1 (black) and a coupling frequency respecting the surface effect denoted as Sim2 (green). The inset shows the absolute deviation $\Delta\omega$ of the calculated spectra from the measured values for the three innermost diameters.

theses two models, the previous model, assuming an equal coupling frequency for all layers, is denoted as Sim1 and the latter model, assuming a scaled coupling frequency according to equation 6.4, as Sim2 respectively.
In figure 6.4 the experimentally obtained spectra measured at a laser wavelength of $\lambda = 603\,\mathrm{nm}$ (blue) and $\lambda = 647\,\mathrm{nm}$ (red) are compared with the calculated spectra for Sim1 (black) and Sim2 (green). When assuming an equal inter-layer frequency (Sim1), the calculated mode frequencies are down-shifted for the lower frequency mode at $131\,\mathrm{cm}^{-1}$, while they are upshifted for the higher frequency modes at $161\,\mathrm{cm}^{-1}$ and $270\,\mathrm{cm}^{-1}$. This is shown in more detail in the inset of figure 6.4, which compares the difference of the measured and the simulated Raman modes $\Delta\omega = \omega_{\mathrm{Sim}} - \omega_{\mathrm{Raman}}$ for the three innermost diameters. The deviation for Sim1 is decreasing with the tube diameter. This can be explained by the surface effect leading to a non-equal coupling frequency decreasing for smaller diameters due to the decreasing number of interacting C atoms. When this effect is taken into account in the calculation (Sim2), a far better consistence of the simulated frequencies to the experimentally measured frequencies can be obtained. As shown in the inset, the absolute deviation obtained for Sim2, which takes the surface effect into account, is rapidly decreasing to zero for larger diameters (marked by the dashed black line). Thus, it can be expected that the strong down-shift of the frequency of the BLM of the innermost tube with a diameter of only

d_T [nm]	$\omega_{Raman}[cm^{-1}]$	$\omega_{RBM}[cm^{-1}]$	ω_{Sim1} [nm]	ω_{Sim2} [cm^{-1}]
0.82	270	272.87 (1.1%)	277.53 (2.8%)	275.52 (2.0%)
1.52	161	147.20 (8.6%)	165.45 (2.6%)	160.78 (0.1%)
2.25	131	99.44 (23.9%)	126.75 (3.0%)	130.76 (0.2%)
2.96		75.59	108.74	115.41
3.65		61.30	89.40	93.40
4.35		51.44	60.71	61.38

Table 6.1: Comparison of the experimentally obtained BLM frequencies ω_{Raman} and calculated frequencies obtained by equation 3.12 (ω_{RBM}), equation 6.2 assuming equal coupling (ω_{Sim1}) and a scaled coupling frequency (ω_{Sim2}) using equation 6.4 respecting the surface effect for each measured diameter d_T. Deviation percentage from the experimentally obtained frequencies ω_{Raman} are given in brackets.

0.82 nm is due to the curvature effect, which is negligible for the second and the third innermost tube with a diameter of 1.52 nm and 2.25 nm. Instead these BLMs show an up-shift compared to the calculated RBMs for individual SWCNTs, which are caused by the inter-layer phonon coupling.
A comparison of the observed and calculated BLM modes is given in table 6.1. The relative deviations of each calculated frequency from the observed Raman frequency ω_{Raman} are listed in brackets. The frequencies ω_{RBM} are calculated according to equation 3.12 by using the corrected tube diameters d_T neglecting the vdW coupling. While the percentage deviation is only 1.1% for the innermost counter-phase mode, it increases rapidly for the intermediate Raman modes. This is in agreement with the results observed by Zhao *et al.*, who observed an up-shift of only ∼5% for innermost layers within MWCNTs [128]. When taking the vdW coupling into account and assuming an equal coupling frequency for all layers (Sim1), the calculated BLM frequencies ω_{Sim1} show a constant relative deviation of about 3% for the three innermost SWCNTs. After considering a coupling frequency that take the surface effect into account according to equation 6.4 (Sim2), the relative deviation of the resulting frequencies ω_{Sim2} could be further reduced. But there is still a relative deviation of 2% between the observed and the calculated BLM frequency of the innermost tube, which is rapidly decreasing for tubes with larger diameters and can be explained by the curvature effect as described in chapter 2.4.
As discussed in section 3.3.3 Popov *et al.* showed that the counter-phase mode tends towards the counter-phase B_{2g}-mode of graphite with a frequency of 3.81 THz [129] for large diameters and increasing number of layers, while the in-phase mode is disappearing for pure graphite. He *et al.* calculated that the vdW interaction in a multi-layered graphene sheet causes resonant vibrations with frequencies in the terahertz range that

increase for increasing numbers of layers approaching the B_{2g}-mode of graphite [130]. Thus, we can expect that the coupling frequency ω_c also increases with the number of layers and larger diameters, becoming the B_{2g}-mode of graphite for infinity diameters and increasing number of layers, which is optically silent and therefore does not show up in Raman spectroscopy [131]. The best agreement between the measured and simulated frequencies is obtained for a coupling frequency of $\omega_c = 1.52\,\mathrm{THz}$ for Sim1 and $\omega_c = 2.14\,\mathrm{THz}$ for Sim2, shown by the black dashed lines in figure 6.3. While the obtained coupling frequency for Sim1 is averaged over all contributing tubes due to the assumed equal phonon coupling, the coupling frequency obtained for Sim2 compensates the surface effect, resulting in a frequency, which is closer to the expected frequency of the B_{2g}-mode in graphite. This shows that the simple one-dimensional model (Sim1) can be improved by respecting the surface effect (Sim2) leading to a coupling frequency decreasing for smaller diameters.

6.2 Phonon modes in nanotubes bundles

As mentioned in section 3.3.3 phonon coupling can also be observed for bundles of CNTs where the outermost layer of each CNTs is coupled to its neighbors by inter-tube vdW interactions. For this case Rahmani *et al.* predicted an additional BBLM mode for larger bundles [85].
To investigate this coupled phonon mode, a bulk sample is measured with FT-Raman using a Bruker RAM II spectrometer at a laser wavelength of $\lambda = 1064$ nm. A high amount of catalyst was placed on a Mo sample by using a heating plate before the CNTs are synthesized by CVD at a growth temperature of $T_{\mathrm{CVD}} = 900\,^{\circ}\mathrm{C}$. Thus, large bundles of mainly SWCNTs and DWCNTs are expected to form due to their inter-tube vdW interactions according to chapter 4.5.
Several peaks can be observed within the RBM region of the measured Raman spectra shown in figure 6.5a. The expected diameters of the SWCNTs inducing these modes can be determined by the $1/d_{\mathrm{T}}$-dependence of their resonance frequency using equation 3.12 with $A = 223.75\,\mathrm{cm^{-1}nm}$ for SWCNTs [16]. This makes an assignment of the used excitation energy of 1.167 eV (black dashed line) and the calculated diameters (colored dashed lines) to the resonant energy transitions in the Kataura-Plot possible, as shown in figure 6.5b. It shows that the peaks observed at $148\,\mathrm{cm^{-1}}$ (red) and $165\,\mathrm{cm^{-1}}$ (green) arise from the E_{22}^S transition and the peaks at $313\,\mathrm{cm^{-1}}$ (olive) and $326\,\mathrm{cm^{-1}}$ (purple) from the E_{11}^S transition. Because no frequency shift due to inter-layer coupling can be observed, we attribute these peaks to RBMs of SWCNTs. Only the strong peak at $263\,\mathrm{cm^{-1}}$ (blue) could not be assigned, because its calculated diameter of $d_{\mathrm{T}} = 0.85\,\mathrm{nm}$ leads to a resonance point between the resonance branches (blue cross). Since the investigated CNTs are mostly SWCNTs and DWCNTs only small deviations from the $1/d_{\mathrm{T}}$-dependency due to the inter-layer coupling are ex-

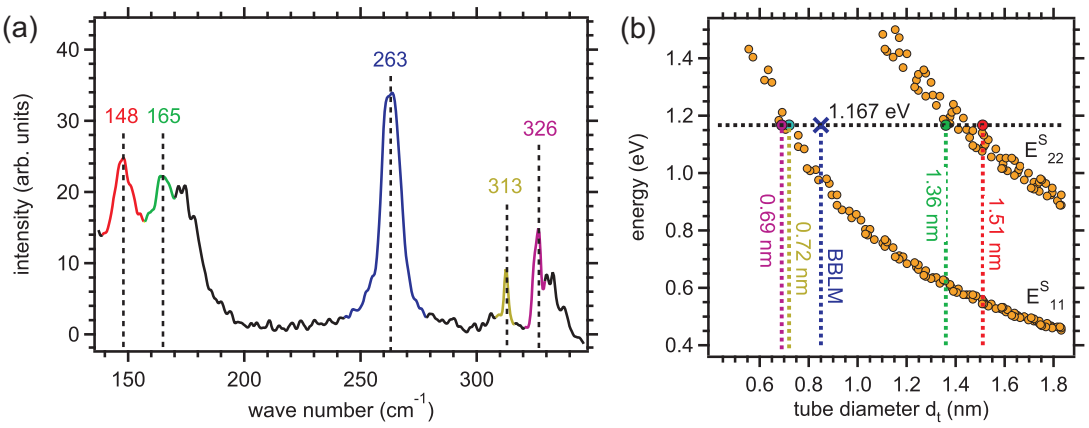

Figure 6.5: (a) FT-Raman spectra measured at a laser wavelength of $\lambda = 1064\,\text{nm}$ showing several peaks (colored) in the RBM region of a bulk sample providing a high yield of CNTs. (b) Besides the BBLM at $263\,\text{cm}^{-1}$ (blue cross) these modes can be assigned to their resonant transitions by the Kataura plot (marked by their colors) at the laser excitation energy of 1.167 eV (black dashed line), which identifies it as a coupled phonon mode. The calculated Kataura plot was provided by S. Maruyama [125].

pected. Thus, we can exclude that the observed peak at $260\,\text{cm}^{-1}$ is a BLM. Because this peak showed up for different kinds of substrates and decreased with the yield of the CNTs, we propose that this peak is the predicted BBLM.
In order to be able to observe a BBLM, which arises from the RBMs of the outermost layers of CNTs in a bundle, the contributing CNTs need to be in resonance. The outermost diameter of the CNTs contributing to the BBLM can be calculated according to equation 3.15, which results in an outer diameter of $d_{\text{outer}} = 1.53\,\text{nm}$. This is consistent with the diameter calculated for the RBM at $148\,\text{cm}^{-1}$, which is in resonance at 1.167 eV and can therefore contribute to the BBLM.
To further investigate the observed mode at $263\,\text{cm}^{-1}$, the sample is heated in air at 400 °C for 25 minutes, at 450 °C for 5 minutes and at 500 °C for 5 minutes consecutively. The obtained spectra, which are normalized to the peak height of the G-mode, are shown in figure 6.6a, where the observed RBMs and the BBLM are colored as before. Besides the RBM at $165\,\text{cm}^{-1}$ (green), which could not be fitted due to its broadened line shape in the pristine sample, figure 6.6b plots the relative intensities for each mode normalized to the intensity of the D*-mode. During the heating at 400 °C for 25 minutes no change of the intensities could be observed. After increasing the heating temperature to 450 °C the intensity of the BBLM at $263\,\text{cm}^{-1}$ is rapidly reduced, while the intensities of the RBM at $148\,\text{cm}^{-1}$ (red) belonging to larger diameters slightly

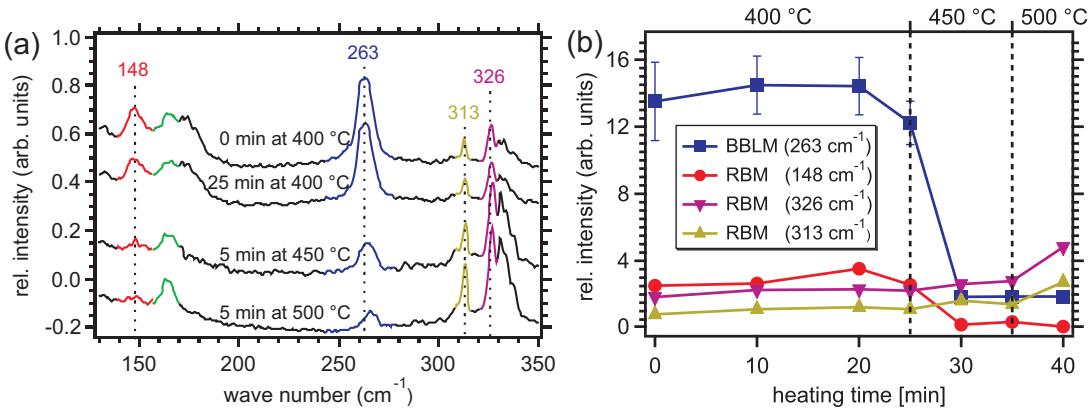

Figure 6.6: (a) Change of the intensity of the RBMs (colored) and the BBLM (blue) after heating in air at 400 °C, 450 °C and 500 °C normalized to the intensity of the G-mode. (b) Absolute intensities of the investigated modes normalized to the intensity of the D*-mode for different heating times and temperatures. The increase of the heating temperature was done consecutively.

decreases and the RBMs at 313 cm^{-1} (olive) and 326 cm^{-1} (purple) slightly increase. In consistency with section 7.1.2 this shows that outer layers contributing to the RBM at 148 cm^{-1} are removed due to their selective oxidation during heating in air. Thus, inner layers become more accessible to Raman spectroscopy, resulting in an increase of their intensities as show by the RBMs at 313 cm^{-1} and 326 cm^{-1}. Since the RBM at 148 cm^{-1} originating from outer layers contributes to the observed BBLM, the removal of these layers explains the rapid drop in intensity of the BBLM shown in figure 6.6a and figure 6.6b. The removal of outer layers starts above a temperature of 450 °C, which is slightly higher than the oxidation temperatures investigated in section 7.1.2 due to the formation of large bundles being more stable against oxidation than smaller bundles or individual CNTs.
Additional measurements, especially on individual bundles with varying outer diameters and different number of tubes, are needed to further investigate the behavior of the BBLM, which may provide the estimation of the number of CNTs and their outer diameter within a bundle.

6.3 Summary

In this chapter BLMs and the BBLM were investigated, which are coupled phonon modes arising from either inter-layer or inter-tube interactions. It was shown that the BLM frequencies of the three innermost layers within an individual MWCNT measured by confocal Raman spectroscopy could be simulated by a simple model

based on a one-dimensional chain of equally coupled harmonic oscillators. In this one-dimensional approach, curvature and surface effects are neglected. By assuming a scaled coupling between adjacent layers, the surface effect could be compensated, leading to a far better agreement of the simulated frequencies and the measured frequencies.
The BBLM predicted by Rahmani *et al.* originating from RBM modes being resonant at the used excitation energy was observed by FT-Raman spectroscopy using bulk samples consisting of bundles of mostly SWCNTs. We could show that the intensity of the BBLM rapidly drops when the contributing CNTs are removed by heating the sample above 450 °C in air.
Coupled phonon modes provide additional information about the inter-layer structure and their inter-tube alignment in the Raman spectra, which can usually only be obtained by HRTEM. A detailed correlation of HRTEM and Raman measurements for different individual MWCNTs and separated bundles may therefore allow one to simulate the BLMs and BBLMs for different diameters, providing a non-destructive tool for the determination of inter-molecular arrangements of the measured CNTs. As shown in chapter 7.1 and chapter 7.2 this is essential for the effective opening of CNTs, which is necessary for the preparation of peapods.

Chapter 7

Synthesis and characterization of peapods

Carbon nanotubes (CNTs) filled with fullerene molecules, so-called "peapods", recently have generated a lot of interest because of their potential for electronic applications. The fullerenes inside tune the properties of the nanotubes, e.g. soften the modes in nano-electro-mechanical devices [21, 22]. They offer the possibilities of building ambipolar CNT field effect transistors [19] and changing the properties of single electron transistors [20]. If the CNTs contain endohedral fullerenes, i.e. fullerenes with an atom inside, they form a model system for studying one-dimensional spin chains coupled to a ballistic conductor. This can lead to new spintronic devices, such as spin-qubit arrays for quantum information processing [23] as discussed in chapter 1.
Usually, peapods are produced from bulk material [132]. For electronic applications they are suspended in a solvent and dispersed on a substrate, before contacts are fabricated onto the individual CNTs for measurements [20, 100, 101]. This processing suffers from several disadvantages: it does not allow the controlled positioning of the nanotubes, the CNTs often cluster together in ropes, and the CNTs are rather short (< 1 µm) due to the sonication involved. Especially the latter inhibits the fabrication of more complicated device structures as needed for e.g. double quantum dots [102] or high-frequency irradiation [103].
CNTs synthesized by chemical vapour deposition (CVD), on the other hand, can be grown individually on predefined sites with lengths of several micrometers [25]. These CNTs have to be filled directly on substrate in order to keep these advantages. However, this approach has been accomplished only by very few groups so far [30, 31].
In this chapter a more detailed HRTEM study of the opening and filling process is presented. Opening by air oxidation and acid treatment are compared for CVD-grown CNTs for the first time.

7.1 Opening of carbon nanotubes

Like all CNTs grown in a catalytic process, CVD-grown CNTs have closed caps, which have to be opened before the CNTs can be filled. Opening of as-grown CNTs is achieved by oxidation, which can be carried out either by annealing in air [133] or acid treatment [134, 135, 136], the latter often followed by an annealing step [132]. However, the effects of chemical reactions depend strongly on the amount and environment of the reactants. Thus, individual CNTs on a surface are expected to behave differently towards chemical treatment compared to bulk samples.
Bulk samples of CNTs are usually purified by acid treatment and most of the studies on the opening of CNTs so far have been carried out with such kind of material. This way, the effects of acid treatment and oxidation in air are never truly separated. To discriminate between the defects created by those methods, the following study is divided into two parts: First, the effect of oxidation by acid treatment without and with a subsequent annealing step and second the oxidation by heating in air without prior treatment are investigated and compared for both individual CNTs and bulk samples. Structural characterization is done by HRTEM, which only shows a small region of the observed sample. For comparison, bulk samples are investigated with FT-Raman to obtain spectra that are characteristic for the whole sample.

7.1.1 Acid treatment

Because acid treatment is used to clean powder samples of CNTs [135], it removes catalyst particles from the substrate. Because CNTs are usually fixed to the catalyst particles, they become mobile during acid treatment and are removed from the substrates as well. This has been observed by others [30] and is the reason why oxidation using acid treatment has not been investigated so far for CNTs grown by CVD directly on substrates. However, if grown with sufficiently high yield, enough tubes remain on the substrate for analysis.
In order to directly study defects induced by the acid treatment, CNTs are grown at $T_{\mathrm{CVD}} = 1030\,^{\circ}\mathrm{C}$ on perforated Si_3N_4 membranes and investigated with HRTEM. According to chapter 4.5, mostly MWCNTs are expected at this growth temperature. Since HRTEM is an destructive characterization method, the samples are investigated after acid treatment only. To characterize the acid treatment process, bulk samples are grown on quartz glass substrates at the same growth temperature as used before for the perforated Si_3N_4 membranes and measured by using FT-Raman spectroscopy. Prior to each measurement, the samples are flushed in deionized water to remove acid residue from the sample. Series of the RBM region or the D/G-ratio were measured at the same position on the sample. The acid treatment is carried out at 100 °C in 5M HNO_3 stirred with 200 rpm. Figure 7.1a shows a HRTEM image of CNTs after such a treatment for three hours without subsequent annealing. The remaining CNTs

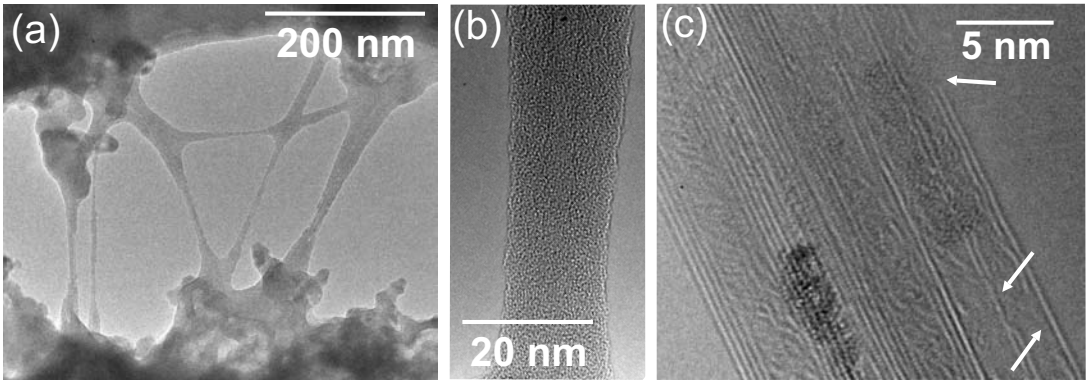

Figure 7.1: Samples after acid treatment: (a) The CNTs are covered with amorphous material. (b) Magnification of the residue covering the CNTs. A CNT is barely visible in the center. (c) Clean part of a sample with a rope of CNTs, where amorphous carbon can be seen inside the tubes. White arrows indicate defects on the rightmost DWCNT.

cluster together into thick ropes, which is expected since the CNTs are becoming mobile during acid treatment due to the removal of catalyst particles as mentioned above.
These ropes are strongly covered by amorphous material, as shown more closely in figure 7.1b. This coverage resembles the findings applied in [132] for bulk powder samples using much stronger acids and shorter reaction times, which suggests that individual CNTs on a surface seem to be affected much more by acid treatment than CNTs in a bulk powder sample. Obviously, they are more exposed.
Despite the coverage, parts of the tubes remain clean on the outside as shown for a rope in figure 7.1c. The CNTs seem to be filled with amorphous carbon. In principle, this feature could have its origin from material above or below the CNTs, because the focal depth of the HRTEM measurements is about 11 nm. However, it seems to be unlikely that the rope is covered from the top or bottom while the outer layers of the rope are free from any residue. It can therefore be assumed that the amorphous material resides within the CNTs.
Looking more closely at the DWCNT on the right of the rope in figure 7.1c, layer defects are clearly visible. Sites can be found where both layers are affected, shown by the upper white arrow, while the lower white arrows point to sites where only the inner layer of the DWCNT has been damaged while the outer layer remains unaffected. This is in contrast to prior reports of the oxidation of MWCNTs with much stronger acids, where the caps of CNTs could be opened selectively [134] due to their strong curvature induced by pentagonal carbon rings [137]. Instead Monthioux *et al.* assume that defects in the layers of CNTs induced by acid treatment occur at

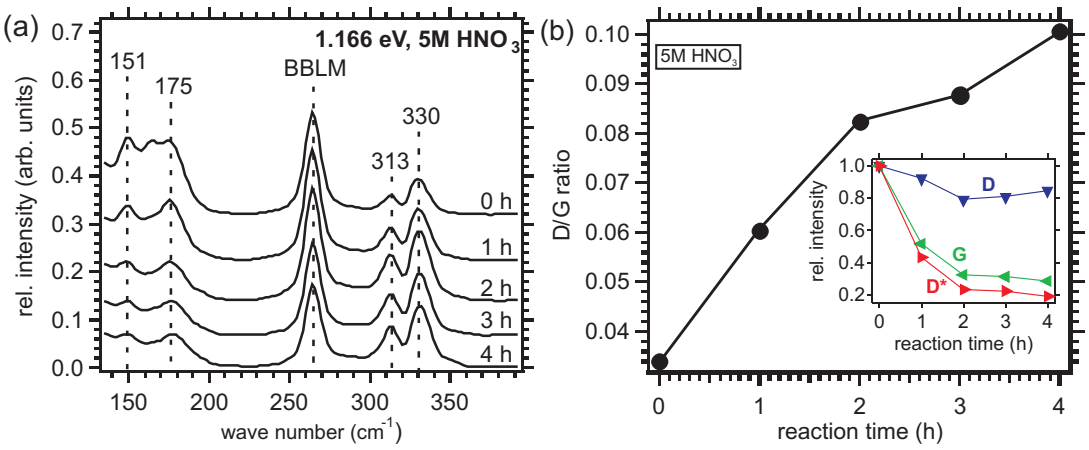

Figure 7.2: (a) Change of the relative intensities of the BLMs during acid treatment for bulk samples grown on quartz glass. The intensities are normalized to the intensity of the G-mode. (b) Change of the D/G-ratio during acid treatment. The inset shows the change in the relative intensity for the most prominent Raman modes.

pre-existing defects like Stone-Wales defects created during CVD growth [132].
HRTEM measurements only show a selected part of a sample and it is difficult to characterize a bulk sample by HRTEM alone. Therefore, FT-Raman spectroscopy is used to investigate the RBM region of bulk samples grown on quartz glass substrates during acid treatment. Since the CNTs are grown at $T_{\mathrm{CVD}} = 1030\,^{\circ}\mathrm{C}$ where we expect mostly MWCNTs, the observed peaks are BLMs (see chapter 6.1) originating from MWCNTs. Figure 7.2a shows the measured BLM spectra after different reaction times while their intensities are normalized to the intensity of the G-mode. The intensities of all modes are decreasing during acid treatment due to the removal of tubes from the substrate. This is not seen in figure 7.2a, which shows the relative intensities compared to the G-mode.
Two different groups of peaks can be identified on both sides of the BBLM at $265\,\mathrm{cm}^{-1}$, which was discussed in chapter 6.2. Its strong intensity indicates the high yield of CNTs on the sample, leading to large bundles. The left group showing peaks at $151\,\mathrm{cm}^{-1}$ and $175\,\mathrm{cm}^{-1}$ arises from CNTs with larger diameters than the CNTs that induce the right group with peaks at $313\,\mathrm{cm}^{-1}$ and $330\,\mathrm{cm}^{-1}$, where the relative intensities of all observed Raman modes stay nearly constant during acid treatment.
Furthermore, the D/G-ratio, given by the fraction of the intensity of the D-mode and of the intensity of the G-mode, was monitored during acid treatment, which increases with the reaction time as shown in figure 7.2b. To investigate if this increase of the D/G-ratio is due to an increase of the intensity of the D-mode, the relative intensities

of the most prominent modes, which are labeled by their name, are compared in the inset of figure 7.2b. During acid treatment the relative intensity of the D-mode remains almost constant, while the relative intensities of the other modes decrease significantly. This can be explained by the removal of CNTs from the substrate while the amount of amorphous carbon per remaining CNT increases. Thus, the increase of the D/G-ratio during acid treatment is due to an decreasing relative intensity of the G-mode caused by the removal of CNTs from the substrate, while the relative intensity of the D-mode increases, because of an increasing amount of amorphous carbon arising from oxidized CNTs, as shown in figure 7.1b.
Amorphous carbon covering the CNTs can be removed by subsequent annealing in air [135, 138] which is used to purify the CNTs after acid treatment [139]. It was carried out at 400 °C for 30 minutes, which decreases the thickness of the coverage by partially removing it, as shown in figure 7.3a. The inset shows that sites where the coverage is not completely removed are less homogeneous than before.
However, the tubes are not clean enough for filling and since carboxylic groups block the entry ports [140], another annealing step in vacuum ($p < 10^{-6}$ mbar) at 650 °C for 24 hours is added. Indeed the samples are much cleaner after this treatment, as shown in figure 7.3b. The ropes are now covered with small particles. Sometimes, layered structures within these particles are observed. They might be due to remaining

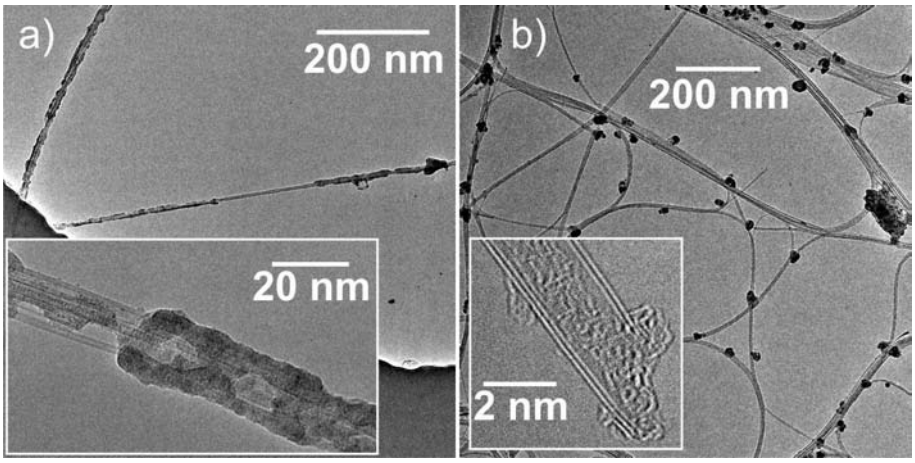

Figure 7.3: (a) Sample shown in figures 7.1 after heating in air. The coverage is only partially removed. (b) Sample after acid treatment and annealing in air followed by annealing in vacuum. The amorphous residue outside the tubes is removed by the last annealing step. Small crystals are attached along the CNTs. The inset shows the end of an opened DWCNT plugged with amorphous carbon.

catalyst particles contained within carbon shells, as discussed for similar objects in [132]. The interior of the CNTs is still plugged with amorphous carbon, as shown in the inset of figure 7.3b for the end of a DWCNT. A third wall starts forming from the amorphous carbon on the outside at the lower end of this tube induced by the electron irradiation. This process of graphitic shells forming from carbon material due to electron irradiation annealing is known since the early 1990s [141]. It could be observed for different samples by taking time series, whereas an example of the formation of a inner layer from encapsulated C_{60} molecules is discussed in section 3.2.2.

The cleaning of the acid treated samples by additional annealing is confirmed by FT-Raman measurements, where the samples are first placed into acid for 2 hours and afterwards flushed with deionized water. Then they are heated in air at 450 °C, while every ten minutes a spectrum was obtained as shown in figure 7.4a. After acid treatment (referred to as AT) the relative intensities stay almost constant which does not indicate a diameter selective oxidation. This is consistent with the data in figure 7.2a. Also after subsequential annealing, no significant change of the relative intensities of all observed modes could be observed.

The D/G-ratio shown in figure 7.4b increases significantly after acid treatment, while it decreases after subsequential annealing. This is due to an increase of the relative intensity of the D-mode after acid treatment, while the relative intensities of the G- and the D*-mode decrease as shown in the inset of figure 7.4b. After short

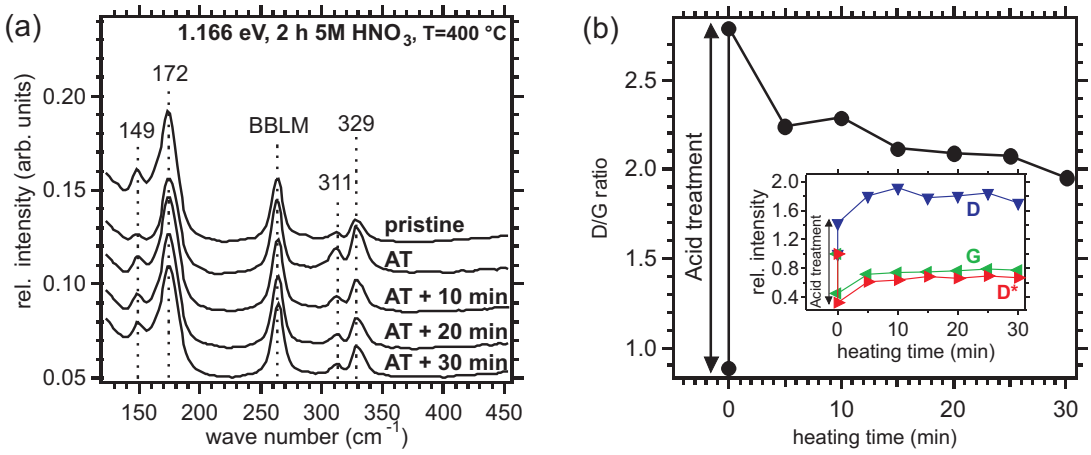

Figure 7.4: (a) Relative intensity of the BLMs during acid treatment (AT) followed by additional heating in air. (b) Change of the D/G-ratio for the same sample. The inset shows the change in the relative intensity for the most prominent modes during oxidation.

subsequential annealing (∼5 minutes) the relative intensities of all modes increase equally and stay constant for longer heating times. This is in agreement with the partial cleaning of acid treated CNTs after subsequential annealing in air due to the removal of amorphous carbon as observed by HRTEM in figure 7.3a. The increase of the relative intensities of the G- and D*-mode after short heating can be explained by a shielding effect induced by functional side groups and amorphous carbon, which reduces the overall intensity of CNTs coated with amorphous material, as assumed by Osswald *et al.* [142]. However, their relative intensities do not reach the starting value indicating that tubes are removed from the substrate during the acid treatment.

As a brief summary, it can be concluded that compared to CNT powder samples from arc discharge or PLV material, oxidation by acid treatment has a stronger effect on tubes grown directly on a substrate. The conditions for chemical treatment of individual CNTs should therefore be chosen carefully and should be much weaker than for bulk material.
A strong coverage with amorphous material appears directly after the treatment which is consistent to the measured increase of the D/G-ratio during acid treatment. The increase of the D/G-ratio arises from the increase of the intensity of the D-mode, while the G- and the D*-mode decrease due to the removal of CNTs from the sample. In powder samples the amorphous material has previously been ascribed to surfactant residues [136]. Since we grow the tubes directly on the TEM substrates, no surfactant is involved during the preparation. Instead, it is more likely that the residue consists of amorphous carbon from destroyed tubes or dissolved shells of MWCNTs. Furthermore, the acid treatment introduces functional side groups on the surface of CNTs, which could be shown by highly hydrophobic CNTs becoming hydrophilic after acid treatment and therefore being soluble in polar solvents like N,N-dimethylformamide (DMF) [143].
This coverage can be only partially removed by heating in air, while annealing in vacuum shows a much better result. However, afterwards small particles stick to the tubes. It is expected that these are catalyst particles covered with carbon shells. Since catalyst particles become mobile during acid treatment, the tubes are no longer fixed to the substrate either. Instead, they cluster together in thick ropes, which contain more tubes than the ropes in as-grown samples. Both effects are obstacles for further processing of individual tubes, e.g., for electronic devices.
The caps of the CNTs are opened. However, since defects could be observed on the layers of CNTs, this seems not to be a selective process. Layer defects occur even with rather mild acid treatment (compared to the conditions of reference [138]). We observed defects on the inner layers of DWCNTs while the outer layer remained unaffected. This could explain why the tubes are filled with amorphous material, since the remnants of inner layers stay inside. The finding that inner and outer layers are equally affected is supported by Raman measurements, where no diameter-specific

change of the intensities of the BLMs was observed after acid treatment.

7.1.2 Heating in air

Another way for opening the closed CVD-grown CNTs on substrates is oxidation by heating in air. This has been successfully applied by others before [30, 31]. Air annealing does not remove CNTs from the surface and does not change the catalyst particles either. Thus, the CNTs remain at their growth position and formation of ropes is due to the high yield of CNTs. The as-grown ropes contain fewer tubes than the agglomerated ropes of the acid treated sample, while the diameters of the CNTs are comparable.
In order to study the influences of heating in air, CNTs were grown at $T_{\mathrm{CVD}} = 940\,^{\circ}\mathrm{C}$ on Si substrates and investigated with AFM by using the tapping mode to exclude defects induced by the AFM tip. After heating the substrate at 700 °C in air for 10 minutes, nearly all CNTs on the substrates are removed, while the catalyst particles stay unaffected. If the heating temperature is reduced to 500 °C, CNTs on the substrate are partially decomposed forming small clusters of carbon as shown in figure 7.5a. This is in contrast to the observations of Ajayan *et al.* [133], who reported that oxidation of CNTs occurs only at temperatures above 700 °C. This discrepancy might be explained by the fact that Ajayan *et al.* investigated samples consisting of MWCNTs with more than ten walls, while in this study mostly DWCNTs are investigated, as discussed in chapter 4.5 for a growth temperature of $T_{\mathrm{CVD}} = 940\,^{\circ}\mathrm{C}$. This shows the necessity to characterize the pristine samples before the oxidation.
The heating temperature for the samples was then further reduced as shown in

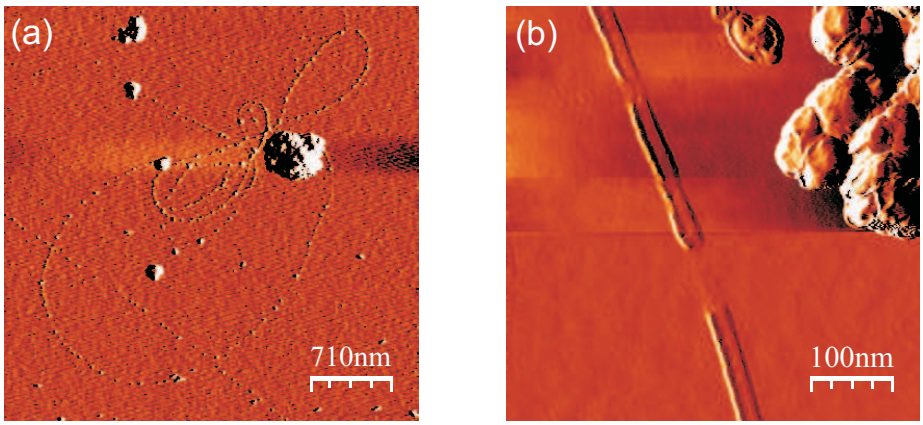

Figure 7.5: AFM images of individual CNTs heated in air at (a) 500 °C for 10 minutes and (b) 450 °C for 30 minutes.

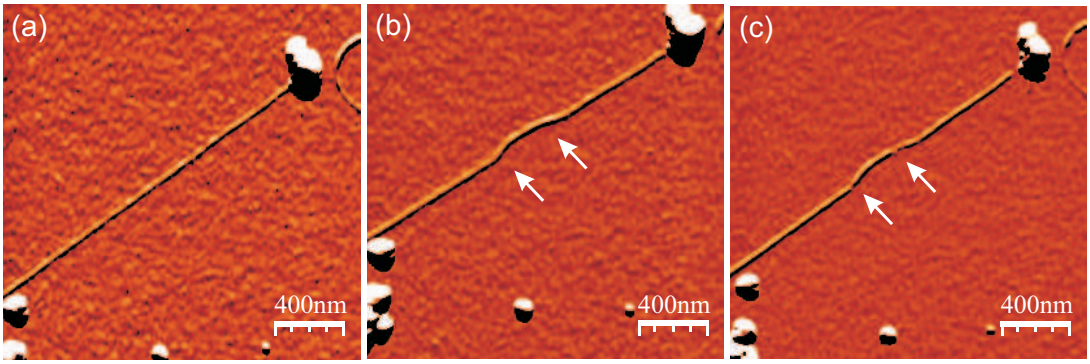

Figure 7.6: Investigation of an individual CNT after CVD growth heated at 450 °C for (a) 0 min, (b) 10 min and (c) 20 min. White arrows point to induced defects.

figure 7.5b for a sample heated at 450 °C for 30 minutes. It shows a CNT with a diameter of about $d_T = 2\,\text{nm}$, which is damaged at two positions. At this heating temperature, no CNTs are removed allowing a detailed investigation of an individual CNT with an outer diameter of about $d_T = 1.5\,\text{nm}$ during heating in air as shown in figure 7.6a. After heating at 450 °C for 10 minutes kinks are formed in the observed CNT indicating defects in the atomic structure of its layers (white arrows) as shown in figure 7.6b. Figure 7.6c shows the same CNT after a heating time of 20 minutes were the CNT starts to decompose at these positions. Further heating leads to a damage of the CNT as shown for the tube in figure 7.5b.

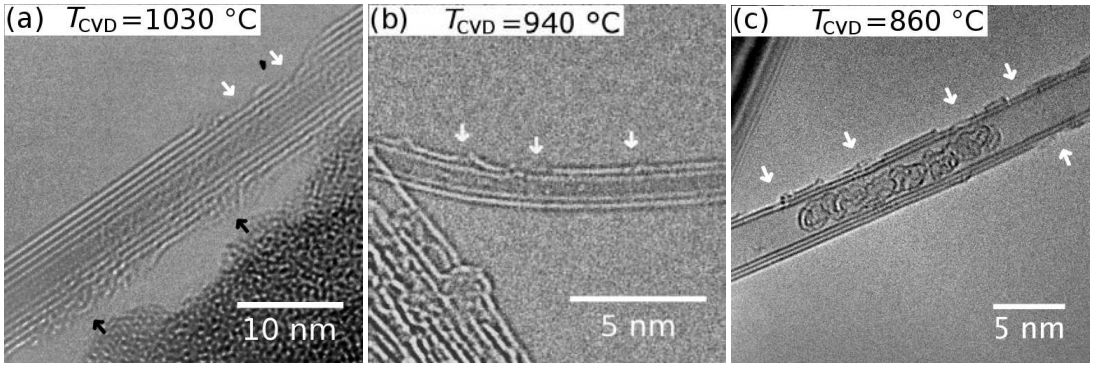

Figure 7.7: HRTEM measurements of CNTs after opening by oxidation in air synthesized at different growth temperatures T_{CVD}. White arrows indicate defects in the sidewalls of the investigated CNTs, while black arrows point at amorphous material surrounding the CNTs after oxidation.

For a more detailed investigation of defects in CNTs induced by heating in air, CNTs are grown on perforated Si_3N_4 membranes using different growth temperatures as shown in figure 7.7. This allows the investigation of CNTs with different numbers of layers by using HRTEM. All samples were oxidized at 450 °C for 20 min after CVD growth. It is clearly shown for all samples that defects are created in the outer layers (white arrows). Amorphous material from collapsed sidewalls is surrounding the CNT in figure 7.7a (black arrows). The DWCNT shown in figure 7.7b shows a defect in its innermost layer at a site where the outer layer is already removed, which indicates that this tube is opened. In contrast to the MWCNT in figure 7.7a, which is still closed by remaining layers, the DWCNT in figure 7.7b and the DWCNT in figure 7.7c are filled with amorphous material. HRTEM measurements confirm that this amorphous material within the CNTs is quite moveable. Since no defects on the inner layer could be investigated for the DWCNT in figure 7.7c, this might indicate that this DWCNT is also opened, leading to amorphous carbon from former layers being sucked into its inner hollow through an opened entry port not seen in the image. This is shown more clearly in figure 7.8 for a bundle of DWCNTs, which shows opened entry ports (white arrows) after heating at 450 °C for 20 minutes. Several DWCNTs are filled with amorphous material, which plug the opened entry ports. This amorphous material inside the CNTs could be observed only very rarely for CNTs investigated directly after CVD growth (see figure 4.6b in chapter 4.5). The inset of figure 7.8 shows an individual SWCNT from the same sample. Clear layer defects can be seen, which are also plugged with amorphous carbon. This effect of amorphous carbon being sucked inside CNTs during heating in air has been observed

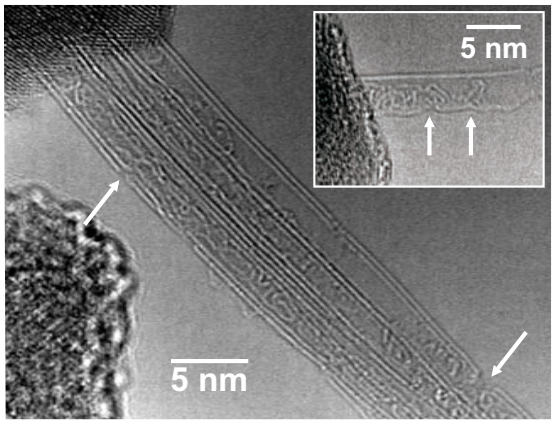

Figure 7.8: Rope of DWCNTs showing opened entry ports (white arrows) after heating at 450 °C for 20 min. This allows amorphous material to creep inside the holes as shown in the inset for a SWCNT.

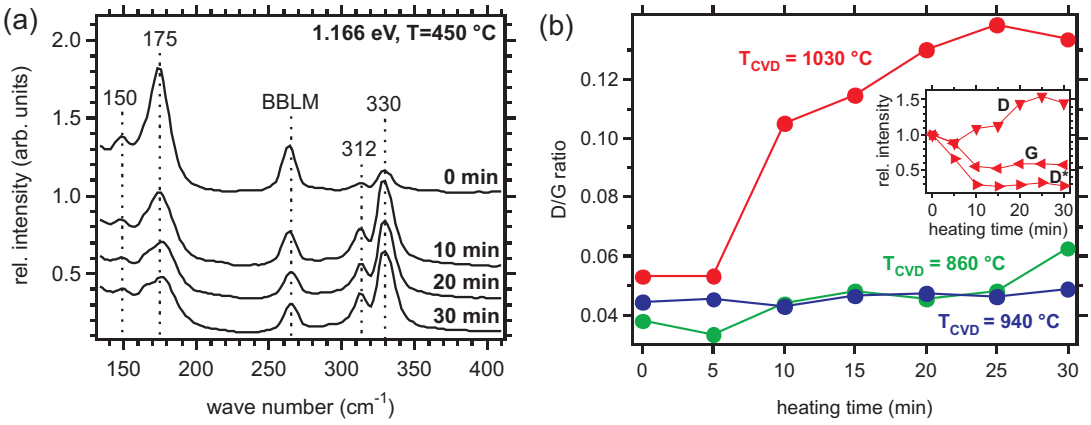

Figure 7.9: (a) Change of the BLM region for a sample grown at $T_{\mathrm{CVD}} = 1030\,^{\circ}\mathrm{C}$ and (b) the D/G-ratio for samples grown at different growth temperatures T_{CVD} during heating. The inset shows the relative intensities of the most prominent Raman modes.

before for MWCNTs by Ajayan *et al.* [133].
In contrast to the acid treated samples, no defects on inner layers can be observed with the outer layers remaining unaffected. Further oxidation predominantly occurs at defect sites, and thus, CNTs are opened starting from the outer layers. Therefore, opening of MWCNTs needs longer heating times than for DWCNTs as shown for the MWCNT in figure 7.7a compared to DWCNTs shown in figure 7.7b, figure 7.7c and figure 7.8. Thus, the optimal heating time to open a CNT without inducing too much damage depends on their growth temperature T_{CVD}.
In order to study the effects of the heating in air on CNTs with different diameters, FT-Raman spectra of the RBM region are obtained for bulk samples after different reaction times as shown in figure 7.9a. During heating in air, the intensity of the BLMs at $149.7\,\mathrm{cm}^{-1}$ and $174.5\,\mathrm{cm}^{-1}$ belonging to tubes with larger diameters is reduced, while it is increased for tubes with smaller diameters showing BLMs at $312\,\mathrm{cm}^{-1}$ and $329.8\,\mathrm{cm}^{-1}$. This effect can be observed after short heating times (∼5-10 minutes), while longer heating shows no further changes in the Raman spectrum. The relative intensity of the BBLM stays nearly constant during heating in air.
Furthermore, the D/G-ratio is investigated for CNTs grown at different temperatures T_{CVD} on Mo samples, as shown in figure 7.9b. The absolute values of the D/G-ratio for the pristine samples are increasing with growth temperature, indicating that the amount of amorphous carbon and defects are increased. CNTs synthesized at $T_{\mathrm{CVD}} = 1030\,^{\circ}\mathrm{C}$ show a strong increase of the D/G-ratio with heating time, which

is strongest between 5 and 10 minutes and saturates after 20 minutes. The inset of figure 7.9b shows for these CNTs that the increase of the D/G-ratio is mainly due to an increase of the relative intensity of the D-mode, though the intensities of the other modes are slightly reduced. For CNTs grown at $T_{\mathrm{CVD}} = 940\,℃$ and $T_{\mathrm{CVD}} = 860\,℃$, no or only a slight increase is observed. This is in agreement with the fact that oxidation occurs preferably at defect sites, since samples grown at $T_{\mathrm{CVD}} = 1030\,℃$ show also the highest D/G-ratio before oxidation. Furthermore, according to chapter 4.5 CNTs synthesized at higher T_{CVD} have on average a larger outer diameter providing a larger surface for oxygen molecules to react. However, from these explanations one would expect a stronger increase of the D/G-ratio for the sample grown at $T_{\mathrm{CVD}} = 940\,℃$ than actually observed. Thus, other effects have to come into play to explain this result. One possibility could be the creation of more defects due to the larger number of layers for CNTs synthesized at $T_{\mathrm{CVD}} = 1030\,℃$, because more amorphous material is created from former layers (see black arrows in figure 7.7) leading to an increase of the intensity of the D-mode.

In summary the CNTs are opened after oxidation as indicated by defects in their layers observed by HRTEM for all investigated methods. The oxidation by acid treatment for a few individual CNT on a surface has a stronger impact compared to bulk material and the conditions of the reaction need to be adapted. For heating in air, the conditions are very similar to those used for treatment of bulk samples, but since the oxidation starts at the outer sidewalls, the reaction time for the opening of an individual CNTs also depends on its number of layers. Therefore, it is essential to characterize the pristine samples before opening to determine the number of layers and the yield of CNTs in the sample. This allows one to adjust the optimum oxidation temperature and heating time, avoiding the decomposition of CNTs or the introduction of too much damage, as shown by AFM on individual CNTs.
Catalyst particles are removed by acid treatment. Thus, CNTs are no longer fixed and cluster together in thick ropes or are removed from the substrate. Furthermore, the acid treated CNTs show a strong coverage with amorphous material in HRTEM images. This coverage can be only partially removed by heating in air, while annealing in vacuum shows a much better effect. This is confirmed by FT-Raman measurements of the D/G-ratio, which is increasing due to the strong coverage with amorphous material. After subsequential annealing in air the D/G-ratio is decreasing without reaching its original value due to the removal of CNTs from the substrate.
In contrast to the acid treatment, opening by heating in air only produces small amounts of amorphous carbon on the outer layers of the CNTs. This is in agreement with the change of the D/G-ratio during the opening process. The amount of amorphous carbon and defects are increased for CNTs grown at higher temperatures. Monthioux *et al.* argue that due to the more stable structure of individual layers, defects must be present in the layers before oxidation to induce layer defects [132].

Such disclinations like Stone-Wales defects, a twinned pentagon-heptagon pair increasing the curvature of the CNTs, result in sharp kinks as observed with AFM measurements in figure 7.6 during oxidation. This explains the observation of defects in the layers of CNTs for both oxidation methods investigated in this chapter. Because more residual material is produced at higher growth temperatures due to the increased decomposition of methane, it can be expected that more defects are formed for CNTs synthesized at higher temperatures, which occur preferably in the presence of attached residue material on the outer layers.
Residue material could also be observed within the CNTs by using HRTEM, with the amount of this material being much higher for the acid treated samples. A comparison of the resonant RBM spectra indicates that the thermal oxidation removes the outer layers leading to smaller diameters, while the acid treatment is affecting the CNTs from inside and outside alike. This is confirmed by HRTEM measurements where for thermal oxidation, defects can be observed on the outer layers, while the acid treated samples show defects on outer as well as inner layers. Thus, the high amount of residue material investigated within the CNTs after acid treatment may consist of remnants from destroyed inner layers. With heating in air, on the other hand, the inner layer is oxidized after the outer layers as suggested, but not shown by Chikkannanavar *et al.* [30]. Amorphous carbon is sucked inside, plugging the entry ports of the opened CNTs, which leads to the smaller amount of amorphous material inside the CNTs.
The bundling of CNTs after acid treatment due to the removal of catalyst particles and the strong coverage of the CNTs with amorphous carbon blocking their entry ports are obstacles for further processing of individual CNTs, for example, for electronic devices. Furthermore, CNTs are affected on the outermost and the innermost sidewall as well leading to a high amount of amorphous carbon within the CNTs, which prevents later filling. Thus, opening the CNTs by heating in air is the preferred method, which will be used to open CNTs in the following. However, if the individual tubes and the catalyst particles are somehow fixed to the substrate, for instance, with electrodes, and the as-grown CNTs consists mostly of SWCNTs, acid treatment might be still an option.

7.2 Filling CNTs with C_{60} molecules

CNTs filled with C_{60} molecules, so-called peapods, are usually produced from bulk material [132]. In order to produce individual peapods which are usable for transport measurements, this has to be achieved from CVD-grown CNTs directly on substrates. This is more challenging due to the limited methods to clean the CNTs before and after filling without removing them from the substrate, e.g. as reported for sonication methods [144]. Therefore, the filling of CVD-grown CNTs directly on the substrate

could only be achieved by a few groups so far [30, 31].
Several filling methods can be used, while the solvent filling [54, 145, 146] and the vapor filling [30, 147] are the most common. Both methods use different ways to transport the C_{60} molecules to the entry ports of the CNTs. While during solvent filling, the samples are placed in a solution saturated with C_{60} molecules, they are directly evaporated onto the outer layers of the opened CNTs at pressures below 10^{-6} mbar during vapor filling. In this thesis, vapor filling is used, which will be studied in the following for CNTs grown by CVD directly on substrates.
For bulk material, vapor filling is commonly achieved by placing the CNTs together with C_{60} powder inside a quartz glass tube, which is evacuated ($p < 10^{-6}$ mbar) and sealed afterwards. According to Mathews *et al.* [148] the sublimation temperature T_{Sub} of C_{60} as a function of the pressure p is given by

$$T_{\mathrm{Sub}}[℃] = \frac{-9777 \pm 138}{\log p[\mathrm{mbar}] - 9.582 \pm 0.126} - 273.15. \tag{7.1}$$

Thus, for pressures below $p = 10^{-6}$ mbar, sublimation starts approximately at 400 ℃. Therefore, the sealed quartz glass tube is heated at 450 ℃ for 72 hours in order to sublime the C_{60} molecules, which condense on the outer surface of the opened CNTs. These C_{60} molecules are quite mobile, allowing surface diffusion as investigated by Smith *et al.* during *in situ* annealing above 325 ℃ [136]. Molecular dynamic calculations by Berber *et al.* show that the optimum temperature for the peapod formation is close to 400 ℃, allowing surface diffusion until a defect is reached and the C_{60} molecule can enter the CNT [149]. This is an exothermic process in which an individual C_{60} molecules gains an energy of 0.51 eV when entering a (10,10) SWCNT and stays inside the tube afterwards [150].
Different cleaning methods to remove the C_{60} molecules sticking to the surface of the CNTs after filling have been used. Their effect on the CNTs and fullerenes is discussed in the following. Figure 7.10a shows an individual CNT, that was cleaned by stirring the sample for one hour in toluene. After this procedure, individual CNTs are still strongly covered with C_{60} molecules as indicated by HRTEM measurements shown in figure 7.10a, which prevents the investigation of their atomic structure and their filling.
If the CNTs are stirred in 1-phenylnaphthalene, which provides a higher solubility of C_{60} (50 mg/ml) compared to toluene (2.8 mg/ml) [151] after vapor filling, the coverage of individual CNTs is slightly reduced, as shown in figure 7.10b, allowing the observation of individual C_{60} molecules at the surface of the CNTs. But the coverage is still too thick to further investigate the shown CNT. The white arrow points at a side where C_{60} molecules could be partially removed from the surface of the tube.
Figure 7.10c shows a HRTEM picture of a sample that was annealed at 600 ℃ at a pressure below 10^{-6} mbar for 20 hours. The coverage of the CNTs with C_{60} could be further reduced, as indicated by clean regions marked by the white arrows, but

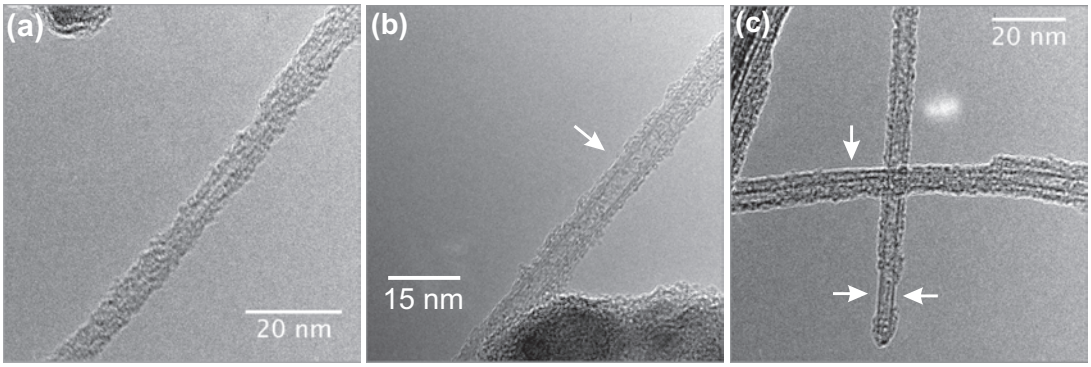

Figure 7.10: Strong coverage of individual CNTs with C_{60} molecules after vapor filling using a quartz glass tube and additional cleaning by (a) stirring for 1h in toluene, (b) stirring for 1.5 hours in 1-phenylnaphthalene and (c) heating at 600 °C for 20 hours at a pressure below 10^{-6} mbar. White arrows point at sites of CNTs which are partially cleaned from C_{60} molecules.

at least one monolayer of C_{60} remains sticking to the outer sidewall of the CNTs, and could not be removed by further stirring or annealing after the exposure to air. A possible explanation is that C_{60} molecules react with the outer layers of the CNTs and are afterwards hard to remove from the CNTs. This finding is consistent with observations of Smith *et al.*, who observed that damaged C_{60} molecules on the surface of CNTs are not moveable anymore and become fixed during annealing at low pressures [136].
As discussed above, the entry ports of oxidized CNTs are often plugged with amorphous carbon preventing their filling with C_{60} molecules. This material plugging the entry ports of oxidized CNTs can be removed with an additional annealing step in vacuum as suggested by Ugarte *et al.* [152], which removes exterior amorphous material from the outer layers of CNTs. Thus, CNTs could only be filled if the sample was annealed at high temperatures in vacuum ($p < 10^{-6}$ mbar) directly after opening. When a sample was exposed to air for several hours a removal of these plugs was not possible anymore, which suggest reactions of the amorphous material and the defect sites with the atmosphere forming oxygenic compounds. Thus, after opening of the CNTs by heating in air, they are additionally annealed in vacuum directly after their opening, which cleans the outer layers from amorphous carbon and opens their entry ports, leading to CNTs that are ready to be filled with C_{60}.
For this purpose, a UHV-chamber was built as shown in figure 7.11a. It is equipped with a micro-evaporator and an additional substrate heating, which are regulated by two independent temperature controllers up to 900 °C. The turbo pump with a backing pump allows pressures down to 10^{-8} mbar inside the UHV-chamber.

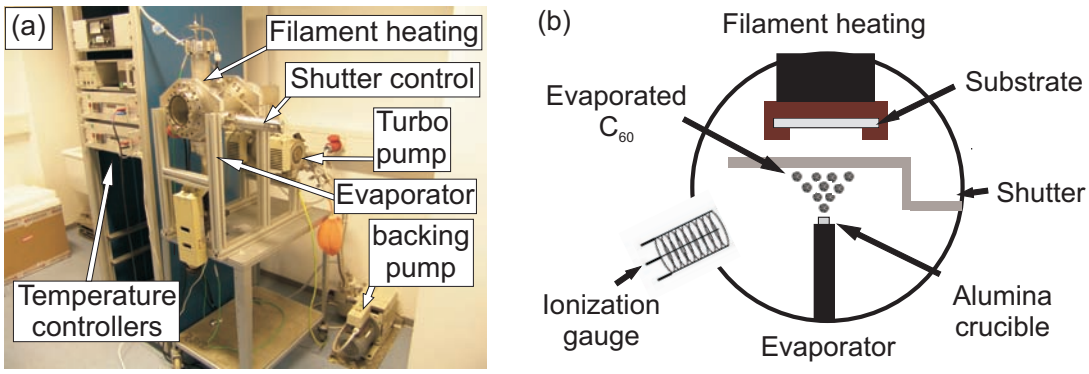

Figure 7.11: (a) Setup of the built UHV-chamber. (b) Schematic illustration of the vapor filling inside the UHV-chamber.

Figure 7.11b shows the schematic illustration of the vapor filling inside the chamber, where C_{60} powder is filled inside an alumina crucible located within the evaporator. Directly before the evaporation of the C_{60} molecules on the substrate, the oxidized CNTs are heated up to 900 °C for 1.5 hours below 10^{-6} mbar to remove amorphous carbon plugging the entry ports. The C_{60} molecules are evaporated at a pressure of 10^{-6} mbar onto the substrate, while the shutter allows one to define the evaporation process for a selected period of time. Additional heating of the sample to about 100 °C during evaporation allows one to control the thickness of the coverage with C_{60} molecules, which decreases with increasing substrate temperature. Thus, a more controlled deposition of C_{60} molecules on the CNTs was achieved. After evaporation, the sample is held at a temperature of 400 °C for 48 hours to allow surface diffusion of the C_{60} molecules until they enter the CNTs through defect sites forming peapods. Afterwards, the sample is cleaned of exterior C_{60} by a final annealing step at 650 °C and pressures below $p = 10^{-6}$ mbar for more than 48 hours. Thus, besides the better control of the C_{60} evaporation using vapor filling inside the UHV-chamber, this method also allows the *in situ* cleaning of the CNTs from exterior C_{60} molecules without exposing the sample to air. At higher annealing temperatures after filling, the coalescence of interior C_{60} molecules forming a new inner tube could be investigated by HRTEM. This was also observed by Bandow *et al.* for filled SWCNTs which form DWCNTs above ∼800 °C [153].
When the period of time for the encapsulation of C_{60} molecules is too short, partial filling can be observed as seen for a sample in figure 7.12, which was annealed at 400 °C for only 24 hours after the evaporation of C_{60}. The encapsulated C_{60} molecules are pushed inside the shown SWCNT by further C_{60} molecules entering the entry ports.
When the sample is held at a temperature of 400 °C for 48 hours after the evaporation

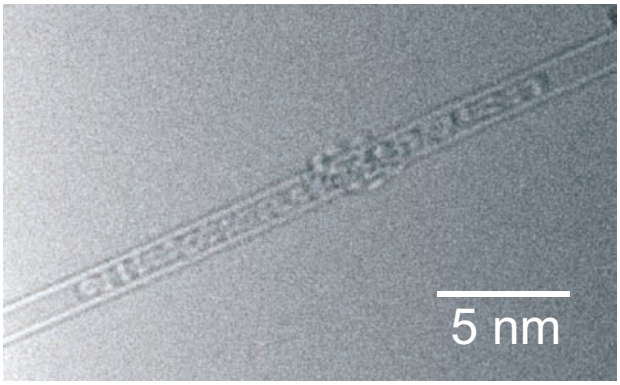

Figure 7.12: Partial filling of a SWCNT heated at 400 ℃ for only 24 hours after the evaporation of C_{60}.

of C_{60}, allowing a longer surface diffusion of the C_{60} molecules before entering the CNTs through opened entry ports, clean peapods could be synthesized from CNTs with different number of layers as shown in figure 7.13. Due to the *in situ* cleaning by annealing at low pressures, the filling of individual peapods can be observed by HRTEM. As mentioned before in chapter 4.5, it can be seen that the number of sidewalls and the diameter of the CNTs are increasing with T_{CVD}.
As discussed in chapter 2.7, different ordered phases of C_{60} molecules can be observed inside the CNTs depending on their inner diameter [54] shown by the white arrows in figure 7.13. While an amorphous phase of C_{60} molecules is shown in figure 7.13a, a straight chain phase and a zigzag phase can be found in figure 7.13b and figure 7.13c

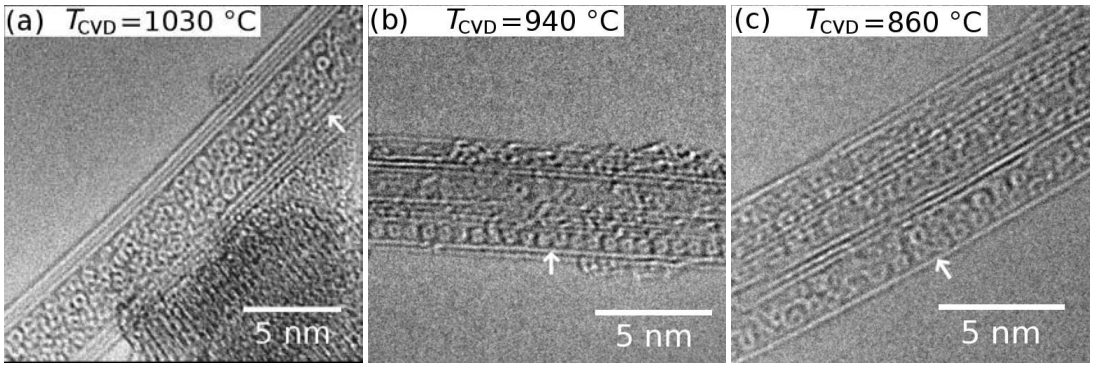

Figure 7.13: HRTEM measurements at 80 keV of peapods synthesized from CNTs grown at different growth temperatures T_{CVD}. White arrows point at different ordering phases of the C_{60} molecules inside the CNTs.

respectively.
All samples were oxidized for 20 minutes at 450 °C except the sample synthesized at T_{CVD} = 1030 °C (figure 7.13a), which was opened by oxidation at 500 °C for 20 minutes due to the larger number of sidewalls of CNTs in the sample. Thus, the *in situ* cleaning of the samples within the UHV-chamber leads to cleaner surfaces compared to the other investigated cleaning methods.
Besides HRTEM, confocal Raman spectroscopy helps to prove the filling of CNTs with C_{60} molecules by its characteristic C_{60} modes. Figure 7.14 shows the Raman spectrum of a C_{60} crystal measured at room temperature. The red curve was measured with FT-Raman spectroscopy at a laser wavelength of $\lambda = 1064\,\text{nm}$, while the blue curve is obtained by confocal Raman spectroscopy at a laser wavelength of $\lambda = 488\,\text{nm}$. The characteristic modes of C_{60} are marked with their designations. The intensity of all modes is considerably smaller for the confocal Raman spectrum as compared to the FT-Raman spectrum. This is expected since FT-Raman spectroscopy illuminates a larger area of the sample, which results in a higher intensity of all C_{60} modes. The most prominent mode at $\lambda = 1064\,\text{nm}$ is the $A_g(2)$-mode and we will focus on this mode in the following. It arises from an in-phase stretching of the diameters of all pentagons within the C_{60} molecule and is very sensitive to distortions induced into the fullerene cage. Compared to the FT-Raman spectrum, the confocal Raman spectrum shows two significant differences for this mode. First, its relative intensity is significantly suppressed and secondly, its frequency shows a small down-shift. While the $A_g(2)$-mode is located at $1469\,\text{cm}^{-1}$ for a laser wavelength of $\lambda = 1064\,\text{nm}$, it

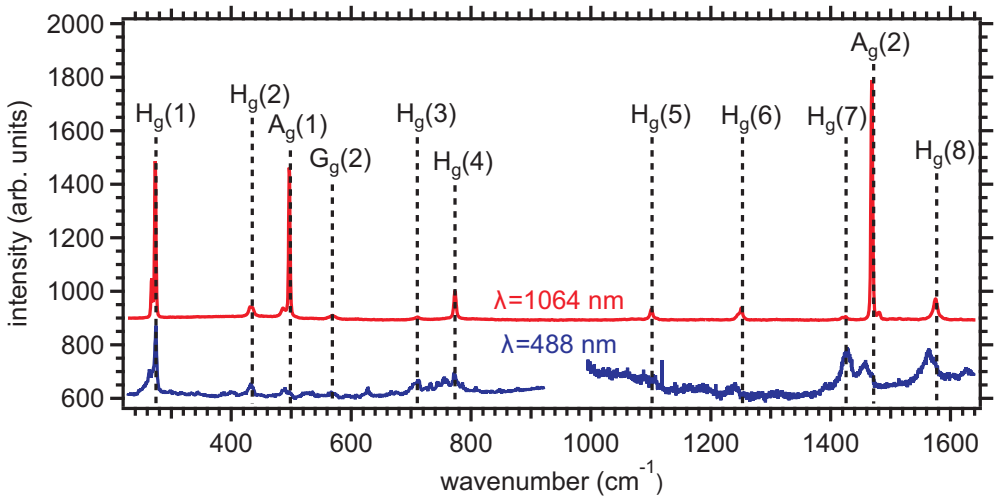

Figure 7.14: Comparison of the Raman modes of a C_{60} crystal measured at a laser wavelength of $\lambda = 1063\,\text{nm}$ (red curve) and $\lambda = 488\,\text{nm}$ (blue curve).

appears at 1459 cm^{-1} for $\lambda = 488$ nm. The reason for the differences in the two spectra measured at different laser wavelength is the photopolymerization of the C_{60} molecules, which was first noted by Rao *et al.* [154]. They observed a downshift of $\sim$9 cm^{-1} after photopolymerization, which forms polymers of C_{60} molecules via the [2+2] cycloaddition reaction [155]. Wang *et al.* discussed the kinetics of the C_{60} photopolymerization reaction and estimated an activation energy of 1.25 eV [156]. This is consistent to the measured spectra, while the laser wavelength of $\lambda = 1064$ nm and $\lambda = 488$ nm corresponding with a energy of 1.17 eV and 2.54 eV are below and above the required activation energy for the photopolymerization respectively.
In order to investigate synthesized peapods, a sample with a high yield of CNTs was grown at $T_{CVD} = 925$ °C on a perforated Si_3N_4 membrane and filled with C_{60} as shown by the HRTEM image in figure 7.15a. It shows a bundle of mostly DWCNT peapods, while exterior C_{60} molecules could be completely removed by the *in situ* cleaning. Images from different sites of the sample indicate a high yield of synthesized peapods, which is difficult to determine quantitatively, since individual peapods could not be separated within a bundle in the HRTEM images.
Figure 7.15b shows the Raman spectrum of the same sample, which was measured by using an Ar laser at a wavelength of $\lambda = 488$ nm in a confocal setup. From the estimated yield of CNTs within the sample we can conclude that the observed spectrum arises from a few hundred CNTs illuminated by the laser spot with a

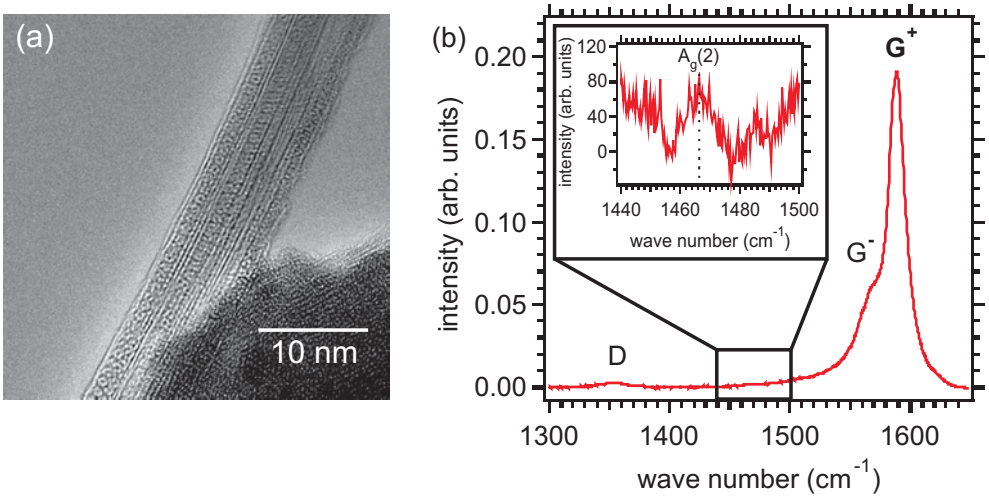

Figure 7.15: (a) HRTEM image of a cleaned peapod sample grown on a perforated Si_3N_4 membrane. (b) Confocal Raman spectrum of the same sample measured at a wavelength of $\lambda = 488$ nm. The inset shows the observed down-shifted $A_g(2)$-mode of interior C_{60} molecules.

diameter of ∼1 µm, while most of the CNTs are filled with C_{60} molecules as seen in figure 7.15a. The inset of figure 7.15b is a zoom-in of the $A_g(2)$-mode of interior C_{60}. Its frequency is down-shifted by ∼3 cm^{-1} with respect to C_{60} crystals measured at a laser wavelength of $\lambda = 1064$ nm. Although photopolymerization is expected, the down-shift of the $A_g(2)$-mode is surprisingly small. A similar down-shift of the $A_g(2)$-mode was observed by several authors [147, 157, 158], which assume photopolymerization of the C_{60} molecules inside the CNTs induced by the laser irradiation. They argue that the deviance of this down-shift compared to C_{60} crystals is due to the formation of one-dimensional polymers inside the CNTs. This assumption is confirmed by HRTEM studies of Hirahara *et al.* [159] and Zhou *et al.* [158], who observed an intermolecular distance for C_{60} molecules in peapods that is smaller than for bulk crystals, but larger than for C_{60} polymers being consistent with XRD studies [147].
However, the down-shift observed for peapods in figure 7.15b is in good agreement to the published results, which confirms the high quality of the produced peapods directly on substrates. This offers a non-destructive confirmation of the peapod synthesis. Because of the small intensity of the $A_g(2)$-mode compared to the modes of the CNTs, this method is only accessible for bulk samples with a high filling percentage. Furthermore, several authors observed a shift of about 3 cm^{-1} in the frequency of the RBMs after filling, due to interactions between the interior C_{60} molecule and inner SWCNT [31, 71, 160], which may provide the confirmation of the filling of individual CNTs.

In summary, vapor filling of opened CNTs was achieved by placing the sample together with C_{60} powder inside an evacuated quartz glass tube. This leads to a strong coverage of the CNTs with C_{60} molecules preventing the investigation of their inner hollow. In addition to cleaning the sample by stirring in toluene and 1-phenylnaphthalene annealing in vacuum is most effective, although C_{60} sticking at the outer surface could only be partially removed
After the exposure of the sample to air for several hours a removal of amorphous carbon plugging the entry ports of the opened CNTs and exterior C_{60} molecules after filling was not possible anymore, which suggests reaction with the CNTs. This could be avoided by a custom-built UHV-chamber, which facilitates not only the removal of amorphous material from the outer layers of the CNTs before filling, but also the cleaning of the peapods *in situ* after filling. These additional annealing steps in vacuum are essential to fill the CNTs by opening the entry ports of the oxidized CNTs and to investigate their inner hollow by HRTEM.
This makes the production of clean peapods with different numbers of layers possible, while the period of time for the annealing of the substrate at 400 °C is directly influencing the filling yield. This synthesis step promotes the surface diffusion of the C_{60} molecules on the outer layers of the CNTs until an entry port is reached and

leads to partial filling for a annealing time below 48 hours.
Besides HRTEM, filling of bulk samples can be confirmed with non-destructive Raman spectroscopy by a down-shift of the $A_g(2)$-mode, which is consistent with the results of other authors. But due to the small intensity of the $A_g(2)$-mode compared to the Raman modes of the CNTs, this method is only feasible for bulk samples with a high filling yield.

7.3 Summary

In this chapter we showed that the filling of CNTs directly on substrates is possible, resulting in clean peapods that can be used for later transport measurements. Two different commonly known methods for the opening of as-grown CNTs in bulk powder samples were adapted for use with individual CNTs on substrates, which were studied and compared with each other. These are oxidation by acid treatment and oxidation by heating in air. In contrast to acid treatment, which removes catalyst particles leading to the formation of thick bundles, heating in air does not remove catalyst particles, allowing the investigation of individual CNTs during heating as shown by AFM measurements. Furthermore, the acid attacks the CNTs from inside and outside leaving a large amount of amorphous material inside the CNTs which originates from former layers. This prevents the filling of these CNTs. Heating in air on the other hand, oxidizes the CNTs selectively from the outside, which reduces the amount of amorphous carbon inside the CNTs significantly. The entry ports of these tubes are often plugged with amorphous material, which can be removed by subsequential annealing in vacuum. This results in clean and open CNTs that are ready for filling.
A UHV-chamber was set up for the filling of the CNTs, which allows for control of the amount of evaporated C_{60} by additionally heating the substrate. Furthermore, the UHV-chamber is used to clean the sample after filling *in situ* by heating the substrate above the sublimation temperature, removing excessive fullerene molecules completely. The remaining tubes and peapods are very clean on the outside allowing detailed HRTEM studies. This was not possible for samples exposed to air after C_{60} evaporation for several hours, suggesting that reactions between C_{60} and the outer layers of CNTs are induced. Similar effects could be observed for amorphous material, which was sucked inside the opened entry ports of the CNTs after opening and could only be removed by heating at a temperature of 900 °C and pressures below 10^{-6} mbar for 1.5 hours directly after opening.
HRTEM images of *in situ* cleaned samples show that interior C_{60} molecules form different phases depending on the diameter of the CNTs. Raman spectroscopy as a non-destructive method is used to detect the C_{60} molecules inside the CNTs by observing a shift of the $A_g(2)$-mode in cleaned bulk samples of peapods, which is

consistent with the results of other authors.

Chapter 8

Conclusions and Outlook

In this thesis carbon nanotubes (CNTs) were synthesized by chemical vapor deposition (CVD) in order to fill them with C_{60} molecules directly on substrates. A detailed characterization of the as-grown pristine material at different growth temperatures with different catalysts permits the improvement of the synthesis parameters. We showed that the yield of synthesized CNTs can be controlled by the amount of catalyst particles on the substrate, while the number of layers and the mean diameter is influenced by the growth temperature T_{CVD}.
Due to the invasive behavior of high-resolution transmission electron microscopy (HRTEM), even at electron energies as low as 80 keV, this characterization method is only feasible as the last step and needs perforated substrates. While the surface of a CNT can be characterized by atomic force microscopy (AFM) or scanning electron microscopy operated under ultra-high vacuum conditions (UHV-SEM), an investigation of the inner structure including its number of layers or its filling is, in general, not possible with these methods. Therefore, the usability of Raman spectroscopy as a method for the pre-characterization of the studied samples was investigated. This is quite challenging since Raman spectroscopy mainly probes the electronic properties of the measured CNTs, which are influenced by different effects like purity, yield and their inter- and intra-molecular arrangement. Therefore, it is difficult to disentangle the atomic structure of an individual CNTs by Raman spectroscopy alone.
This difficulty could be overcome by a direct correlation of HRTEM and Raman spectroscopy on the same individual CNT. In this way, we were able to study the influences of the atomic structure on the obtained Raman spectra for both single-walled CNTs (SWCNTs) and multi-walled CNTs (MWCNTs). The most powerful feature within Raman spectroscopy is the radial breathing mode (RBM) providing the determination of the diameter of inner layers of MWCNTs, which is most important for later filling. The strong resonance behavior of the RBM is ambivalent: On the one hand, it allows for the separation of individual CNTs in a bundle, which is not possible by using HRTEM. On the other hand, the RBM of an individual CNT is hard to find without any additional information about the diameter due to the very small window of this

resonance. Thus, at selected positions, where an individual SWCNT could be located with either AFM or UHV-SEM, the sample has to be scanned using resonant Raman spectroscopy (RRS) by tuning the laser excitation energy in small steps, which makes this method extremely time-consuming.
However, when the RBM can be obtained it provides information about the diameter of the corresponding SWCNT, but also its family in the Kataura plot, which defines its electronic behavior. Furthermore, a correlation of RRS and HRTEM on the same individual MWCNT makes a determination of both its optical transition energy and its diameter possible with high accuracy. This offers not only an assignment of the measured CNTs to their family, but also a determination of their family branch, which permits one to distinguish between metallic and semimetallic SWCNTs. This is extremely important for the interpretation of future transport measurements.
In this thesis, coupled phonon modes were investigated for an individual MWCNT and a small bundle of SWCNTs for the first time experimentally. These modes arise from the coupling between adjacent layers in MWCNTs or in bundles due to vdW interactions. Thus, in the case of MWCNTs breathing-like modes (BLMs) are observed, while for bundles bundle-breathing-like modes (BBLMs) arise, as predicted by Popov *et al.* [84] and Rahmani *et al.* [85], respectively. This could be shown by a correlation of Raman spectroscopy and HRTEM on the same individual MWCNT, while a small bundle was investigated with FT-Raman spectroscopy combined with an annealing study in air to remove the outer layers of those CNTs, which contribute to the inter-tube phonon coupling in bundles. A model based on a one-dimensional chain of equally coupled harmonic oscillators was presented to simulate the non-linear frequency shifts of the BLMs, induced by the inter-layer coupling, compared to the RBMs expected for SWCNTs. Thus, the simple $1/d_{\mathrm{T}}$-dependence of the observed radial Raman modes is no longer valid for MWCNTs. Further measurements of different individual MWCNTs and separated bundles may therefore allow the simulation of the BLMs and BBLMs for different diameters, providing a non-destructive tool for the determination of inter-molecular arrangements. Furthermore, we could show that the width of the obtained resonance profiles for BLMs of an individual MWCNT differs compared to the resonance profiles of individual and bundled SWCNTs. This provides additional information of the inter-layer structure and the inter-tube alignment of CNTs, which can usually only be obtained by HRTEM and offers a new way for the pre-characterization of individual CNTs grown on substrates for later transport measurements.
We could show that the synthesis of peapods from CVD-grown CNTs directly on substrates is possible. For the first time this was confirmed by a detailed study of each synthesis step using HRTEM and Raman spectroscopy. Two different oxidation techniques for opening CVD-grown CNTs, acid treatment and heating in air, were investigated in order to synthesize peapods on a substrate. During heating in air, inner layers are oxidized along with the outer layers, while during acid treatment, CNTs are

dissolved from the outside and the inside. Both oxidation methods lead to amorphous carbon inside the tubes, which is most prominent for the acid treated samples. Thus, we suggest that in the case of the acid treatment this amorphous material, which prevents later filling, consists of remnants from destroyed inner layers. Furthermore, acid treatment removes individual CNTs from the substrate. Therefore we focused on the oxidation of CNTs by heating in air, which leads to amorphous carbon that is sucked inside the tubes, plugging the opened entry ports. Another difficulty was the cleaning of the CNTs of C_{60} molecules sticking to the outer layers after evaporation of C_{60}. These problems could be solved by using a self-constructed UHV-chamber for the vapor filling, which permits the removal of the plugs before and cleaning of the samples after filling *in situ* by heating the substrate above the sublimation temperature. The remaining tubes and peapods are very clean on the outside and therefore suitable for the fabrication of electronic devices. They show different ordering phases of C_{60} molecules inside the CNTs, which directly depend on the inner diameter of the observed peapod. When endohedral fullerenes are used instead of empty C_{60}, this may allow the investigation of different spin couplings for different phases, which could help to study the transition from a one-dimensional spin system to a quasi-crystal providing different orientations and distances.
For bulk samples, the filling of CNTs with C_{60} molecules can also be confirmed by their characteristic Raman modes. This was shown for a cleaned peapod sample, where the $A_g(2)$-mode of C_{60} could be investigated, which showed a small down-shift in frequency, in agreement to other groups. Further experiments are needed to explain the origin of this slight shift, which may be due to tube-C_{60} or C_{60}-C_{60} interactions. However, since this shift could only be observed for C_{60} molecules located inside CNTs, it allows us to confirm the filling of a bulk sample. But, because of the weak intensity of the $A_g(2)$-mode, which is additionally decreased inside CNTs, filling of individual CNTs has to be proven by changes in the Raman modes of the CNT itself. Thus, further experiments on an individual CNT before and after filling are needed to study the influence of interior C_{60} molecules on the Raman modes of the encapsulating CNT.
This thesis confirmes the possibility to synthesize individual peapods directly on a substrate and to characterize them by either HRTEM as a last step or by Raman spectroscopy before further measurements, which permits to selectively choose adequate peapods for later transport measurements. Thus, this work lay the foundations for the fabrication of selected peapod based quantum devices in the future.

A first quantum transport device, which was fabricated with Au leads by K. Goß using electron beam lithography (EBL) on a Si substrate is shown in figure 8.1a. The black arrow points at the contacted unfilled CNT, which is coated by the source (S) and drain (D) contact on the left and on the right side, respectively. The gate contact is located in proximity of the CNT to tune the potential of the resulting quantum dot. A stability diagram of a similar device, featuring a quantum dot length of about 740 nm

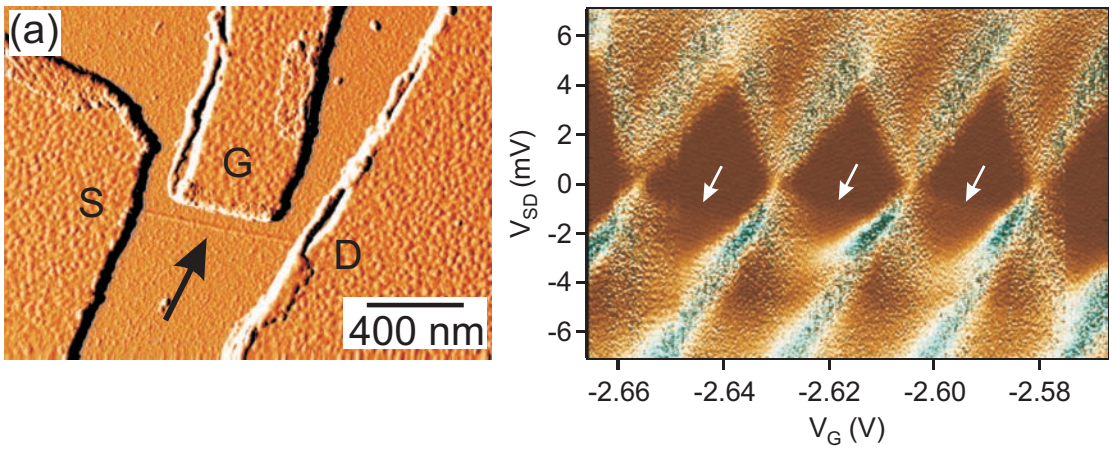

Figure 8.1: (a) AFM image of a contacted individual CNT (black arrow). The gate electrode (G) between the source (S) and drain (D) contacts provides the tuning of the potential of the quantum dot. (b) Stability diagram for a similar device measured at 40 mK for different gate voltages V_g showing the expected Coulomb diamonds. White arrows point at features in the Coulomb blockade regime.

was measured by K. Goß at 40 mK, as shown in figure 8.1b. It shows characteristic diamonds for different gate voltages V_g, resulting from the Coulomb blockade. These diamonds show features in the Coulomb blockade regime marked by white arrows that lead to a asymmetry of the diamonds for negative and positive voltages V_{SD} between source and drain contact. We suggest that these features arise from the hybridization of electronic states due to the coupling of two quantum dots. AFM measurements revealed a tube diameter of about 1.5 nm, but does not allow one to distinguish between an individual SWCNT, a MWCNT or a bundle of SWCNTs. Thus, it can not be investigated if more than one SWCNT is contacted. Therefore it is planned to characterize the inter-molecular structure of this device by Raman spectroscopy, as shown in this thesis, investigating its radial modes and the width of their resonance profiles. This may help to understand the asymmetry of the observed Coulomb diamonds in figure 8.1b and to interpret further transport measurements of devices that are fabricated on substrates being not accessible with HRTEM.
Since HRTEM is up to now the only obtainable method to confirm the filling of individual CNTs, a new kind of substrate was designed, which may allow the correlation of HRTEM, Raman spectroscopy and transport measurements on the same individual CNT. A first example of such a substrate is shown in figure 8.2, which was fabricated from a Si_3N_4 membrane by K. Goß and C. Morgan using reactive ion beam etching (RIBE). The patterning of the membrane is done by etching negative markers instead

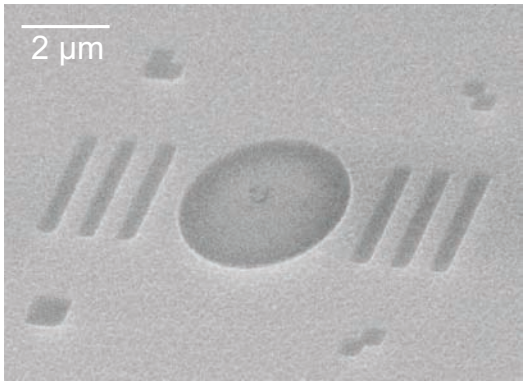

Figure 8.2: SEM image of a recently designed perforated membrane, which was fabricated by RIBE. Such a patterned TEM grid would enable one to contact CNTs for transport measurements in addition to HRTEM and Raman characterization.

of depositing positive markers, as used for Si substrates before. Beside the large hole with a diameter of about 3 µm which provides the investigation of individual CNTs crossing the hole after CVD growth, several small slits are etched into the membrane to confirm the complete filling of the CNT by using HRTEM. In further experiments, it is planned to contact these CNTs directly on the membrane, which was not possible for the perforated Si_3N_4 membranes used in this thesis, because of too little space between the holes for contacting individual CNTs. Thus, the structure and the filling of the measured tube can be determined, even though HRTEM can only be done after transport measurements. This may permit direct correlation of transport measurements from an individual contacted CNT to its atomic structure.

Bibliography

[1] S. Iijima, Nature (London) **354**, 56 (1991).

[2] L. V. Radushkevich, V. M. Lukyanovich, Zh. Fiz. Khim. **26**, 88 (1952).

[3] A. Oberlin, M. Endo, J. Cryst. Growth **32**, 335 (1976).

[4] J. Cumings, A. Zettl, Science **286**, 602 (2000).

[5] Q. S. Zheng, Q. Jiang, Phys. Rev. Lett. **88**, 45503 (2002).

[6] L. X. Zheng, M. J. O'Connell, S. K. Doorn, X. Z. Liao, Y. H. Zhao, E. A. Akhadov, M. A. Hoffbauer, B. J. Roop, Q. X. Jia, R. C. Dye, D. E. Peterson, S. M. Huang, J. Liu, Y. T. Zhu, Nature Materials **3**, 673 (2004).

[7] V. Krstić, S. Roth, M. Burghard, Phys. Rev. B **354**, R16334 (2000).

[8] S. Hong, S. Myung, Nature Nanotech. **2**, 207 (2007).

[9] Z. K. Tang, L. Zhang, N. Wang, X. X. Zhang, G. H. Wen, G. D. Li, J. N. Wang, C. T. Chan, P. Sheng, Science **292**, 2462 (2001).

[10] J. Nygard, D. H. Cobden, P. E. Lindelof, Nature **408**, 342 (2000).

[11] M. Bockrath, D. H. Cobden, J. Lu, A. G. Rinzler, R. E. Smalley, L. Balents, P. L. McEuen, Nature **397**, 598 (1999).

[12] Z. Yao, H. W. C. Postma, L. Balents, C. Dekker, Nature 402, **273** (1999).

[13] S. J. Tans, M. H. Devoret, H. Dai, A. Thess, R. E. Smalley, L. J. Geerligs, C. Dekker, Nature **386**, 474 (1997).

[14] H. W. Ch. Postma, T. Teepen, Z. Yao, M. Grifoni, C. Dekker, Science **293**, 76 (2001).

[15] L. Duclaux, Carbon **40**, 1751 (2001).

[16] S. Bandow, S. Asaka, Y. Saito, A. M. Rao, L. Grigorian, E. Richter, and P. C. Eklund, Phys. Rev. Lett. **80**(17), 3779 (2005).

[17] D. J. Hornbaker, S.-J. Kahng, S. Misra, B. W. Smith, A. T. Johnson, E. J. Mele, D. E. Luzzi, A. Yazdani, Science **295**, 828 (2002).

[18] J. Lee, H. Kim, S.-J. Kahng, G. Kim, Y.-W. Son, J. Ihm, H. Kato, Z. W. Wang, T. Okazaki, H. Shinohara, Y. Kuk, Nature **415**, 1005 (2002).

[19] T. Shimada, T. Okazaki, R. Taniguchi, T. Sugai, H. Shinohara, K. Suenaga, Y. Ohno, S. Mizuno, S. Kishimoto, T. Mizutani, Appl. Phys. Lett. **81**, 4067 (2002).

[20] H. Y. Yu, D. S. Lee, S. H. Lee, S. S. Kim, S. W. Lee, Y. W. Park, U. Dettlaff-Weglikowska, and S. Roth, Appl. Phys. Lett. **87**, 163118 (2005).

[21] P. Jaroenapibal, S. B. Chikkannanavar, D. E. Luzzi, J. Appl. Phys. **98**, 044301 (2005).

[22] H. Su, W. A. Goddard III., Y. Zhao, Nanotech. **17**, 5691 (2006).

[23] S. C. Benjamin, A. Ardavan, G. A. D. Briggs, D. A. Britz, D. Gunlycke, J. Jefferson, M. A. G. Jones, D. F. Leigh, B. W. Lovett, A. N. Khlobystov, S. A. Lyon, J. J. L. Morton, K. Porfyrakis, M. R. Sambrook, A. M. Tyryshkin, J. Phys.: Condens. Matter **18**, 867 (2006).

[24] A. Ardavan, M. Austwick, S. C. Benjamin, G. A. D. Briggs, T. J. S. Dennis, A. Ferguson, D. G. Hasko, M. Kanai, A. N. Khlobystov, B. W. Lovett, G. W. Morley, R. A. Oliver, D. G. Pettifor, K. Porfyrakis, J. H. Reina, J. H. Rice, J. D. Smith, R. A. Taylor, D. A. Williams, C. Adelmann, H. Mariette, R. J. Hamers, Phil. Trans. R. Soc. Lond. A **361**, 1473 (2003).

[25] J. Kong, H. T. Soh, A. M. Cassell, C. F. Quate, H. Dai, Nature **395** (1998).

[26] H. Kato, T. Okazaki, H. Shinohara, S. Iijima, S. Bandow, M. Takizawa, Chem. Phys. Lett. **347**, 23 (2001).

[27] A. G. Souza Filho, A. Jorio, Ge. G. Samsonidze, G. Dressselhaus, R. Saito, M. S. Dresselhaus, Nanotech. **14**, 1130 (2003).

[28] A. Jorio, R. Saito, J. H. Hafner, C. M. Liber, M. Hunter, T. McClure, G. Dresselhaus, M. S. Dresselhaus, Phys. Rev. Lett. **86**, 1118 (2001).

[29] B. W. Smith, M. Monthoux, D. E. Luzzi, Nature **396**, 323 (1998).

[30] S. B. Chikkannanavar, D. E. Luzzi, S. Paulson, and T. Johnson Jr., Nanolett. **5**, 151 (2005).

[31] Y. Ohno, Y. Kuokawa, S. Kishimoto, T. Mizutani, T. Shimada, M. Ishida, T. Okazaki, H. Shinohara, Y. Murakami, S. Maruyama *et al.*, Appl. Phys. Lett. **86** 023109 (2005).

[32] S. Okada, M. Otani, A. Oshiyama, Phys. Rev. B **67**, 205411 (2003).

[33] M. S. Dresselhaus, P. C. Eklund, Adv. Phys. **49**, 705 (2000).

[34] C.-H. Kiang, W. A. Goddard, III, R. Beyers, D. S. Bethune, J. Phys. Chem. **100**, 3749 (1996).

[35] B. Corzilius, Ph. D. Thesis, TU Darmstadt (2008).

[36] C. Thomsen and S. Reich, Top. Appl. Phys. **108**, 115 (2007).

[37] C. T. White, J. W. Mintmire, Nature (London) **394**, 29 (1998).

[38] E. D. Minot, Ph. D. Thesis, Cornell University (2004).

[39] P.R. Wallace, Phys. Rev. **71**, 622 (1947).

[40] S. Reich and C. Thomsen, Phys. Rev. B **62**, 4273 (2000).

[41] R. Saito, G. Dresselhaus, M. S. Dresselhaus,
"Physical Properties of Carbon Nanotubes", Imperial College Press, London (1998).

[42] S. Niyogi, M. A. Hamon, H. Hu, B. Zhao, P. Bhowmik, R. Sen, M. E. Itkis, R. C. Haddon, Acc. Chem. Res. **35**, 1105 (2002).

[43] S. Reich, C. Thomsen. P. Ordejón, Phys. Rev. B **65**, 155411 (2002).

[44] X. Blase, L. X. Benedict, E. L. Shirley, S. G. Louie, Phys. Rev. Lett. **72**, 1878 (1994).

[45] J. Kürti, V. Zólyomi, M. Kertesz, G. Sun, New J. Phys. **5**, 125 (2003).

[46] M. Ge, K. Sattler, Appl. Phys. Lett. **64**, 7 (1994).

[47] F. Wang, M. Y. Sfeir, L. Huang, X. M. H. Huang, Y. Wu, J. Kim, J. Hone, S. O'Brien, L. E. Brus, T. F. Heinz, Phys. Rev. Lett. **96**, 167401 (2006).

[48] C.-H. Kiang, M. Endo, P. M. Ajayan, G. Dresselhaus, M. S. Dresselhaus, Phys. Rev. Lett. **81**, 1869 (1998).

[49] Y. A. Kim, H. Muramatsu, T. Hayashi, M. Endo, M. Torrones, M. S. Dresselhaus, Chem. Phys. Lett. **398**, 87 (2004).

[50] Y. Li, S. Xie, W. Zhou, D. Tang, Z. Liu, X. Zou, G. Wang, Carbon **39**, 1429 (2001).

[51] W. Song, M. Ni, J. Lu, Z. Gao, S. Nagase, D. Yu, H. Ye, X. Zhang, Chem. Phys. Lett. **414**, 429 (2005).

[52] M. Hodak, L. A. Girifalco, Phys. Rev. B **67**, 075419 (2003).

[53] S. Okada, Chem. Phys. Lett. **438**, 59 (2007).

[54] A. Khlobystov, D. A. Britz, A. Ardavan, and G. A. Briggs, Phys. Rev. Lett. **67**, 24 (2004).

[55] H. Kataura, Y. Maniwa, M. Abe, A. Fujiwara, T. Kodama, K. Kikuchi, H. Imahori, Y. Misaki, S. Suzuki, Y. Achiba, Appl. Phys. A **74**, 349 (2002).

[56] A. Rochefort, Phys. Rev. B **67**, 115401 (2003).

[57] G. Binning, C. F. Quate, Ch. Gerber, Phys. Rev. Lett. **56**, 930 (1986).

[58] "Abteilungsbericht 1998 der Abteilung Festkörperphysik der Universität Ulm",
URL: `http://www.uni-ulm.de/fkp/berichte/iia/iia.htm`, Univesität Ulm (27.11.2009).

[59] "Atomic force microscopy",
URL: `http://en.wikipedia.org/wiki/Atomic_force_microscope`, Wikipedia (27.11.2009).

[60] M. Knoll, E. Ruska, Z. Physik **78**, 318 (1932).

[61] E. Ruska, Z. Physik **87**, 580 (1934).

[62] M. v. Ardenne, Z. Physik **19**, 407 (1938).

[63] K. W. Urban, Science **321**, 506 (2008).

[64] L. Houben, unpublished.

[65] M. Haider, H. Rose, S. Uhlemann, E. Schwan, B. Kabius, K. Urban, Nature **392**, 768 (1998).

[66] M. Lentzen, Ultramicroscopy **99**, 211 (2004).

[67] M. Lentzen, Microscopy and Microanalysis **12**, 191 (2006).

[68] C. L. Jia, M. Lenzen, K. Urban, Science **299**, 870 (2003).

[69] B. W. Smith, D. E. Luzzi, J. Appl. Phys. **90**, 3509 (2001).

[70] E. Hernández, V. Meunier. B. W. Smith, R. Rurali, H. Terrones, M. Buongiorno Nadelli, M. Terrones, D. E. Luzzi, and J.-C. Charlier, Nanolett. **3**, 1037 (2003).

[71] S. Bandow, M. Takizawa, H. Kato, T. Okazaki, H. Shinohara, S. Iijima, Chem. Phys. Lett. **347**, 23 (2001).

[72] C. V. Raman, K. S. Krishnan, Nature **121**, 501 (1928).

[73] S. Roehrig, Ph. D. Thesis, RWTH Aachen (2009).

[74] M. Minsky, Scanning **10**, 128 (1988).

[75] C. Fantini, A. Jorio, M. Souza, M. S. Strano, M. S. Dresselhaus, M. A. Pimenta, Phys. Rev. Lett. **93**, 147406 (2004).

[76] A. Weber, D. E. Jennings, J. W. Brault, Proceedings IXth International Conference on Raman Spectroscopy, Tokyo, 58 (1984).

[77] M. S. Dresselhaus, G. Dresselhaus, R. Saito, A. Jorio, Phys. Rep. **409**, 47 (2005).

[78] A. M. Keszler, L. Nemes, S. R. Ahmad, X. Fang, JOAM **6**, 1269 (2004).

[79] J. Maultzsch, H. Telg, S. Reich, C. Thomsen, Phys. Rev. B **72**, 205438 (2005).

[80] H. Telg, Diploma Thesis, TU Berlin (2004).

[81] A. Jorio, A. G. Souza Filho, G. Dresselhaus, M. S. Dresselhaus, R. Saito, J. H. Hafner, C. M. Lieber, F. M. Matinaga, M. S. S. Dantas, M. A. Pimenta, Phys. Rev. B **63**, 245416 (2001).

[82] A. Jorio, C. Fantini, M. S. S. Dantas, M. A. Pimenta, A. G. Souza Filho, Ge. G. Samsonidize, V. W. Brar, G. Dresselhaus, M. S. Dresselhaus, A. K. Swan, M. S. Ünlü, B. B. Goldberg, R. Saito, Phys. Rev. B **66**, 115411 (2002).

[83] H. Kataura, Y. Kumazawa, Y. Maniwa, I. Umezu, S. Suzuki, Y. Ohtsuka, Y. Achiba, Synth. Met. **103**, 2555 (1999).

[84] V. N. Popov, L. Henrard, Phys. Rev. B **65**, 235415 (2002).

[85] A. Rahmani, J.-L. Sauvajol, J. Cambedouzou, and C. Benoit, Phys. Rev. B **71**, 125402 (2005).

[86] R. P. Vidano, D. B. Fischbach, L. J. Willis, T. M. Loehr, Sol. Stat. Commun. **39**, 341 (1981).

[87] S. D. M. Brown, A. Jorio, P. Corio, M. S. Dresselhaus, G. Dresselhaus, R. Saito, K. Kneipp, Phys. Rev. B **63**, 155414 (2001).

[88] C. Thomsen, S. Reich, Phys. Rev. Lett. **85**, 5214 (2000).

[89] J. Kastner, T. Pichler, H. Kuzmany, S. Curran, W. Blau, D. N. Weldon, M. Delamesiere, S. Draper, H. Zandbergen, Chem. Phys. Lett. **221**, 53 (1994).

[90] D. S. Knight, W. B. White, J. Mater. Res. **4**, 385 (1988).

[91] A. C. Ferrari, J. C. Meyer, V. Scardaci, C. Casiraghi, M. Lazzeri, F. Mauri, S. Piscanec, D. Jiang, K. S. Novoselov, S. Roth, A. K. Geim, Phys. Rev. Lett. **97**, 187401 (2006).

[92] P. Corio, P. S. Santos, V. W. Brar, Ge. G. Samsonidze, S. G. Chou, M. S. Dresselhaus, Chem. Phys. Lett. **370**, 675 (2003).

[93] C. A. Cooper, R. J. Young, M. Halsall, Composites: Part A **32**, 401 (2001).

[94] W. Kräschmer, L. D. Lamb, D. R. Huffman, Nature **347**, 354 (1990).

[95] S. Iijima, T. Ichihashi, Nature **363**, 603 (1993).

[96] D. S. Bethune, C. H. Kiang, M. S. de Vries, G. Gorman, R. Savoy, J. Vazquez, R. Beyers, Nature **363**, 605 (1993).

[97] H. W. Kroto, J. R. Heath, S. C. O' Brien, R. F. Curl, R. E. Smalley, Nature **318**, 162 (1985).

[98] H. Kataura, Y. Kumazawa, Y. Maniwa, Y. Ohtsuka, R. Sen, S. Suzuki, Y. Achiba, Carbon **38**, 1691 (2000).

[99] W. Z. Li, J. G. Wen, Z. F. Ren, Appl. Phys. A **74**, 397 (2002).

[100] P. Utko, J. Nygård, M. Monthioux, L. Noé, Appl. Phys. Lett. **89**, 233118 (2006).

[101] C. H. L. Quay, J. Cumings, S. J. Gamble, A. Yazdani, H. Kataura, D. Goldhaber-Gordon, Phys. Rev. B **76**, 073404 (2007).

[102] M. J. Biercuk, S. Garaj, N. Mason, J. M. Chow, C. M. Marcus, Nanoletters **5**, 1267 (2005).

[103] C. Meyer, J. M. Elzermann, L. P. Kouwenhoven, Nanoletters **7**, 295 (2007).

[104] B. Zheng, Y. Li, J. Liu, Appl. Phys. A **74**, 345 (2002).

[105] N. Muradov, F. Smith, C. Huang, A. T-Raissi, Catalysis Today **116**, 281 (2006).

[106] N. Shah, D. Panjala, G. P. Huffman, Energy & Fuels **15**, 1528 (2001).

[107] J. Gavillet, A. Loiseau, C. Journet, F. Willaime, F. Ducastelle, J.-C. Chalier, Phys. Rev. Lett. **87**, 275504 (2001).

[108] H. Dai, A. G. Rinzler, P. Nikolaev, A. Thess, D. T. Colbert, R. E. Smalley, Chem. Phys. Lett. **260**, 471 (1996).

[109] S. Curtarolo, N. Awasthi, W. Setyawam, A. Jiang, K. Bolton, T. Tokune, A. R. Harutyunyan, Phys. Rev. B **78**, 054105 (2008).

[110] N. Nagaraju, A. Fonseca, Z. Konya, J. B. Nagy, J. Mol. Catal. A **181**, 57 (2002).

[111] G.-Y. Xiong, D. Z. Wang, Z. F. Ren, Carbon **44**, 969 (2006).

[112] M. H. Rümmeli, C. Kramberger, F. Schäffel, E. Borowiak-Palen, T. Gemming, B. Rellinghaus, O. Jost, M. Löffler, P. Ayala, T. Pichler, R. J. Kalenczuk, Phys. Stat. Sol. (b) **244**, 3911 (2007).

[113] A. Müller, S. Sarkar, S. Q. N. Shah, H. Bögge, M. Schmidtmann, S. Sarkar, P. Kögerler, B. Hauptfleisch, A. X. Trautwein, V. Schünemann, Angew. Chem. Int. Ed. **38**, 3238 (1999).

[114] L. An, J. M. Owens, L. E. McNeil, J. Liu, J. Am. Chem. Soc. **124**, 13688 (2002).

[115] K. Goss, A. Kamra, C. Spudat, C. Meyer, P. Kögerler, C. M. Schneider, Phys. Stat. Sol. (b) **246**, 2494 (2009).

[116] K. Edgar, J. L. Spencer, Curr. Appl. Phys. **6**, 419 (2006).

[117] J.-M. Bonard, M. Croci, C. Klinke, F. Conus, I. Arfaoui, T. Stöckli, A. Chatelain, Phys. Rev. B **67**, 085412 (2003).

[118] B. C. Liu, S. C. Lyu, T. J. Lee, S. K. Choi, S. J. Eum, C. W. Yang, C. Y. Park, C. J. Lee, Chem. Phys. Lett. **373**, 475 (2003).

[119] C. Spudat, C. Meyer, C. M. Schneider, Phys. stat. sol. (b) **245**, 2205 (2008).

[120] G. Y. Xiong, Y. Suda, D. Z. Wang, J. Y. Huang, Z. F. Ren, Nanotechnology **16**, 532 (2005).

[121] P. Nikolaev, A. Thess, A. G. Rinzler, D. T. Colbert, R. E. Smalley, Chem. Phys. Lett. **226**, 422 (1997).

[122] K. Méténier, S. Bonnamy, F. Béguin, C. Journet, P. Bernier, M. Lamy de La Chapelle, O. Chauvet, S. Lefrant, Carbon **40**, 1765 (2002).

[123] A. Jorio, A. G. Souza Filho, G. Dresselhaus, M. S. Dresselhaus, A. K. Swan, M. S. Ünlü, B. B. Goldberg, M. A. Pimenta, J. H. Hafner, C. M. Lieber, R. Saito, Phys. Rev. B **65**, 155412 (2002).

[124] K. Mølhave, S. B. Gudnason, A. T. Pedersen, C. H. Clausen, A. Horsewell, P. Bøggild, Ultramicroscopy **108**, 52 (2007).

[125] S. Maruyama, Tokyo University, URL:`http://www.photon.t.u-tokyo.ac.jp/~maruyama/kataura/kataura.html`, (04.12.2008).

[126] P. A. Denis, F. Iribarne, R. Faccio, J. Chem. Phys. **130**, 194704 (2009).

[127] J. M. Benoit, J. P. Buisson, O. Chauvet, C. Godon, S. Lefrant, Phys. Rev. B **66**, 073417 (2002).

[128] X. Zhao, Y. Ando, L.-C. Qin, H. Kataura, Y. Maniwa, R. Saito, Chem. Phys. Lett. **361**, 169 (2002).

[129] M. Mohr, J. Maultzsch, E. Dobardžić, S. Reich, I. Milošević, A. Bosak, M. Krisch, C. Thomsen, Phys. Rev. B **76**, 035439 (2007).

[130] X. Q. He, S. Kitipornchai, K. M. Liew, Nanotechnology **16**, 2086 (2005).

[131] S. K. Saha, U. V. Waghmare, H. R. Krishnamurthy, A. K. Sood, Phys. Rev. B **78**, 165421 (2008).

[132] M. Monthioux, Carbon **40**, 1809 (2002).

[133] P.M. Ajayan, T. W. Ebbesen, T. Ichihashi, S. Jijima, K. Tanigaki, H. Hiura, Nature **362**, 522 (1993).

[134] S. C. Tsang, Y. K. Chen, P. J. F. Harris, M. L. H. Green, Nature **372**, 159 (1994).

[135] T. M. Martínez, A. M. Callejas, A. M. Benito, M. Chet, T. Seeger, A. Ansón, J. Schreiber, C. Gordon, C. Marhic, O. Chauvet, W. K. Maser, Nanotech. **14**, 691 (2003).

[136] B. W. Smith, D. E. Luzzi, Chem. Phys. Lett. **321**, 169 (2000).

[137] J. Liu, A. G. Rinzler, H. Dai, J. H. Hafner, R. K. Bradley, P. J. Boul, A. Lu, T. Iverson, K. Shelimov, C. B. Huffman, F. Rodriguez-Macias, Y.-S. Shon, T. Randall Lee, D. T. Colbert, R. E. Smalley, Science **22**, 1253 (1998).

[138] M. Monthioux, B. W. Smith, B. Burteaux, A. Claye, J. E. Fischer, D. E. Luzzi, Carbon **39**, 1251 (2001).

[139] A. C. Dillon, T. Gennett, K. M. Jones, J. L. Alleman, P. A. Parilla, M. J. Heben, Adv. Mater. **11**, 1354 (1999).

[140] A. Kuznetsova, D. B. Mawhinney, V. Naumenko, J. T. Yates Jr., J. Liu, R. E. Smalley, Chem. Phys. Lett. **321**, 292 (2000).

[141] D. Ugarte, Nature **359**, 707 (1992).

[142] S. Osswald, E. Flahaut, Y. Gogotsi, Chem. Mater. **18**, 1525 (2006).

[143] H. Murphy, P. Papakonstantinou, T. I. T. Okpalugo, J. Vac. Sci. Technol. B **24**, 715 (2006).

[144] K. L. Lu, R. M. Lago, Y. K. Chen, M. L. H. Green, P, J, Harris, S. C. Tsang, Carbon **34**, 814 (1996).

[145] W. Plank, H. Kuzmany, F. Simon, T. Saito, S. Ohshima, M. Yumura, S. Iijima, G. Rotas, G. Pagona, N. Tagmatarchis, Phys. Stat. Sol. (b) **244**, 4074 (2007).

[146] F. Simon, H. Kuzmany, H. Rauf, T. Pichler, J. Bernardi, H. Peterlik, L. Korecz, F. Fülöp, A. Jánossy, Chem. Phys. Lett. **383**, 362 (2004).

[147] H. Kataura, Y. Maniwa, T. Kodama, K. Kikuchi, K. Hirahara, K. Suenaga, S. Iijima, S. Suzuki, Y. Achiba, W. Krätschmer, Synth. Met. **121**, 1195 (2001).

[148] C. K. Mathews, M. Sai Baba, T. S. Lakshmi Narasimhan, R. Balasubramanian, N. Sivaraman, T. G. Srinivasan, P. R. Vasudeva Rao, J. Phys. Chem., **96**, 3566 (1992).

[149] S. Berber,Y.-K. Kwon, D. Tománek, Phys. Rev. Lett. **88**, 185502 (2002).

[150] S. Okada, S. Saito, A. Oshiyama, Phys. Rev. Lett. **86**, 3835 (2001).

[151] R. S. Ruoff, D. S. Tse, R. Malhotra, D. C. Lorents, J. Phys. Chem. **97**, 3379 (1993).

[152] D. Ugarte, T. Stöckli, J. M. Bonard, A. Châtelein, W. A. de Heer, Appl. Phys. A **67**, 101 (1998).

[153] S. Bandow, K. Hirahara, T. Hiraoka, G. Chen, P. C. Eklund, S. Iijima, MRS Bulletin, **29**, 260 (2004).

[154] A. M. Rao, P. Zhou, K.-A. Wang, G. T. Hager, J. M. Holden, Y. Wang, W.-T. Lee, X.-X. Bi, P. C. Eklund, D. S. Cornett, M. A. Duncan, I. J. Amster, Science **259**, 955 (1993).

[155] K. Venkatesan, V. Ramamurthy, *"Biomolecular photoreactions in crystals"*, VCH, Weinheim (1991).

[156] Y. Wang, J.M. Holden, Z.-H. Dong, X.-X. Bi, P.C. Eklund, Chem. Phys. Lett. **211**, 341 (1993).

[157] T. Pichler, A. Kukovecz, H. Kuzmany, H. Kataura, Y. Achiba, Phys. Rev. B **67**, 125416 (2003).

[158] Y. Zou, B. Liu, M. Yao, Y. Hou, L. Wang, S. Yu, P. Wang, B. Li, B. Zou *et al.*, Phys. Rev. B **76**, 195417 (2007).

[159] K. Hirahara, K. Suenaga, S. Bandow, H. Kato, T. Okazaki, H. Shinohara, S. Iijima, Phys. Rev. Lett. **85** 5384 (2000).

[160] H. Qiu, Z. Shi, S.-L. Zhang, Z. Gu, J. Qiu, Sol. Stat. Commun. **137**, 654 (2006).

[161] K. Jensen, J. Weldon, H. Garcia, and A. Zettl, Nanoletters **7**, 3508 (2007).

[162] P. G. Collins, K. Bradley, M. Ishigami, A. Zettl, Science **287**, 1801 (2000).

[163] P. Qi, O. Vermesh, M. Grecu, A. Javey, Q. Wang, and H. Dai, Nanoletters **3**, 347 (2003).

[164] J. Kastner, T. Pichler, H. Kuzmany, S. Curran, W. Blau, D. N. Weldon, M. Delamesiere, S. Draper, H. Zandbergen, Phys. Rev Lett. **30**, 929 (1999).

[165] M. Yudasaka, K. Ajima, K. Suenaga, T. Ichihashi, A. Hashimoto, S. Iijima, Chem. Phys. Lett. **380**, 42 (2003).

[166] S. Henke, K. H. Thürer, J. K. N. Lindner, B. Rauschenbach, B. Stritzker, J. Appl. Phys. 76, 3337 (1994).

[167] S. Bandow, T. Hiraoka, T. Yumura, K. Hirahara, H. Shinohara, S. Iijima, Chem. Phys. Lett. **384**, 320 (2004).

[168] D. Ugarte, Carbon **33**, 989 (1995).